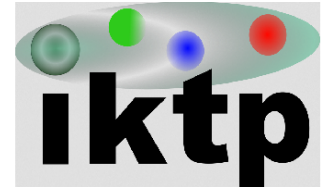# Search for a light CP-odd Higgs boson decaying into a $\tau\tau$ pair

Master-Arbeit
zur Erlangung des Hochschulgrades
Master of Science
im Master-Studiengang Physik

vorgelegt von

Paul Moder

geboren am 24.05.1993 in Dresden

Institut für Kern- und Teilchenphysik
Fachrichtung Physik
Fakultät Mathematik und Naturwissenschaften
Technische Universität Dresden

Eingereicht am 05. Oktober 2018

Abstract

The two-Higgs-doublet model (2HDM) is an extension of the Standard Model of particle physics (SM) that is able to explain many of its problems. One of these is the deviation between the predicted and measured value for the anomalous magnetic moment of the muon. The 2HDM predicts an additional Higgs field that introduces four new Higgs bosons. One of these is the neutral CP-odd Higgs boson A which is predicted to be light in the flavour-aligned model. The discovery of a light CP-odd Higgs boson would therefore hint at the existence of physics beyond the SM.

In this thesis different analyses are presented for the search of a light CP-odd Higgs boson with a mass of 60 GeV, 70 GeV, 80 GeV and 90 GeV. The decay channel of all analyses is the $A \rightarrow \tau\tau$ channel with both τ leptons decaying leptonically. The analyses are done for combined data from 2015 and 2016 with an integrated luminosity of $36.1\,\mathrm{fb}^{-1}$ recorded by the ATLAS detector. The thesis will show that the presented analyses have a high enough sensitivity for a possible discovery and it presents the expected upper limits on the up-type quark coupling for each mass prediction.

Zusammenfassung

Das Zwei-Higgs-Doublet-Modell (2HDM) ist eine Erweiterung des Standardmodells der Teilchenphysik (SM), welches Erklärungen für verschiedene seiner Probleme präsentiert. Eines dieser Probleme ist die Abweichung zwischen Messung und Vorhersage für den Wert des anormalen magnetischen Moments des Myons. Das 2HDM führt ein zusätzliches Higgsfeld ein, welches zu vier weiteren Higgsbosonen führt, von denen eines neutral und CP-ungerade ist. In der speziellen Theorie des "flavour-aligned" 2HDM ist dieses Boson darüber hinaus auch leicht. Die Entdeckung eines solchen Bosons würde somit Hinweise für Physik jenseits des Standardmodells liefern.

In dieser Arbeit werden Analysen für die Suche nach einem leichten CP-ungeraden Higgsboson mit Massen von 60 GeV, 70 GeV, 80 GeV und 90 GeV präsentiert. Der Zerfallskanal der Analyse ist der $A \rightarrow \tau\tau$ Kanal, wobei die τ Leptonen nur leptonisch zerfallen können. Die Analysen verwenden die kombinierte Datenmenge, welche vom ATLAS-Detektor in den Jahren 2015 und 2016 gemessen wurde, was einer Luminosität von $36.1\,\mathrm{fb}^{-1}$ entspricht. Die Arbeit zeigt, dass die vorgestellten Analysen eine hoch genügende Sensitivität für eine mögliche Entdeckung eines CP-ungeraden Higgs Bosons haben und es werden die erwarteten oberen Grenzen der Kopplungen der Up-Typ-Quarks für alle Massen präsentiert.

Contents

List of Figures

List of Tables

1 Introduction

With the discovery of the electron by J.J. Thomson in 1897 [1] the idea of a theory describing the particles at their smallest scale had begun. But for this, a lot of the known theories had to be reworked. The first theories that changed the fundamentals were the theory of relativity by Einstein in 1916 [2] and the theory of quantum electrodynamics (QED) by Schwinger, Feynman and others in the late 40s [3,4]. Based on this work Glashow, Weinberg and Salam unified the weak interaction with the QED to the theory of the electroweak interaction in the late 60s [5–7]. This theory describes the electroweak interaction as an exchange of $W^{\pm}$ and Z^0 gauge bosons, which were later discovered by the UA1 and UA2 experiments [8,9]. But there was still one problem that the theory was not able to explain. The fermions and bosons were predicted to be massless, but the experiments showed the opposite. The solution to this problem was discovered by Higgs, Engelbert and Brout independently at the same time. By postulating a scalar field, which is called the Higgs field, the masses of the particles could be explained [10–12]. Furthermore, an additional boson was predicted, the Higgs boson, which was discovered at the Large Hadron Collider (LHC) by the ATLAS and CMS detectors in 2012 [13,14]. The theory of the quantum chromodynamics (QCD) was developed at the same time as the Higgs mechanism. It could explain the interaction between quarks, why they are bound within hadrons and why they can not be observed as free particles [15–18]. All of these models were then combined into one model that explains the fundamentals of nature. This model is called the Standard Model of particle physics (SM) [19].

Until this day the SM passed all tests of its predictions using different kinds of experiments. Every particle predicted by the SM was found, the latest one being the Higgs boson. Furthermore, most of the properties of all particles were measured very precisely and in most cases the SM predictions were found to be correct. However, the SM is not a perfect model. For instance the fourth fundamental force, the gravity, is not describes in the SM at all. In addition to that, not all observations of nature could be described by the SM, one of the most prominent ones being the existence and mass of dark matter [20]. Therefore, many theories were conceived that go beyond the SM and are able to explain many of its problems. One of these theories is the two-Higgs-doublet model (2HDM), which predicts the existence of an additional Higgs field and therefore also additional Higgs bosons. Finding these additional particles would give a hint at physics beyond the SM. However, these particle are only produced rarely in comparison to known SM particles.

To be able to produce these particles, the LHC was built along with different detectors. One of them is the ATLAS detector. The LHC is a particle accelerator and it collides proton-proton pairs at high energies to create different particles through their interaction. These protons do not only collide with a center-of-mass energy of $\sqrt{s} = 14\,\text{TeV}$, which enables the production of heavy particles, but the number of collisions is very high which allows the search for rare processes. But in order to find these rare processes against the background of all the known SM processes, collision events with certain properties have to be selected and analysed.

The goal of this thesis is to present an analysis, that can be used to search for a light CP-odd Higgs boson that is predicted by the flavour-aligned two-Higgs-doublet model. For this, the flavour-aligned 2HDM is presented in section 2.2. This section also describes the properties, production and decay of a light CP-odd Higgs boson. Chapter 4 describes the analysis for the search of this boson. The background and signal processes are analysed and the cuts to maximize the ratio between signal and background are presented. Chapter 5 shows the sensitivity of the analyses for four different masses of the CP-odd Higgs boson. Furthermore, a likelihood ratio test is done to determine the expected upper limits for the up-type quark couplings of the new Higgs field in dependence on the different masses of the Higgs bosons.

2 Theory

In this chapter a short summary of the theory behind a possible CP-odd Higgs Boson is given. Because it is an extension of the Standard Model the basics of the Standard Model are explained first, before going into its limitations. From these limitations the motivation for the two-Higgs-doublet Model (2HDM) is shown. The fundamentals of the model will be described as well as the introduction of the CP-odd Higgs boson. The section will then also present the properties of this new particle and how this will affect the analysis during this thesis. At the end, the basics for a statistical evaluation of an analysis are presented.

2.1 Standard Model of Particle Physics

2.1.1 Elementary Particles

The Standard Model of Particle Physics (SM) is a summary of all the currently known elementary particles and their interactions. With the electromagnetic, the weak and the strong interaction it describes three out of four known interactions very precisely. These interactions are represented through a gauge group $\mathrm{SU(3)_C \otimes SU(2)_L \otimes U(1)_Y}$ where $\mathrm{SU(3)_C}$ represents the group of the strong interaction with the colour C and $\mathrm{SU(2)_L \otimes U(1)_Y}$ represents the electroweak group with the left chirality L and the weak hypercharge Y. A certain interaction between particles is only possible if they carry the corresponding charge. For example, a neutral particle can not interact through the electromagnetic interaction. The same goes for the weak interaction, where the charge is the weak hypercharge. In the strong interaction the charge is the colour.

The elementary particles of the SM shown in figure 2.1 are divided into two groups. The first group of particles consists of fermions, which have a half-integer spin. The fermions are then further classified as quarks or leptons with three generations for both classes. Fermions of one generation do not differ in their coupling structure, but in their mass or charge only. For leptons, these three generations are electrons (e), muons (μ) and taus (τ) together with their corresponding neutrinos (ν). Leptons do not interact through the strong interaction, but always through the weak interaction. In addition to that, only electrons, muons and taus can interact via electromagnetic interaction, because they all have an electromagnetic charge of ± 1, while neutrinos are always neutral. Furthermore, it was assumed at first that neutrinos have no mass. This was later disproven through the observation of neutrinos changing their flavour. This is only possible, if neutrinos have different masses. Still, experiments show that neutrinos can only have a very small mass. And because they only interact through the weak interaction, the cross-sections of their interactions are small. This is the reason, why they can not be detected directly. [19]

In comparison to the leptons, there are also 6 quarks in the SM: up (u), down (d), charm (c), strange (s), top (t) and bottom (b). Like leptons, they also interact through the weak interaction.

In addition to that, they also interact through the electromagnetic interaction, because they have an electromagnetic charge of 2/3 (up-type quarks) or -1/3 (down-type quarks). Furthermore, they also carry a colour charge (red, green, blue), which means that they interact through the strong interaction as well. But other than the electromagnetic charge, the colour charge can not be measured, because no free particle was ever observed carrying a color. This leads to two conclusions about quarks. First, a quark can not be a free particle. Free particles always have to be composed of two (mesons) or three quarks (baryons). The second conclusion is that the colours of quarks making up a free particle, have to add up to a colour neutral state. A colour neutral state is achieved, when a colour and an anti-colour are combined (i. e. red and anti-red) or when all colours are combined (red, green and blue). [19]

Additional to every fermion there also exists an anti-fermion. These anti-particles are nearly identical to the original particles. The only difference is that they have the opposite charge. For example the positron is the anti-particle of the electron, which means it has the same mass and interaction cross-section. But instead of having an electromagnetic charge of -1, it has a charge of +1. The difference in the charge is also not limited to the electromagnetic charge alone. The anti-particle of a bottom quark with the colour-charge red is an anti-bottom quark with an electromagnetic charge of +1/3 and the colour anti-red [19]. While the anti-particle for most particles was found, the anti-particles for neutrinos are still just a theory. As it only interacts through the weak interaction, the anti-particle of the neutrino could only be found through a difference in the weak hypercharge. However, the weak hypercharge can only be calculated theoretically through the electromagnetic charge (see section 2.1.2). Therefore, it is also possible that there is no anti-particle for the neutrino. The neutrino itself would then be its own anti-particle, which is called a Majorana particle [22]. Due to the similar properties, anti-particles will always be implied when talking about fermions in this thesis, except something different is stated explicitly.

The other group of particles besides fermions are the gauge bosons, which have an integer spin. They can be interpreted as carriers of the interactions. They act as mediators between the particles that carry the charge of the corresponding interaction. For example, photons interact only with particles that have an electromagnetic charge, so they do not interact with neutrinos. The other gauge bosons are the gluons for the strong interaction and W^+, W^- and Z^0 bosons for the weak interaction. The
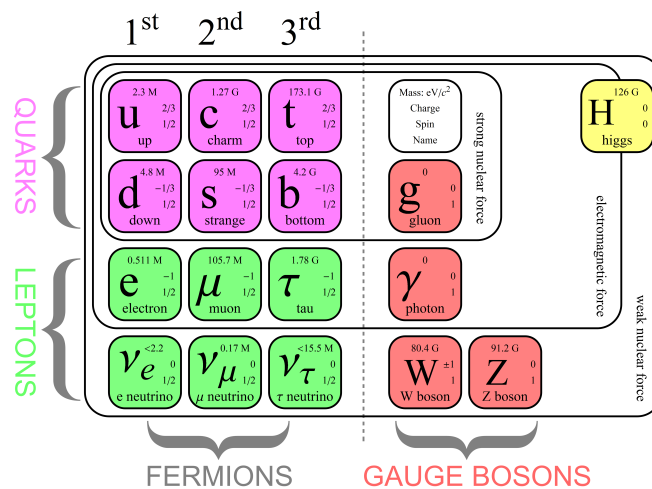
Figure 2.1: Elementary Particles of the SM [21]

W and Z bosons are also the only bosons that have a mass. Because of their mass, the gauge bosons for the weak interaction have a very short lifetime of around $3 \cdot 10^{-25}$s, which means that the weak interaction can only occur over a short distance. And even though gluons do not have a mass, the range of the strong interaction is also small, because the energy between two strongly interacting particles increases with the distance. So if the distance between two quarks is reaching a certain point, the resulting energy of the field leads to the creation of a new quark-antiquark pair reducing the interaction distance again. This is the second reason why free quarks can not exist. If two quarks are separated far enough, another quark-antiquark pair will be produced. In contrast to that, the electromagnetic interaction can occur over infinite distances. Aside from the interaction with elementary particles bosons are able to interact with each other, if they carry the corresponding charge. As gauge bosons of the weak interaction carry its charge, there are also some possible interactions between them. An example is presented in figure 2.2. The same applies to the strong interaction. It contains eight different gluon fields, each representing a different color-anticolor state, what leads to an interaction between gluons. At last the W$^+$ and W$^-$ bosons can also interact with the photon as they are carrying an electromagnetic charge in addition to their weak charge. [19]

The last particle of the SM is the Higgs boson. This particle was predicted early in the theory of the Higgs mechanism and it was detected in 2012 [13, 14]. The Higgs boson is different from the other bosons as it has a spin of 0 and it is not a carrier of an interaction. It is however very important as the existence of the Higgs boson is the reason that all the other particles in the SM have a mass. This will be further explained in section 2.1.3.

2.1.2 Electroweak Unification

The Lagrangian of the SM can be written as

$$\mathcal{L}_{SM} = \mathcal{L}_{gauge} + \mathcal{L}_f + \mathcal{L}_{Higgs} + \mathcal{L}_{Yukawa} \tag{2.1}$$

where $\mathcal{L}_{Higgs}$ is the term of the Higgs field and $\mathcal{L}_{Yukawa}$ is the term for the Yukawa coupling of the fermions. Both become important later in section 2.1.3. In this section the fermion term is analysed

$$\mathcal{L}_f = \bar{l}i\gamma^\mu\partial_\mu l + \bar{e}_R i\gamma^\mu\partial_\mu e_R + \bar{Q}i\gamma^\mu\partial_\mu Q + \bar{u}_R i\gamma^\mu\partial_\mu u_R + \bar{d}_R i\gamma^\mu\partial_\mu d_R. \tag{2.2}$$

In the electroweak unification fermions are grouped into two types: left-handed fermions, which are doublets and right handed fermions being singlets. In equation (2.2) the left-handed doublets are
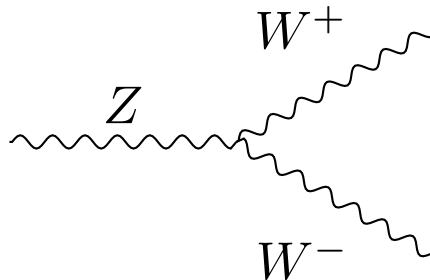
Figure 2.2: Allowed interaction between bosons of the weak interaction

symbolised by $l = (\nu_e, e)_L^T$ and $Q = (u, d)_L^T$ and the right-handed singlets are symbolised by e_R, u_R and d_R. Furthermore, it has to be summed over all possible generations of fermions. For example e_R does not only represent right-handed electrons, but also right-handed muons and right-handed taus. However, neutrinos are not included in this sum, as there are no right-handed neutrinos in the SM. The fermions carry a weak isospin T in this theory, which is 1/2 for doublets and 0 for singlets. In addition to that, all fermions carry a weak hypercharge Y, which is related to the third component of the weak isospin T_3 and the electromagnetic charge Q through the equation

$$Q = T_3 + Y \tag{2.3}$$

with T_3 being +1/2 for the first particle and -1/2 for the second particle in the fermion doublet. Then the gauge transformations for the fermion doublets and singlets are

$$l \rightarrow l' = e^{i\alpha(x)Y_L} \cdot e^{i\sum_a \Theta_a(x)T^a} l \tag{2.4}$$

$$e_R \rightarrow e'_R = e^{i\alpha(x)Y_R} e_R \tag{2.5}$$

where $\alpha(x)$ and $\Theta_a(x)$ are gauge functions, Y_L and Y_R are the values of the hypercharge for left handed doublets and right handed singlets and T^a are matrices defined by the Pauli matrices σ

$$T^a = \frac{\sigma^a}{2} \tag{2.6}$$

$$\sigma^1 = \begin{pmatrix} 0 & 1 \\ 1 & 0 \end{pmatrix} \quad \sigma^2 = \begin{pmatrix} 0 & -i \\ i & 0 \end{pmatrix} \quad \sigma^3 = \begin{pmatrix} 1 & 0 \\ 0 & -1 \end{pmatrix}. \tag{2.7}$$

With this transformation the following covariant derivative is needed for the Lagrangian to be invariant

$$D^\mu l = (\partial^\mu + ig_W T^a W_a^\mu + ig_Y Y_L B^\mu)l, \quad D^\mu e_R = (\partial^\mu + ig_Y Y_R B^\mu)e_R \tag{2.8}$$

where W^μ and B^μ are the gauge fields that come from the term $\mathcal{L}_{gauge}$ in the Lagrangian of the SM

$$\mathcal{L}_{gauge} = -\frac{1}{4} W_a^{\mu\nu} W_{\mu\nu}^a - \frac{1}{4} B^{\mu\nu} B_{\mu\nu}. \tag{2.9}$$

With that, the transformation of these gauge fields can be written as

$$W_a^\mu \rightarrow W_a^{\mu\prime} = W_a^\mu - \frac{1}{g_W} \partial^\mu \Theta_a(x) + \epsilon_{abc} \Theta^b(x) W^{c,\mu} \tag{2.10}$$

$$B^\mu \rightarrow B^{\mu\prime} = B^\mu - \frac{1}{g_Y} \partial^\mu \alpha(x). \tag{2.11}$$

This leads to a sum of four gauge fields. The first three gauge fields W_1^μ, W_2^μ, W_3^μ with the weak coupling g_W correspond to the three generators of the $SU(2)_L$ group. The fourth gauge field B^μ with the gauge coupling g_Y corresponds to the generator of the $U(1)_Y$ group. All gauge fields have mass

eigenstates which are defined as a mixture of W_a^μ and B^μ

$$W^{\pm,\mu} = \frac{1}{\sqrt{2}} \left(W_1^\mu \mp i W_2^\mu \right) \tag{2.12}$$

$$\begin{pmatrix} A^\mu \\ Z^\mu \end{pmatrix} = \begin{pmatrix} \cos(\Theta_W) & \sin(\Theta_W) \\ -\sin(\Theta_W) & \cos(\Theta_W) \end{pmatrix} \begin{pmatrix} B^\mu \\ W_3^\mu \end{pmatrix} \tag{2.13}$$

where Θ_W is the mixing angle calculated through the following relations

$$\cos(\Theta_W) = \frac{g_W}{\sqrt{g_W^2 + g_Y^2}} \tag{2.14}$$

$$e = g_W \sin(\Theta_W) = g_Y \cos(\Theta_W). \tag{2.15}$$

$$\tag{2.16}$$

The mass eigenstates of the gauge fields can then be associated with bosons. The fields $W^{\pm,\mu}$ represent the $W^\pm$ bosons, the Z^μ field represents the Z^0 boson and the A^μ field represents the photon. [23]

2.1.3 Higgs Mechanism

While the SM described so far could explain all of the elementary particles and their interactions between each other, particles in this model were all massless as there was no mathematical explanation for the mass of the particles. This is why the Higgs mechanism was included into the SM. The basic idea of the Higgs Mechanism is the spontaneous symmetry breaking. First, a new scalar spin 0 field was postulated:

$$\Phi = \begin{pmatrix} \phi^+ \\ \phi^0 \end{pmatrix} \tag{2.17}$$

which leads to the term $\mathcal{L}_{Higgs}$ in the Lagrangian of the SM

$$\mathcal{L}_{Higgs} = (D^\mu \Phi)^\dagger (D_\mu \Phi) - V(\Phi) \tag{2.18}$$

with the potential $V(\Phi)$

$$V(\Phi) = -\mu^2 \Phi^\dagger \Phi + \lambda \left(\Phi^\dagger \Phi \right)^2 \tag{2.19}$$

where λ is real and positive. For μ^2 there are two different cases. If μ^2 is negative, then the potential has only one minimum, which is the ground state at $\Phi = 0$. This case is not observed as it just represents a standard QED theory with a massless photon and a charged scalar field ϕ with mass μ. But if μ^2 is positive, then the potential is degenerate with an infinite number of ground states, shown in figure 2.3. This solution leads to the spontaneous symmetry breaking. At the beginning, the system is in a state of symmetry at the point of origin, which is a local maximum. But because every system aims at minimizing its energy, it changes into a random ground state, so the symmetry is broken. One of these ground states can be chosen

$$\langle \Phi \rangle = \frac{1}{\sqrt{2}} \begin{pmatrix} 0 \\ v \end{pmatrix} \tag{2.20}$$
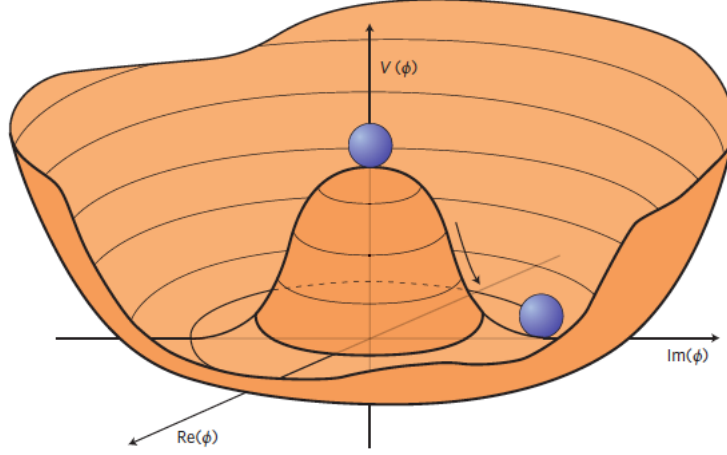
Figure 2.3: Higgs Potential [24]

with $\frac{v^2}{2} = \frac{\mu^2}{2\lambda}$. v is called the vacuum expectation value (VEV). This means, that the charge of Φ is 0 and the $SU(2)_L \otimes U(1)_Y$ group is broken into an electromagnetic $U(1)_Q$ group. The Higgs doublet can then be parametrised to

$$\Phi = \langle \Phi \rangle + \begin{pmatrix} G^+ \\ \frac{1}{\sqrt{2}} \left(H + iG^0 \right) \end{pmatrix} = \begin{pmatrix} G^+ \\ \frac{1}{\sqrt{2}} \left(v + H + iG^0 \right) \end{pmatrix} \tag{2.21}$$

and with a gauge transformation this leads to

$$\Phi = \begin{pmatrix} 0 \\ \frac{1}{\sqrt{2}} \left(v + H \right) \end{pmatrix} \tag{2.22}$$

what shows that the fields G^+ and G^0 are Goldstone bosons. This is not unexpected as the Goldstone theorem states that there will always be at least one new massless scalar particle if a symmetry gets broken. Furthermore, it can be seen that the field H is a massive Higgs boson with the mass $m_h = \sqrt{2}\mu = \sqrt{2\lambda}v$. With this the kinetic part of $\mathcal{L}_{Higgs}$ can be written as

$$(D^\mu \phi)^\dagger (D_\mu \phi) = \frac{v^2}{8} \left(1 + \frac{H}{v} \right)^2 \left[g_W^2 \left((W_\mu^1)^2 + (W_\mu^2)^2 \right) + (g_W W_\mu^3 - g_Y B_\mu)^2 \right] + (\partial^\mu \Phi)^\dagger (\partial_\mu \Phi) \tag{2.23}$$

$$\overset{(2.12)}{=} \left(1 + \frac{H}{v} \right)^2 \left[\left(\frac{v g_W}{2} \right)^2 W^{+,\mu} W_\mu^- + \frac{1}{2} \left(\frac{v}{2} \right)^2 (g_W^2 + g_Y^2) Z^\mu Z_\mu + 0 \cdot A^\mu A_\mu \right] \tag{2.24}$$
$$+ (\partial^\mu \Phi)^\dagger (\partial_\mu \Phi).$$

This directly provides all the boson masses

$$m_H = \sqrt{2\lambda}v \tag{2.25}$$

$$m_W = \frac{g_W v}{2} \tag{2.26}$$

$$m_Z = \frac{v}{2}\sqrt{g_W^2 + g_Y^2} \tag{2.27}$$

$$m_A = 0. \tag{2.28}$$

Therefore, the mechanism does not only explain, why the photon has no mass, but it directly explains, why the bosons from the weak interaction have a mass. [25]

This leaves the question, how the Higgs field gives mass to fermions. This coupling is described by the last term of the Lagrangian, the Yukawa coupling term, which for the first generation of fermions is given by

$$\mathcal{L}_{Yukawa} = f_e \bar{l} \Phi e_R + f_d \overline{Q} \Phi d_R + f_u \overline{Q} \Phi^c u_R + h.c. \tag{2.29}$$

with $\Phi^c = i\sigma^2 \Phi^*$ and f_i being the coupling constant for the fermion. It can be seen that the Higgs field only couples to fermions that have a left handed and a right handed component. As neutrinos do not have a right handed component, they do not couple to the Higgs field and so they can not have a mass. Other fermions have a mass as consequence of the interaction with the Higgs field and on tree level those can be found as [25]

$$m_e = \frac{f_e v}{\sqrt{2}} \tag{2.30}$$

$$m_d = \frac{f_d v}{\sqrt{2}} \tag{2.31}$$

$$m_u = \frac{f_u v}{\sqrt{2}}. \tag{2.32}$$

2.1.4 CP-symmetry and violation

The CP-symmetry, which is shortly called CP, is a combination of the parity and charge conjugation symmetries. This combined symmetry was postulated to be invariant in the SM after it was found that neither parity nor charge conjugation were invariant symmetries. The idea of the parity symmetry is that a physical system is invariant under the flip of the spatial coordinates. The parity operator is therefore defined as

$$P\Psi(x,y,z) = \Psi(-x,-y,-z). \tag{2.33}$$

When applying the operator a second time on the same state, the original state is restored

$$P^2\Psi(x,y,z) = P\Psi(-x,-y,-z) = \Psi(x,y,z) \tag{2.34}$$

and assuming that $\Psi(x,y,z)$ is an eigenstate of P

$$P^2\Psi(x,y,z) = \lambda_P P\Psi(x,y,z) = (\lambda_P)^2 \Psi(x,y,z) = \Psi(x,y,z) \tag{2.35}$$

it can be concluded that the eigenvalues of P are either +1 or -1. The eigenvalue λ_P for a particle is called the intrinsic parity. If this value is +1, the particle has an even parity and if the value is -1, the particle has an odd parity. By definition the intrinsic parity of fermions with a spin of $1/2$ is +1 and the intrinsic parity of their anti-particles is -1. Bosons can be classified according to their spin s and parity. This is shown in table 2.1.

However, this is only true as long as the orbital angular momentum l is 0. If it is not 0, then only the total angular momentum j is conserved with j being the vectorial sum of l and s

$$\vec{j} = \vec{l} + \vec{s}. \tag{2.36}$$

State	Spin	Parity
Scalar	0	+1
Pseudoscalar	0	-1
Vector	1	-1
Pseudovector	1	+1

Table 2.1: Classification of particles according to their spin and parity

In the case of $l \neq 0$ the classification in table 2.1 is then dependent on j. Furthermore, the orbital angular momentum l also influences the parity. Wave functions that contain spherical harmonics have a parity dependent on l

$$P\Psi(r,\Theta,\phi) = PR(r)Y_m^l(\Theta,\phi) = (-1)^l R(r)Y_m^l(\Theta,\phi) \tag{2.37}$$

which means that the parity of a particle is no longer equal to its intrinsic parity

$$\lambda_P^l = \lambda_P(-1)^l. \tag{2.38}$$

In addition to that, the parity is not only a property of a particle, but also of a particle system. For example the parity of a two-particle system is

$$\lambda_{P_1,P_2}^L = \lambda_{P_1}\lambda_{P_2}(-1)^L \tag{2.39}$$

with L being the relative angular momentum number of the two particles P_1 and P_2. This means that if parity during a process is conserved, the parity of a mother particle can be calculated from the parities of the daughter particles and their relative angular momentum. [26]

While parity was thought to be invariant in a physical system, it was found that the SM violates the parity symmetry through the weak interaction. This was first shown in an experiment by Chien-Shiung Wu. In this experiment a cobalt-60 nucleus was polarised and decayed into an electron and neutrino afterwards. The angle θ between the orientation of the nucleus and the momentum of the electron was measured and it could be shown that there was a significant difference in the θ and $180° - \theta$ distribution. Therefore, the electron had a preferred direction in relation to the spin of the nucleus, which means that this process is not P-conservative. [27]

In addition to the parity, the CP-symmetry also contains a symmetry under the operation of charge conjugation. When applying the charge conjugation operator on a system, every particle is turned into its anti-particle

$$C\ket{\psi} = \ket{\bar{\psi}}. \tag{2.40}$$

Through the same explanation as in equations (2.34) and (2.35) it can be concluded that the C operator only has two possible eigenvalues +1 and -1. The eigenvalue is called the charge parity of the particle. However, in comparison to the parity operator, most of the particles are not eigenstates of C. Applying the C operator on a proton state will result in an anti-proton state, but this is not just the original state multiplied with a scalar factor. Only particles with all internal quantum numbers being 0 can be eigenstates of C. Examples for such particles are the photon or bound states between particle and anti-particle like the neutral pion. If an eigenstate particle decays into a

particle-antiparticle system the equation

$$\eta_P = (-1)^{L+S} \tag{2.41}$$

can be used to calculate the charge parity η_P of the particle through the relative angular momentum L and the spin S of the system. [26, 28]

As with parity it was also assumed that a physical system is invariant under the charge conjugation. This was again disproven through the weak interaction. When applying the C operator onto the left-handed neutrino, the result would be a left-handed anti-neutrino. But a left-handed anti-neutrino was never observed and does not exist in the SM. Therefore, the SM is not invariant under charge conjugation. [26]

But this example shows that there is a way to make the SM invariant under the product of both symmetries, which is called CP-symmetry. If the C operator is applied on a left-handed neutrino it creates a left-handed anti-neutrino. If then the P operator is applied on the anti-neutrino state, the result is a right-handed anti-neutrino, which does exist in the SM. Therefore, it seems that the SM is invariant under CP-transformation. The nomenclature for this system is J^{PC} which describes the total angular momentum J and its intrinsic parity P and charge parity C. A particle is called CP-even, if the product of the parity and charge parity is $+1$, otherwise it is called CP-odd. If the particle is not an eigenstate of the operator, then this parameter is not given. As an example the SM Higgs boson is likely to have a charge parity of $+1$ and a parity of $+1$ with a spin of 0. This is written as $\text{J}^{\text{PC}} = 0^{++}$. However, experiments to determine the spin and parity of the Higgs boson are still performed and it is also tested if the Higgs boson is a mixture between a CP-even and CP-odd state. [29, 30]

Even though it was assumed that the product of C- and P-symmetry should be invariant in the SM, it was discovered that the SM also violates the CP-symmetry in some cases. The violation is caused by the effect of quark mixing. An example of this is the decay of the Kaons $K^0 = \bar{s}d$ and $\bar{K}^0 = s\bar{d}$. These Kaons are not eigenstates of the CP-operator

$$CP \left| K^0 \right\rangle = -C \left| K^0 \right\rangle = \left| \bar{K}^0 \right\rangle \tag{2.42}$$

$$CP \left| \bar{K}^0 \right\rangle = -C \left| \bar{K}^0 \right\rangle = \left| K^0 \right\rangle \tag{2.43}$$

but eigenstates can be constructed through linear combination

$$\left| K_1 \right\rangle = \frac{1}{\sqrt{2}} \left(\left| K^0 \right\rangle + \left| \bar{K}^0 \right\rangle \right) \tag{2.44}$$

$$\left| K_2 \right\rangle = \frac{1}{\sqrt{2}} \left(\left| K^0 \right\rangle - \left| \bar{K}^0 \right\rangle \right) . \tag{2.45}$$

$\left| K_1 \right\rangle$ is the eigenstate with the eigenvalue $+1$ and $\left| K_2 \right\rangle$ the eigenstate with the eigenvalue -1. Kaons usually decay into a number of pions. If CP is conserved in the SM, K_1 can only decay into a CP-even state, which consists of 2 pions, while K_2 can only decay into a CP-odd state, which consists of 3 pions. Furthermore, K_1 decays faster than K_2. This can be used in an experiment to produce a K_2

beam. It starts with a K^0 beam consisting of K_1 and K_2

$$|K^0\rangle = \frac{1}{\sqrt{2}} \left(|K_1\rangle + |K_2\rangle \right).$$
(2.46)

Because of the shorter lifetime K_1 decays faster, which leaves only K_2 in the beam. This means, that only 3 pion final states should then be observed if CP is conserved. But the observation shows that there are still 2 pion final states, which means that CP conservation is violated. [28]

It is possible to add a third symmetry to the C- and P-symmetry to get an invariance in the SM. This is the time symmetry, which contains an operator that reverses the time of a system. All three together are called CPT-symmetry and until now there was no process found that violates this symmetry. [28]

2.2 The two-Higgs-doublet model

2.2.1 Problems of the Standard Model

The previous section showed the basics of the SM, the currently most precise description of elementary particles and their interactions. Still, the SM is not able to explain every experimental observation. The first problem was already mentioned. As experiments show, neutrinos need to have a small mass to be able to change their flavour. But the SM can not explain this mass, as the neutrinos do not interact with the Higgs field. Therefore, they should have a mass of 0 like the photon and gluon. Another example is the mass of dark matter. The existence of dark matter was proven by the measurement of galaxy rotation curves, which describe the rotation velocity in dependence on the distance from the center of the galaxy. To explain the observed distribution between these two parameters, there has to be more mass than can be directly detected. This missing or hard-to-detect mass is called dark matter. While the SM itself has particles which could be part of the dark matter, i. e. the neutrinos, it can be shown that these alone can not make up the whole mass of the dark matter, which is needed to explain the distributions of the galaxy rotation curves. Therefore, other currently unknow particles must exist. [20]

In this section the focus will be on a third observation: the measurement of the anomalous magnetic moment of the muon a_μ. The anomalous magnetic moment of the muon consists of all the contributions to the value of the magnetic moment, that originate from quantum mechanical effects. The magnetic moment on tree level can be calculated with the Dirac equation predicting a magnetic moment of $g = 2$. This prediction only includes tree level Feynman diagrams. If Feynman diagrams with loops are also taken into account, then there is an additional contribution and the anomalous magnetic moment of the muons is defined by

$$a_\mu = \frac{g_\mu - 2}{2}$$
(2.47)

where g_μ is the real magnetic moment, that can be measured through experiments. In experiments the value of the anomalous magnetic moment is already measured very precisely and it is also predicted in the SM. The values found in both cases are

$$a_\mu^{exp} = 116\,592\,091\,(63) \cdot 10^{-11}$$
(2.48)

$$a_\mu^{SM} = 116\,591\,776\,(44) \cdot 10^{-11}$$
(2.49)

what shows, that there is still a slight deviation between the prediction and the experiment

$$a_\mu^{exp} - a_\mu^{SM} = 313\,(77) \cdot 10^{-11}. \tag{2.50}$$

While this deviation is small, it can not be explained with the SM. Therefore, this deviation might be a hint at a model beyond the SM. [31]

2.2.2 Basics of the two-Higgs-doublet model

As it was explained in section 2.1.3 the Higgs mechanism predicts a new Higgs field, which consists of the doublet

$$\Phi = \begin{pmatrix} \phi^+ \\ \phi^0 \end{pmatrix}. \tag{2.51}$$

The two-Higgs-doublet model (2HDM) predicts, that there is a secondary Higgs doublet in addition to the one that was already proven. This leads to a more complex Higgs potential

$$V(\Phi_1, \Phi_2) = m_{11}^2 \Phi_1^\dagger \Phi_1 + m_{22}^2 \Phi_2^\dagger \Phi_2 - \left\{ m_{12}^2 \Phi_1^\dagger \Phi_2 + H.c. \right\} \tag{2.52}$$
$$+ \frac{\lambda_1}{2} \left(\Phi_1^\dagger \Phi_1 \right)^2 + \frac{\lambda_2}{2} \left(\Phi_2^\dagger \Phi_2 \right)^2 + \lambda_3 \left(\Phi_1^\dagger \Phi_1 \right) \left(\Phi_2^\dagger \Phi_2 \right)$$
$$+ \lambda_4 \left(\Phi_1^\dagger \Phi_2 \right) \left(\Phi_2^\dagger \Phi_1 \right) + \frac{1}{2} \left\{ \lambda_5 \left(\Phi_1^\dagger \Phi_2 \right)^2 + H.c. \right\}$$
$$+ \left\{ \left[\lambda_6 \left(\Phi_1^\dagger \Phi_1 \right) + \lambda_7 \left(\Phi_2^\dagger \Phi_2 \right) \right] \Phi_1^\dagger \Phi_2 + H.c. \right\}$$

with the two doublets Φ_1 and Φ_2 in the same form as in (2.17). The parameters $m_{12}^2, \lambda_5, \lambda_6$ and λ_7 can be complex parameters[1]. [32]

Because of the second Higgs doublet there are now two VEVs v_1 and v_2 and their ratio is defined by the $\tan\beta$ parameter

$$\tan\beta = \frac{v_2}{v_1}. \tag{2.53}$$

For simplification, the two Higgs doublets are rotated by an angle α, so that one doublet has the VEV of the SM

$$v = \sqrt{v_1^2 + v_2^2} = 246\,\text{GeV} \tag{2.54}$$

and the other doublet a VEV of zero. The result leads to a total of five Higgs bosons. The first two bosons are the CP-even neutral Higgs bosons h and H, where $m_h < m_H$. Both bosons correspond to the mixture between both doublets with a mixing angle $(\alpha - \beta)$. The other three bosons are two CP-even charged Higgs bosons $H^\pm$ and one neutral CP-odd Higgs boson A. These three correspond to the second doublet with a VEV of zero. In theory, the masses of the Higgs bosons are independent and the mass of the light CP-even Higgs boson is set to the observed value of $125\,\text{GeV}$[2]. In addition to the masses, the parameters $\tan\beta$, the cosine of the mixing angle $\cos(\alpha - \beta)$ and three of the λ parameters are chosen to be independent. In this case these are λ_1, λ_6 and λ_7. [32]

---

[1] For the specific 2HDM that is analysed in this thesis (see section 2.2.3), those parameters are real as CP violation does not enhance the value of the anomalous magnetic moment of the muon.

[2] There is the possibility, that the observed Higgs boson might be the heavy CP-even Higgs boson, but the probability for this scenario is low, because most of the masses for the light CP-even Higgs boson are already excluded.

2.2.3 The flavour-aligned 2HDM

After the general description of the 2HDM, the focus will now be on the specific model that is used in this thesis: the flavour-aligned 2HDM. With two different Higgs fields, there are two different Yukawa matrices, that couple to the fermion fields. However, this leads to a problem with the coupling to the right-handed fermion fields. Two matrices result in flavour-changing interactions. This should be avoided, because then these matrices can not be diagonalised at the same time. The method used by the flavour-aligned 2HDM to solve this problem, is the alignment of the flavour space of the Yukawa couplings of the two Higgs doublets. The simplest way to include this is the assumption that the SM-like doublet has the Yukawa couplings of the SM and the second doublet has Yukawa couplings proportional to those of the Higgs doublet. This means that the Yukawa matrices are also proportional and can be diagonalised simultaneously. The Yukawa couplings of the second Higgs doublet are defined by proportionality factors to the couplings of the SM ζ_l, ζ_d and ζ_μ. For example $\zeta_l = 50$ means that the second Higgs doublet has a 50 times higher coupling to leptons than the SM. There are four different types of the 2HDM with different couplings to the parameters listed in the table of figure 2.4. [33]

However, these types have different problems for the specific case of this thesis. As it was mentioned in section 2.2.1 the new model should be able to explain the difference between the measurement and the prediction of the anomalous magnetic moment of the muon. And it can be seen in figure 2.5 that the 2HDM is able to explain the deviation. The figure shows the current deviation between the experimental result and the prediction of the SM with the yellow band. The blue, red and grey areas represent the contributions of the 2HDM to the magnetic moment of the muon for different values of ζ_l. In these figures the coupling to up-type quarks is set to the maximum value that is not already excluded by different experiments (see section 2.2.5). The figures show that the 2HDM can only explain the deviation if the mass of the CP-odd Higgs boson is low. This will be the reason why the analysis searches for a light CP-odd Higgs boson. But first, the more interesting fact is that the contributions are also only high enough, if the coupling to leptons and up-type quarks are large at the same time. The problem with this requirement is that it is not obtainable with the four presented models. In the type II and X model, ζ_μ is proportional to $\cot(\beta)$ while ζ_l is proportional to $-\tan(\beta)$. This means that it is impossible for both couplings to be large at the same time. On the other hand the type Y model is very heavily constrained by $b \to s\gamma$ measurements [34], because the product $|\zeta_\mu \zeta_d|$ is never small. And while this product can be small for the type I model, this would also imply that ζ_μ and ζ_l are small, which means that this model can not explain the deviation of the magnetic

	Type I	Type II	Type X	Type Y
ζ_u	$\cot\beta$	$\cot\beta$	$\cot\beta$	$\cot\beta$
ζ_d	$\cot\beta$	$-\tan\beta$	$\cot\beta$	$-\tan\beta$
ζ_l	$\cot\beta$	$-\tan\beta$	$-\tan\beta$	$\cot\beta$

Figure 2.4: Proportionality factors for the different Yukawa couplings and models of the 2HDM [32]
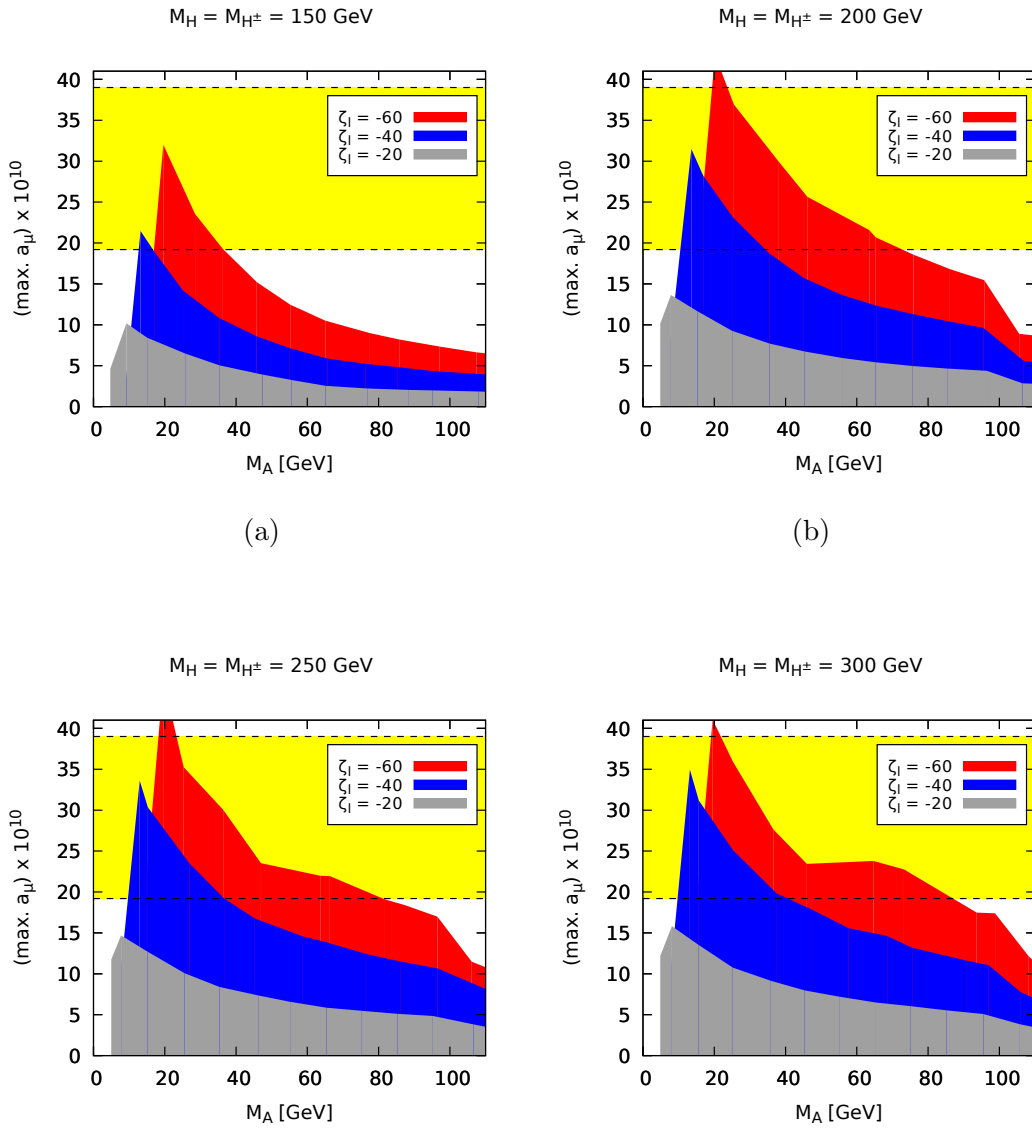
Figure 2.5: Contributions of the 2HDM to the anomalous magnetic moment of the muon for different masses $m_{H^\pm}$, m_A and different couplings to leptons. In all cases, the coupling to up-type quarks is set to the maximum possible value allowed by experimental results. [32]

moment between the experiment and the SM prediction. Therefore, the assumption of the new theory
is that the couplings are independent from each other. [32]

2.2.4 Production and Decay of the CP-odd Higgs boson

At first it is required to define the parameters of interest. As it was mentioned before, the motivation
of this theory is to explain the deviation between the measurement and the SM prediction of the
anomalous magnetic moment of the muon. And as shown in figure 2.5 the CP-odd Higgs boson A has
to be light for the contributions to be high enough. Therefore, finding a light CP-odd Higgs boson
would be evidence for this theory. The light CP-odd Higgs boson can be produced at the LHC through
gluon fusion with a quark loop. Because the contribution to the anomalous magnetic moment of the
muon by ζ_d is negligible, the coupling to down-type quarks is assumed to be significantly smaller
than the coupling to up-type quarks. This means that the A boson is produced primarily through a
top-quark loop. Like the production, the decay of the boson is defined by the couplings. Because the
couplings to leptons is assumed to be large in comparison to the other couplings, the A boson decays
almost always into a pair of leptons. And because the τ leptons have the highest mass, the branching
ratio for $A \rightarrow \tau\tau$ is almost 100%. This leads to the process that can be seen in figure 2.6 and it
shows that the most important parameters will be the coupling to up-type quarks and the coupling
to leptons. [32]

2.2.5 Constraints on the parameters

In section 2.2.3 it was shown that the couplings to leptons and up-type quarks need to be large
in the 2HDM for the contributions to be high enough. But these couplings are parameters of the
flavour-aligned 2HDM and therefore, they are constrained by different experimental results. In this
section the constraints on the couplings to leptons and up-type quarks are presented, because these
two parameters are most important for the analysis. For a continued research on constraints, see [32].
First, it is shortly explained how the upper limits are calculated. After that, there will be more details
about the limits of the lepton and up-type quark coupling. Because the 2HDM is an extension of the
SM, it includes the same particles as the SM together with the introduction of four additional Higgs
bosons. For different physical processes this then results into new Feynman diagrams with the same
initial and final state, but different processes in comparison to the SM. These are the contributions
of the 2HDM to this process. The amount of these contributions is dependent on the parameters of
the 2HDM. For example higher couplings usually lead to an increase in the contributions. However,
these processes were already measured. So contributions of the 2HDM can not be too large, otherwise
the theory would contradict the data. Therefore, certain values of parameters or combination of
parameters can be excluded with experiments. The mathematical background for the calculation of
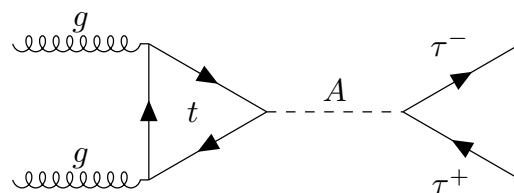
Figure 2.6: Production and decay of the CP-odd Higgs boson

upper limits will be presented in section 2.3.1.

First the limits on the lepton coupling are analysed. For this different processes will be examined. The contributions of the 2HDM to these processes increase with stronger lepton coupling. This means, that only upper limits can be calculated for ζ_l or to be more precise for $|\zeta_l|$. These limits are shown in figure 2.7. The processes constraining the lepton coupling differ in certain areas. In the area $5\,\text{GeV} < m_A < 20\,\text{GeV}$ the ζ_l value is mostly constrained by the LEP process $ee \to \tau\tau(A) \to \tau\tau(\tau\tau)$. In this process the electron pair creates a Z boson, that decays into a τ pair afterwards. One of those τ leptons can create a short-lived A boson, that decays into a secondary pair of τ leptons. The process is shown in figure 2.8. It reduces the maximum value of ζ_l in this mass area to 30. For masses m_A above 20 GeV, two other processes become dominant depending on the mass of the $m_{H\pm}$ bosons. For $m_{H\pm} < 250\,\text{GeV}$ the upper limit of ζ_l is constrained by the τ decay $\tau \to \mu\nu_\tau\bar{\nu}_\mu$. It can be seen in figure 2.7 that these constraints become weaker for higher Higgs boson masses. Above Higgs boson masses of 250 GeV the distribution changes, which indicates that another process is becoming dominant in constraining the upper limit. This process is the leptonic Z boson decay $Z \to ll$. Both processes limit the upper value of ζ_l to around 50 to 100. Furthermore, the Z boson decay puts heavier constraints on the upper limit and therefore, it can be concluded that higher masses $m_{H\pm}$ would not lead to significantly higher upper limits of ζ_l for most masses m_A. This means, that the upper limit for the lepton coupling is about 100. [32]

Now the upper limits for the second parameter, the coupling to up-type quarks, are presented. This parameter is constrained by B-physics measurements and LHC searches for a light CP-odd Higgs boson A. The processes observed in the B-physics are $b \to s\gamma$ and $B_s \to \mu^+\mu^-$ shown in figure 2.9. The Feynman diagrams contain the Higgs bosons h,H,A and H$^\pm$ with couplings to leptons, up-type quarks and down-type quarks. Therefore, the contributions of the 2HDM to these two processes are dependent on all the Higgs boson masses and all the couplings ζ_l, ζ_u, and ζ_d. This means that the upper limits of the up-type quark coupling is dependent on more parameters than the coupling to leptons. In figure 2.10 the allowed parameter values after each experiment for ζ_u can be seen for different masses m_A, different lepton couplings ζ_l and different down-type quark couplings ζ_d. It can be seen, that both experiments allow high values of $|\zeta_u|$. But if they are both combined, the maximum value of $|\zeta_u|$ is only around 0.5 with the exception of some small areas. These figures do not show the influence of the other parameters like the masses of the Higgs bosons. These dependencies can be seen in figure 2.11, where the upper limits on ζ_u from experiments at the LHC are also included. The results of the B-physics experiments show that there is no relevant difference in the maximum value of ζ_u. It depends slightly on the masses m_A and m_H and also the lepton coupling ζ_l. The maximum value always ranges between 0.3 and 0.7. The measurements from the LHC show a stronger dependence. First it can be seen in figures 2.11b, 2.11c and 2.11d that the upper limit on ζ_u decreases heavily for all ζ_l, if A has a mass of 100 GeV or higher. In this case the process constraining ζ_u is $pp \to A \to \tau\tau$ with A having a higher mass than the Z boson. This case was already researched before [35] and because the coupling to up-type quarks directly increases the production rate, this search heavily constraints the upper limit on ζ_u. Another special case can be observed in figure 2.11a, where the constraining process is $pp \to H \to \tau\tau$. Here $m_H = 150\,\text{GeV}$ and it can be seen, that there is a significant drop in the upper value for $m_A > 75\,\text{GeV} = m_H/2$. In this area, the process $H \to AA$ is suppressed and therefore H mostly decays into a pair of τ. But as it was said before, the case of a Higgs boson heavier than a Z boson was already researched [35]. Together with the fact that ζ_u also
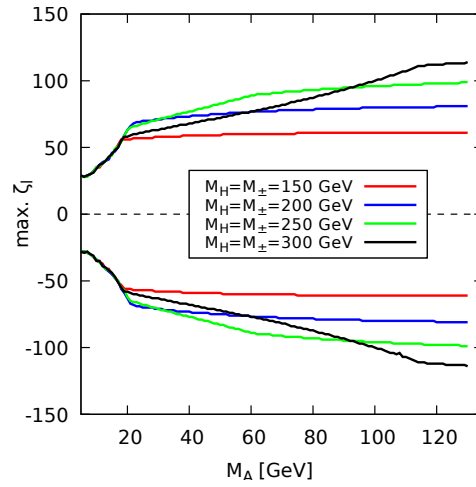
Figure 2.7: Maximum values of the Yukawa coupling to leptons for the second Higgs doublet given for different constraints and dependent on the mass of the CP-odd, heavy CP-even and charged Higgs bosons [32]
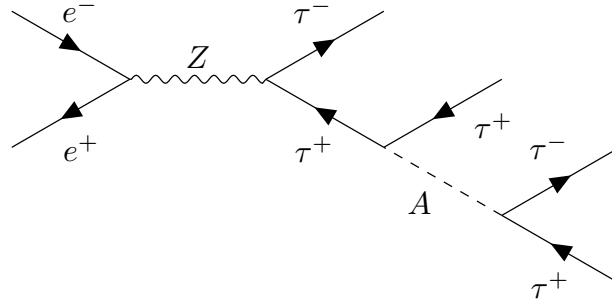
Figure 2.8: Feynman diagram for the production of low mass CP-odd Higgs bosons in the process $ee \to \tau\tau(A) \to \tau\tau(\tau\tau)$

(a)   (b)
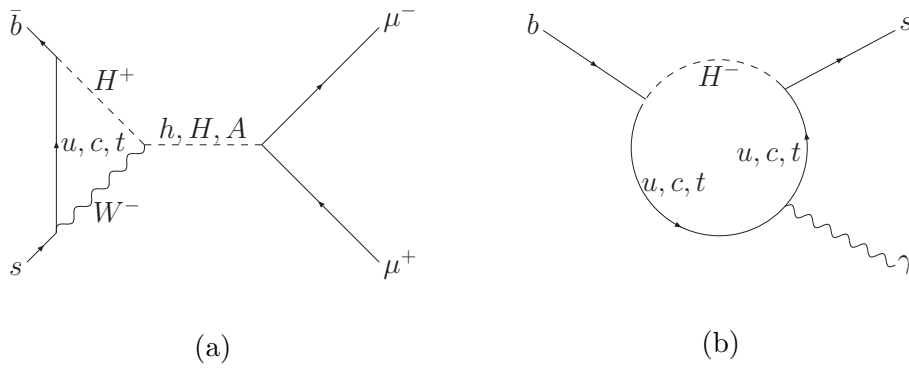
Figure 2.9: Feynman diagrams for the observables, that constrain the up-type quark coupling (a) $B_s \to \mu^+\mu^-$ (b) $b \to s\gamma$ [32]
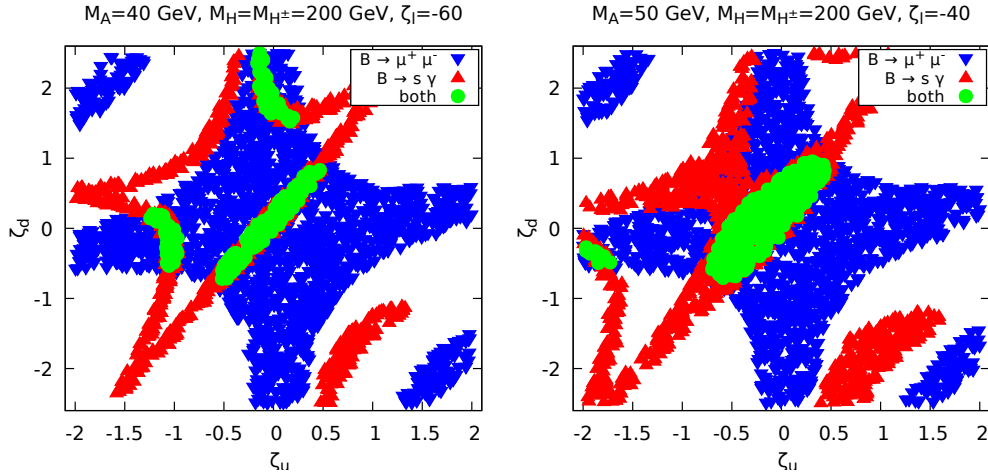
Figure 2.10: Maximum allowed values of ζ_u and ζ_d for masses $m_H = m_{H\pm} = 200\,\text{GeV}$ and (a) $m_A = 40\,\text{GeV}$, $\zeta_l = -60$ (b) $m_A = 50\,\text{GeV}$, $\zeta_l = -40$ [32]

determines the production rate of H, the upper value is heavily constrained in this area. The last case is $m_A < m_Z$ and $m_A < m_H/2$. In this area the process $H \to AA$ is kinematically allowed and the constraints come from the process $pp \to H \to \tau\tau$. But in this case H can also decay into a pair of A bosons. This means, that the contributions of the process $H \to \tau\tau$ can not only be suppressed by reducing ζ_u, but also by increasing the coupling between the Higgs bosons C_{HAA}. So, the constraints on ζ_u are not as strong as before and there can even be some spikes in the upper limits seen in figure 2.11b, 2.11c and 2.11d. In summary, the upper limit for ζ_u is in most cases around 0.5, because of the limits from B-physics results. However, this upper limit can change mostly depending on the masses of the Higgs bosons and can even be 0.2 in some special cases. [32]
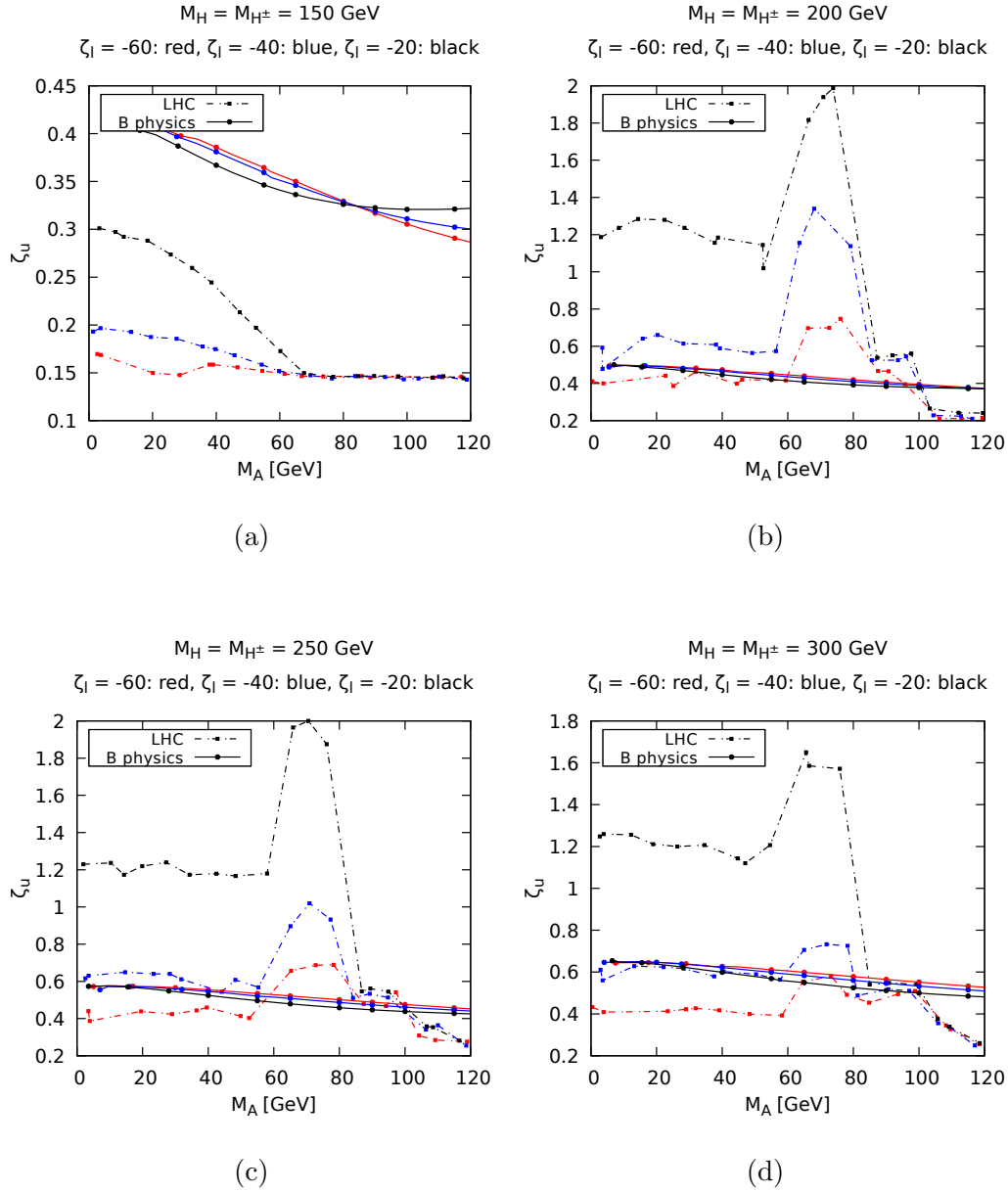
Figure 2.11: Maximum allowed values of ζ_u in dependence of LHC and B-physics results and of different masses and lepton couplings [32]

2.3 Statistics

In the collision of two protons a lot of different particles can be created. But the exact process that is generated in a certain collision can not be predicted with 100% accuracy. Therefore, it is important to repeat the experiment to be able to make a justified statement about the possible existence of a CP-odd Higgs boson. This means that large amounts of events from proton-proton collisions have to be analysed. However, using a high number of events requires a statistical analysis. This section explains the most important statistical terms and tests used in this thesis.

2.3.1 Likelihood Ratio Tests

In this section the general process of a statistical analysis used later in calculating limits is presented. When looking into new signal processes two hypotheses H_0 and H_1 are usually defined. H_0 is called the null hypothesis and normally describes the current theory, in this case the SM theory. Therefore, this hypothesis describes the background of the analysis. The alternative hypothesis is H_1, which is the SM theory but with the addition of the new signal process. So it describes the sum of background and signal in the analysis. To test the truth of both hypotheses, a likelihood ratio test is used. For this, a parameter μ is introduced that acts as a signal strength scale factor. If a histogram with N bins is assumed with the distribution $(n_1, n_2, ..., n_N)$ then the number of expected events in bin i can be written as

$$E[n_i] = \mu s_i + b_i \tag{2.55}$$

where s_i and b_i are the expected numbers of signal and background events in the specific bin i. The hypothesis H_0 is now defined as a theory with $\mu = 0$ and the hypothesis H_1 is usually defined as a theory with $\mu = 1$. Then the likelihood function is a product of Poisson probabilities

$$L(\mu) = \prod_{j=1}^{N} \frac{(\mu s_j + b_j)^{n_j}}{n_j!} e^{-(\mu s_j + b_j)} \tag{2.56}$$

with n_j being the number of data events found in bin j. However, the likelihood function is also dependent on different nuisance parameters θ. To determine or constrain these nuisance parameters, additional measurements are done that lead to new distributions $(m_1, m_2, ..., m_M)$. With this, the expected values for each bin i are

$$E[m_i] = u_i(\theta) \tag{2.57}$$

with u_i being quantities depending on the nuisance parameters $\theta = (\theta_s, \theta_b, b_{tot})$. The complete likelihood function is

$$L(\mu) = \prod_{j=1}^{N} \frac{(\mu s_j + b_j)^{n_j}}{n_j!} e^{-(\mu s_j + b_j)} \prod_{k=1}^{M} \frac{u_k^{m_k}}{m_k!} e^{-u_k} \quad . \tag{2.58}$$

To test the potential values of μ a profile likelihood ratio is built

$$\lambda(\mu) = \frac{L(\mu, \hat{\hat{\theta}})}{L(\hat{\mu}, \hat{\theta})} \tag{2.59}$$

where $\hat{\mu}$ and $\hat{\theta}$ are maximum likelihood estimators, which means that they maximize the likelihood function. In comparison to that, $\hat{\hat{\theta}}$ is the maximum likelihood estimator for a specific value μ. This means that these nuisance parameters $\hat{\hat{\theta}}$ maximize the Likelihood function for a specific value μ. It is theoretical possible for $\hat{\mu}$ to be smaller than 0. However, in most cases this does not make sense as this would imply a negative signal. Therefore, the profile likelihood ratio is more often defined as

$$\tilde{\lambda}(\mu) = \begin{cases} \frac{L(\mu, \hat{\hat{\theta}}(\mu))}{L(\hat{\mu}, \hat{\theta})} & \hat{\mu} \geq 0, \\ \frac{L(\mu, \hat{\hat{\theta}}(\mu))}{L(0, \hat{\hat{\theta}}(0))} & \hat{\mu} < 0. \end{cases} \tag{2.60}$$

It can be seen that $\lambda(\mu)$ ranges between 0 and 1. A value close to 1 implies a good agreement between data and theorized value of μ. For further analysis the test statistic

$$\tilde{t}_\mu = -2 \ln \tilde{\lambda}(\mu) = \begin{cases} -2 \ln \frac{L(\mu, \hat{\hat{\theta}}(\mu))}{L(\hat{\mu}, \hat{\theta})} & \hat{\mu} \geq 0, \\ -2 \ln \frac{L(\mu, \hat{\hat{\theta}}(\mu))}{L(0, \hat{\hat{\theta}}(0))} & \hat{\mu} < 0 \end{cases} \tag{2.61}$$

is used. With this test statistic, the first statistical analysis can be done by defining a value that describes the discrepancy between data and hypothesis. This value is called p-value and can be calculated through

$$p_\mu = \int_{\tilde{t}_{\mu,\text{obs}}}^{\infty} f\left(\tilde{t}_\mu | \mu\right) d\tilde{t}_\mu \tag{2.62}$$

where $\tilde{t}_{\mu,\text{obs}}$ is the value of the statistic $\tilde{t}_\mu$ observed from the data. $f\left(\tilde{t}_\mu | \mu\right)$ is the probability density function (PDF) of $\tilde{t}_\mu$ with an assumed signal strength μ. These PDFs are usually not known and therefore have to be determined. One way is by producing pseudo experiments. With this option, random data events for the bins are generated in dependence on the parameter μ and the nuisance parameters θ. However, this method requires the creation of a high number of pseudo experiments. This results in a lot of computing time. A better method is therefore to simplify the test statistic. Through the Wilks theorem [36] and the Wald approximation [37], $\tilde{t}_\mu$ can be written as

$$\tilde{t}_\mu = \begin{cases} \frac{(\mu - \hat{\mu})^2}{\sigma^2} & \hat{\mu} \geq 0 \\ \frac{\mu^2}{\sigma^2} - \frac{2\mu\hat{\mu}}{\sigma^2} & \hat{\mu} < 0 \end{cases} \tag{2.63}$$

where it is assumed that $\hat{\mu}$ follows a Gaussian distribution with the mean μ' and the standard derivation σ. This leads to the PDF

$$f(\tilde{t}_\mu | \mu') = \frac{1}{2} \frac{1}{\sqrt{2\pi}} \frac{1}{\sqrt{\tilde{t}_\mu}} \exp\left[-\frac{1}{2} \left(\sqrt{\tilde{t}_\mu} + \frac{\mu - \mu'}{\sigma} \right)^2 \right]$$
$$+ \begin{cases} \frac{1}{2} \frac{1}{\sqrt{2\pi}} \frac{1}{\sqrt{\tilde{t}_\mu}} \exp\left[-\frac{1}{2} \left(\sqrt{\tilde{t}_\mu} + \frac{\mu - \mu'}{\sigma} \right)^2 \right] & \tilde{t}_\mu \leq \mu^2/\sigma^2 \\ \frac{1}{\sqrt{2\pi}(2\mu/\sigma)} \exp\left[-\frac{1}{2} \frac{\left(\tilde{t}_\mu - \frac{\mu^2 - 2\mu\mu'}{\sigma^2} \right)^2}{(2\mu/\sigma)^2} \right] & \tilde{t}_\mu > \mu^2/\sigma^2 \end{cases} \tag{2.64}$$

which is faster to calculate as long as σ and μ' are known. These values can be found through the measured data. [38]

The p-value describes the probability for a statistical model to get the same or an even more extreme observed value $\tilde{t}_{\mu,\mathrm{obs}}$ when repeating the measurement [39]. An illustration of that principle can be seen in figure 2.12. The p-value is often used to describe that a specific model is not comparable to the measured data. If the p-value for a hypothesis with value μ is below a certain threshold α, then this hypothesis can be excluded with a confidence level of $1-\alpha$. α is usually set to 0.05, so that a hypothesis can be excluded with a 95% confidence level. This represents a significance of $Z = 2$. However, when discovering a new particle the p-value has to be much lower $p_\mu < 2.87 \cdot 10^{-7}$ which corresponds to a significance of $Z = 5$. This will be explained in more detail in section 2.3.2. [38,40]

The problem with the p-value is that it can only exclude one hypothesis. But like the 2HDM a lot of theories are dependent on different parameters. So it becomes hard to exclude the whole theory with every combination of parameters. Therefore, another likelihood ratio test can be used where upper limits for certain parameters are defined. Values of these parameters above the upper limits can be excluded with a certain confidence level. This was mentioned already in section 2.2.5, where constraints on the parameters of the 2HDM were found. The general calculation of upper limits is similar to the calculation of the p-value. The difference is, that the test statistic (2.61) is slightly modified. In the case of defining an upper limit for the parameter μ, it is reasonable to assume that the upper limit should be higher than the maximum likelihood estimator $\hat{\mu}$. Otherwise this would mean that data with $\hat{\mu} > \mu$ represents less compatibility with μ than the measured data. This transforms equation (2.61) into

$$\tilde{q}_\mu = \begin{cases} -2\ln\tilde{\lambda}(\mu) & \hat{\mu} \le \mu \\ 0 & \hat{\mu} > \mu \end{cases} = \begin{cases} -2\ln\frac{L(\mu,\hat{\hat{\theta}}(\mu))}{L(0,\hat{\hat{\theta}}(0))} & \hat{\mu} < 0 \\ -2\ln\frac{L(\mu,\hat{\hat{\theta}}(\mu))}{L(\hat{\mu},\hat{\theta})} & 0 \le \hat{\mu} \le \mu \\ 0 & \hat{\mu} > \mu \end{cases} \qquad (2.65)$$

Like in equation (2.62) a p-value can be calculated with the new test statistic $\tilde{q}_\mu$

$$p_\mu = \int_{\tilde{q}_{\mu,\mathrm{obs}}}^{\infty} f(\tilde{q}_\mu | \mu, \hat{\hat{\theta}}(\mu, \mathrm{obs})) d\tilde{q}_\mu \qquad (2.66)$$
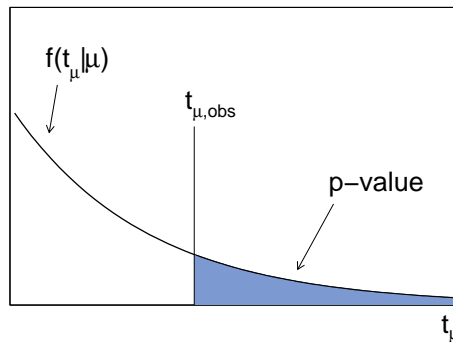
Figure 2.12: Illustration of the p-value calculated from an observed value $\tilde{t}_{\mu,\mathrm{obs}}$ [38]

with $\tilde{q}_{\mu,\text{obs}}$ being the value for the test statistic found through the observed data. $f(\tilde{q}_\mu|\mu, \hat{\hat{\theta}}(\mu, \text{obs}))$ is the PDF of $\tilde{q}_\mu$ under a certain value μ and its nuisance parameters $\hat{\hat{\theta}}(\mu)$ that maximize the likelihood function. As with the calculation of the p-value before, this PDF is not known and has to be either calculated by generating pseudo experiments or by simplifying the test statistic through Wilks theorem [36] and the Wald approximation [37]

$$\tilde{q}_\mu = \begin{cases} \frac{\mu^2}{\sigma^2} - \frac{2\mu\hat{\mu}}{\sigma^2} & \hat{\mu} < 0 \\ \frac{(\mu-\hat{\mu})^2}{\sigma^2} & 0 \le \hat{\mu} \le \mu \\ 0 & \hat{\mu} > \mu \end{cases} \tag{2.67}$$

which then leads to the PDF

$$\begin{aligned} f(\tilde{q}_\mu|\mu') = {} & \Phi\left(\frac{\mu'-\mu}{\sigma}\right)\delta(\tilde{q}_\mu) \\ & + \begin{cases} \frac{1}{2}\frac{1}{\sqrt{2\pi}}\frac{1}{\sqrt{\tilde{q}_\mu}}\exp\left[-\frac{1}{2}\left(\sqrt{\tilde{q}_\mu} - \frac{\mu-\mu'}{\sigma}\right)^2\right] & 0 < \tilde{q}_\mu \le \mu^2/\sigma^2 \\ \frac{1}{\sqrt{2\pi}(2\mu/\sigma)}\exp\left[-\frac{1}{2}\frac{(\tilde{q}_\mu - (\mu^2 - 2\mu\mu')/\sigma^2)^2}{(/2\mu/\sigma)^2}\right] & \tilde{q}_\mu > \mu^2/\sigma^2 \end{cases} \end{aligned} \tag{2.68}$$

with $\Phi(x)$ being the cumulative function of the Gaussian distribution. The p-value is calculated for different $\mu > \hat{\mu}$ with $\mu = \mu'$ and for every μ with a $p_\mu < 0.05$ the value of the hypothesis is excluded with a confidence level of 95%. [38]

However, this method can lead to stronger limits than expected, if the signal is small compared to the background and if the uncertainties are high. Therefore, the p-value is modified so that it includes background measurements into the calculation of upper limits. This is illustrated in figure 2.13. The new p-value is calculated through [41, 42]

$$p'_\mu = \frac{p_\mu}{1 - p_b} \tag{2.69}$$

with

$$p_b = 1 - \int_{\tilde{q}_{\mu,\text{obs}}}^\infty f(\tilde{q}_\mu|0, \hat{\hat{\theta}}(0, \text{obs}))d\tilde{q}_\mu. \tag{2.70}$$

Instead of using real data, the upper limit can also be calculated through an artificial data set, called Asimov data. This is used to determine the sensitivity of the analysis based on the background and signal prediction alone. An Asimov data set is defined such that the true values of the parameters are obtained if the data set is used to evaluate the maximum likelihood estimators for all parameters. This holds true if the number of Asimov data events in a bin i is equal to the expected value

$$n_{i,A} = E_{\mu'}[n_i] = \mu's_i + b_i. \tag{2.71}$$

From this an Asimov likelihood L_A can be derived together with its profile likelihood ratio λ_A. This leads to the standard derivation σ_A of the distribution around $\hat{\mu}$

$$\sigma_A^2 = \frac{(\mu-\mu')^2}{q_{\mu,A}} \tag{2.72}$$
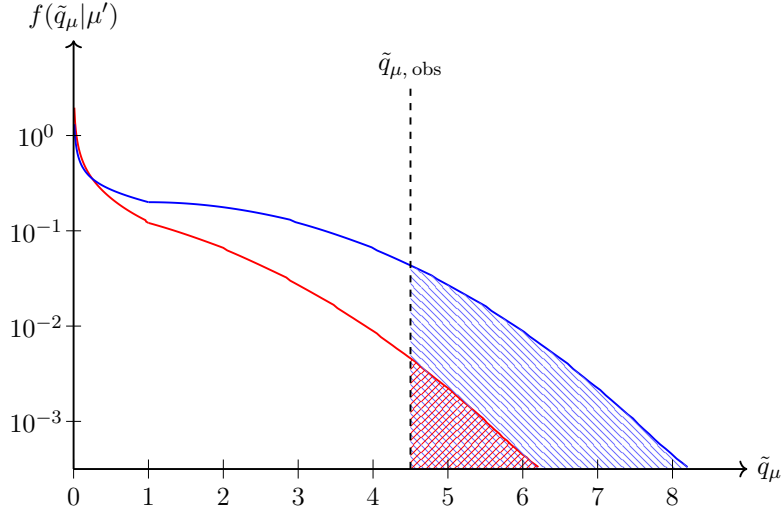
Figure 2.13: Illustration of the modified p-value calculation. The blue line represents the test statistic for the background with $\mu' = 0$ and the red line represents the signal test statistic with $\mu' = \mu$. [41]

with $q_{\mu,A} = -2 \ln \lambda(\mu)$ being the median of the PDF $f(q_{\mu,A}|0)$. Because the exclusion significance is searched for the hypothesis without signal, μ' has to be set to zero

$$\sigma_A^2 = \frac{\mu^2}{q_{\mu,A}}. \tag{2.73}$$

The result from this upper limit calculation is then called the expected limit and describes the lowest possible upper rejection of the signal hypothesis in the case that the background hypothesis is true. Furthermore, additional bands of the upper limits with $\pm N\sigma$ can be calculated through a variation of $\hat{\mu}$ by $N \cdot \sigma_A$ around μ'. [38,41]

2.3.2 Expected Discovery Significance

As it was mentioned in the previous section, the significance Z is defined through the p-value of a measurement. It is calculated through

$$Z = \Phi^{-1}(1 - p_\mu) \tag{2.74}$$

where Φ^{-1} is the inverse of the cumulative function of the Gaussian distribution. This is called the quantile. For example a significance of $Z = 5$ corresponds to a p-value of $2.87 \cdot 10^{-7}$, which is the threshold for the discovery of a new particle. This is the reason why the Higgs boson was discovered with a significance of over 5σ. However, this significance can only be calculated after the measurement. But sometimes it is important to know the expected significance of an analysis, because it directly shows its sensitivity and if it is even possible to discover a particle through this analysis. For the following calculation, it is assumed that there are no nuisance parameters and all events are found in

one bin. This reduces the likelihood function (2.56) to

$$L(\mu) = \frac{(\mu s + b)^n}{n!} e^{-(\mu s + b)} \tag{2.75}$$

with the maximum likelihood estimator

$$\hat{\mu} = \frac{n - b}{s}. \tag{2.76}$$

The test statistic is set to be the same as in equation (2.61) and because the background-only hypothesis is assumed to be true, $\mu = 0$. This leads to

$$\tilde{t}_{\mu=0} = q_0 = \begin{cases} -2\ln\frac{L(0)}{L(\hat{\mu})} & \hat{\mu} \geq 0 \\ 0 & \hat{\mu} < 0. \end{cases} \tag{2.77}$$

It can be shown, that [40]

$$Z = \sqrt{q_0} \tag{2.78}$$

which leads to a significance of 0, if $\hat{\mu} < 0$. This is to be expected as it means that there are more expected background events than measured data events and this results in the conclusion that an additional signal is not compatible with the data. However, if $\hat{\mu} \geq 0$ it leads to

$$Z = \sqrt{-2\ln\frac{L(0)}{L(\hat{\mu})}} = \sqrt{2\left[n\ln\left(\frac{n}{b}\right) - b + n\right]}. \tag{2.79}$$

The median significance for a value of $\mu = 1$ can be approximately calculated by setting $n = s + b$

$$Z = \sqrt{2\left[(s + b)\ln\left(\frac{s}{b} + 1\right) - s\right]} \tag{2.80}$$

which is the expected significance for a possible new process. [40, 43]

3 LHC and ATLAS

In this section the origin of the data used in this thesis for the search of a CP-odd Higgs boson is presented. For that, the section will be separated into two parts. In the first part, the experimental setup of the Large Hadron Collider (LHC), which is used to produce the particles, is explained. In the second part the ATLAS detector (A Toroidal LHC ApparatuS) will be presented. Its task is to measure the produced particles.

3.1 Large Hadron Collider

The LHC is a circular proton-proton accelerator and a part of CERN in the vicinity of Geneva. The LHC consists of a 27 km tunnel with two rings inside. In these rings, the protons are accelerated to a velocity almost as high as the speed of light. To make this possible, the protons have to travel without any interference. Therefore, the rings contain an ultra high vacuum with a pressure of only 10^{-10} to 10^{-11} mbar. To keep the protons on the right track, the rings are surrounded by superconducting electromagnets, that create a magnetic field of 8.3 tesla. To reach a superconductive state in these magnets, they have to be cooled down to -271.3°C. This is achieved by a system of liquid helium [44]. The energy of the protons has changed over the years. Currently each proton beam has an energy of 7 TeV resulting in a center-of-mass energy of 14 TeV. However, the data used in this thesis is taken from experiments over the years 2015 and 2016, where the center-of-mass energy was 13 TeV. The proton beams collide at different locations in the ring. These locations are the detectors of the LHC and they can be seen in figure 3.1. When the protons collide at these locations, different processes can happen. The probability for a process is represented by its cross-section $\sigma_{process}$. The cross-section can be predicted by the theory of the SM and with that, the number of events for this process over a certain time can be calculated as

$$N_{process} = L \cdot \sigma_{process}. \tag{3.1}$$

In this equation, L is the machine luminosity, which is dependent on different beam parameters

$$L = \frac{N_b^2 n_b f_{rev} \gamma_r}{4\pi \epsilon_n \beta^*} F. \tag{3.2}$$

N_b is the number of particles in a bunch and n_b the number of bunches inside a beam. At the LHC, one beam contains 2808 bunches with 10^{11} protons per bunch [45]. Furthermore, f_{rev} is the revolution frequency, γ_r the relativistic gamma factor, ϵ_n the normalized transverse beam emittance, β^* the beta function at the collision point of the protons and F the geometric luminosity reduction factor depending on the angle between the two beams at the collision point. Often not the luminosity itself is important, but the integrated luminosity. It describes the luminosity over a certain time. However, the integrated luminosity is not only dependent on the LHC, but also on the detectors. ATLAS and CMS are both high luminosity detectors, that are designed for a peak luminosity of
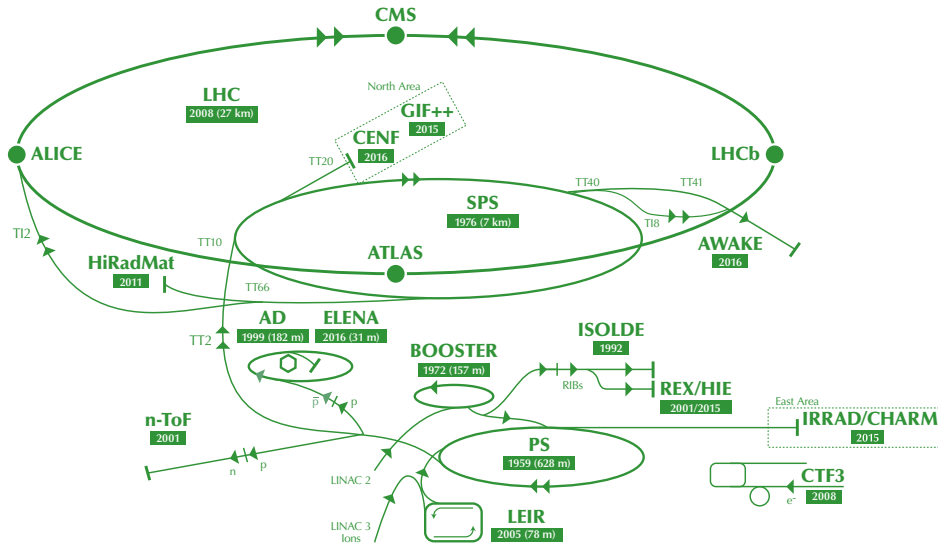
Figure 3.1: The CERN accelerator complex [45]

10^{34}cm^{-2}s^{-1}. These detectors are designed to measure a large amount of events to find events of processes that are very rare. Over the year 2017 both achieved an integrated luminosity of more than 50 fb$^{-1} = 10^{39}$cm^{-2} [46]. In this thesis, combined data from 2015 and 2016 measured by the ATLAS detector is used, what adds to an integrated luminosity of (36.1 ± 1.16) fb^{-1} [47]. The other two detectors are for low luminosity experiments. The LHCb experiment is studying b-quark physics at a peak luminosity of 10^{32}cm^{-2}s^{-1}. ALICE is an experiment for heavy ion measurements, where not protons beams, but lead beams are collided with a luminosity of 10^{27}cm^{-2}s^{-1}. [48]

3.2 The ATLAS detector

The ATLAS detector (A Toroidal LHC ApparatuS), shown in figure 3.2, has a height of 25 m and a length of 44 m with an overall weight of 7000 t. As the figure shows, it consists of several components, which are arranged cylindrical around the beam pipe. The protons collide at the center of the ATLAS detector. The created particles fly through the different layers of the detector and can then be detected. However, not all particles need to be detected. Most elementary particles have a short lifetime, i. e. the Z boson has a lifetime of approximately $3 \cdot 10^{-25}$s. This means that it can travel $9 \cdot 10^{-17}$m which is too short to reach the detector. Only the more stable decay products can be measured. These include electrons, muons, neutrinos, photons and hadrons. Therefore, the detector has to be built so that these decay products can be measured most effectively.

3.2.1 Coordinate system

Before the components of the ATLAS detector are described, its coordinate system has to be explained. The point of collision is the origin of the coordinate system. The beam line defines the z-axis, while the positive x-axis points towards the center of the LHC and the positive y-axis towards the surface of the earth. Because the plane of the x- and y-axis is transverse to the original direction of the particles it is called the transverse plane. Vectorial variables are split into a part parallel to the z-axis and a
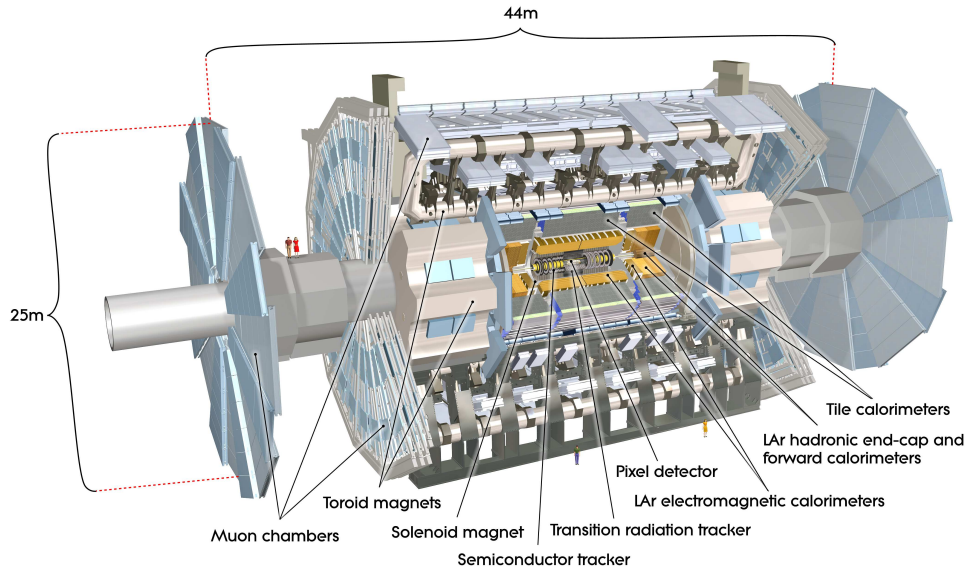
Figure 3.2: Overview of the ATLAS detector [49]

part parallel to the transverse plane. The variables parallel to the transverse plane get the subscript "T", i. e. the transverse momentum p_T. Like in cylindrical coordinates the azimuthal angle ϕ is defined around the z-axis in the x-y-plane, while the polar angle θ is the angle from the z-axis. Now, some new variables are defined. At first there is the pseudo rapidity:

$$\eta = -\ln\left(\tan\frac{\theta}{2}\right). \tag{3.3}$$

Then there is the missing transverse energy E_T^{miss} or the missing transverse momentum p_T^{miss}. These variables are important for processes with particles that can not be detected. In most cases these particles are neutrinos. As it was said in section 2.1.1 neutrinos can not be directly detected by the detector. But if there are neutrinos in a process they carry some energy. Independent from the process, conservation of energy is assumed. This means that if a neutrino appears during a process, the vectorial sum of the transverse energy of the measured particles does not add up to zero. This indifference is then regulated through the missing transverse energy. The last new variable is the distance in the η-ϕ space ΔR [49]:

$$\Delta R = \sqrt{(\Delta\phi)^2 + (\Delta\eta)^2}. \tag{3.4}$$

3.2.2 The inner detector

At the beginning the particles have to pass the inner detector, seen in figure 3.3. The main task of the inner detector is to record the tracks of the different particles. It is surrounded by a magnetic field of 2 T. The magnetic field curves the track of charged particles, which can be used to measure a particles momentum, its charge and vertex. The inner detector is divided into three parts: the Pixel detector, the Semiconductor Tracker (SCT) and the Transition Radiation Tracker (TRT). The
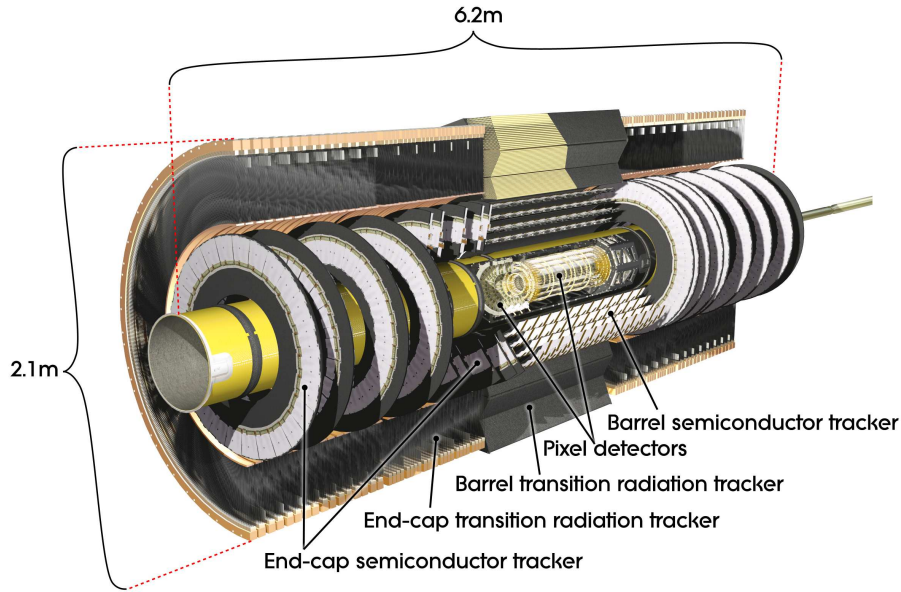
Figure 3.3: The inner detector of the ATLAS detector [49]

Pixel detector has the highest granularity and can therefore measure the tracks of the particles most precisely. This is the reason why it is the closest detector to the collision point. It consists of 1744 pixel sensors with 47232 pixels and 46080 readout channels for each sensor adding to a total of about 80.4 million readout channels. This leads to an accuracy of 10 μm in the transverse plain and 115 μm on the z-axis. The sensors of the pixel detector are semiconducting sensors like the eight strip layers of the Semiconducting Tracker. The basic idea of the SCT is that the incoming particles create electron-hole pairs, which are then read out. In the barrel region the SCT consists of small-angle stereo strips, where one set of strips is always parallel to the beam pipe. This layer measures the R-ϕ coordinates. In the end-cap region the SCT consist of two sets of strips, one radially and one at an angle of 40 mrad. This leads to an accuracy of 17 μm in the transverse plane and 580 μm in the direction of the z-axis. All combined, the SCT has approximately 6.3 million readout channels. The last part of the inner detector is the Transition Radiation Tracker, which consists of 73 straw tubes in the barrel region and 160 straw tubes in the end-cap region. These tubes have a diameter of 4 mm and they are filled with a gas mixture of 70% Xe, 27% CO_2 and 3% O_2 with an overpressure of 5-10 mbar. When a charged particle traverses this gas, it ionises it and creates electrons that drift towards the wire inside the tube. This signal is amplified and read out. In addition to that, there is space between the tubes filled with polymer fibres and foils to create transition radiation in the form of photons which ionise the gas as well. This effect is dependent on the Lorentz factor γ

$$\gamma = \frac{1}{\sqrt{1 - \frac{v^2}{c^2}}} \tag{3.5}$$

with v being the velocity of the particle and c being the speed of light. This factor is the highest for electrons, which means that the signal for an electron is significantly higher than for other particles. It can be used as an identification of the particle. The TRT has an accuracy of 130 μm per straw and a total number of around 351,000 readout channels. [49,50]

3.2.3 The Calorimeter System

The Calorimeter System of the ATLAS detector can be found around the inner detector. Other than the inner detector, which has to record the tracks of the particles, the task of this part is to measure the energy of the particles as precisely as possible. For this, the system is divided into two parts: the electromagnetic calorimeter and the hadronic calorimeter. Both can be seen in figure 3.4. The electromagnetic calorimeter has the task of measuring the energies of electrons and photons. It is built accordion shaped with the absorber material consisting of lead and the detector consisting of liquid argon. The accordion shape is used, because it provides a full ϕ coverage without any cracks and it also allows a fast extraction of the signal. The principle of an electromagnetic calorimeter is that high energy electrons create bremsstrahlung inside the lead. This produces high energy photons. These photons then produce electrons and positrons by pair production. Both processes are repeated creating a shower of particles until the energy of the particles becomes low enough, so that the charged particles start ionizing the liquid argon. This creates a signal and because the signal strength is proportional to the energy of the particle, this energy can be read out. The sum of the energy of all shower particles is the energy of the original electron. However, it has to be remembered that not only electrons and photons deposit their energy in the electromagnetic calorimeter. But these other particles do not deposit their full energy in this calorimeter as they are not creating showers through bremsstrahlung and pair production. The electromagnetic calorimeter is divided several times. First there is a split between the barrel part that provides the coverage for $|\eta| < 1.475$ and the two end-components that provide coverage for $1.375 < |\eta| < 3.2$. The barrel part is further divided into two half barrels, which are separated by $4\,\text{mm}$ at z = 0. Each half barrel has a length of $3.2\,\text{m}$ and inner and outer diameters of $2.8\,\text{m}$ and $4\,\text{m}$ while weighing $57\,\text{t}$. The end-cap region is also divided into two coaxial wheels, where the inner wheel covers the region $1.375 < |\eta| < 2.5$ and the outer wheel the region $2.5 < |\eta| < 3.2$. Also the calorimeter is segmented in depth into three sections for the region $|\eta| < 2.5$ while the outer wheel is segmented into two sections. Furthermore, the outer wheel has a lower granularity than the rest of the calorimeter. [49, 51]

The hadronic calorimeter is used for measuring the energy of hadrons. The principle of this calorimeter is similar to the one of the electromagnetic calorimeter. In this case hadronic showers are created through the interaction of the hadron with the nuclei of the material until the energy of the single particle is low enough. The energy deposition is done via ionisation creating a signal that can be read out. However, the hadronic shower differs from the electromagnetic shower. While only electrons and photons are created in the electromagnetic calorimeter, all sorts of hadrons can be created in the hadronic calorimeter. This is a problem for the measurement of the energy as some of the created particles can be neutral. This means that they do not ionise the material. The hadronic calorimeter from ATLAS is divided into three parts. The first one is the tile calorimeter which covers the region of $|\eta| < 1.7$. It uses steel as absorber material and scintillating tiles as active material. The scintillator measures the intensity of the produced light and gets the energy of the hadron from this information. The second part of the calorimeter is the Hadronic End-cap calorimeter and it covers the region of $1.5 < |\eta| < 3.2$. This calorimeter uses copper as the absorbing material and liquid argon as the active material. The last part is the Forward Calorimeter which covers the region closest to the beam pipe of $3.1 < |\eta| < 4.9$. This part consists of three modules, where the first one uses copper and the other two tungsten as absorbing material. The active material is liquid argon in all modules. [49, 52]
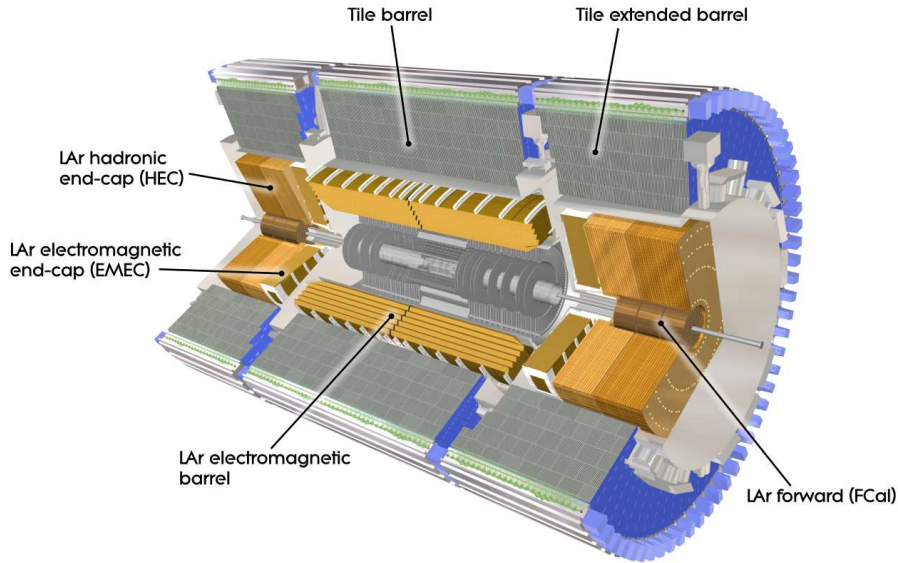
Figure 3.4: The Calorimeter System of the ATLAS detector [49]

3.2.4 Muon Spectrometer

The outmost part of the ATLAS detector is the Muon Spectrometer, shown in figure 3.5. In contrast to the other particles muons have a low cross-section and therefore do not interact with most matter. This also means, that muons fly through most of the detector without interaction. Therefore, the Muon spectrometer was installed in the ATLAS detector being a tracking system solely for muons. The spectrometer consists of four different modules: the Monitored Drift Tube Chambers (MDT), the Cathode Strip Chambers (CSC), the Resistive Plate Chambers (RPC) and the Thin Gap Chambers (TGC). The MDT and CSC are used for precise measurements of the muon track. These parts can also be used to measure the momentum of the muon as there are toroid magnets creating a magnetic field. Through the magnetic field the muon tracks are bent and depending on the radius, the momentum of the muon can be measured very precisely. The bending of the muon is done by the large barrel toroid over the region of $|\eta| < 1.4$. Over the region $1.6 < |\eta| < 2.7$ the bending is done by two end-cap magnets while the region $1.4 < |\eta| < 1.6$ is referred to as the transition region, where the magnetic field is provided by a combination of both magnets. The RPC and TGC are part of the trigger system, which is shown in section 3.2.5. Because of the large amount of events, it is impossible for the system to write out every event. Therefore, a trigger system is installed which decides if an event is written out or not. The trigger system is a less precise measurement of the event and depending on the results of the identity or momentum of the found particles, the data is deleted or written out. The RPC and TGC are the part of the system that can provide bunch-crossing identification, p_T thresholds and muon coordinates. [49]

3.2.5 The Trigger System

At the LHC protons collide with a rate of 40 MHz. With an event size of about 1.3 MB this leads to a required bandwidth of around 50 TB/s [53], which is not achievable by the ATLAS detector.
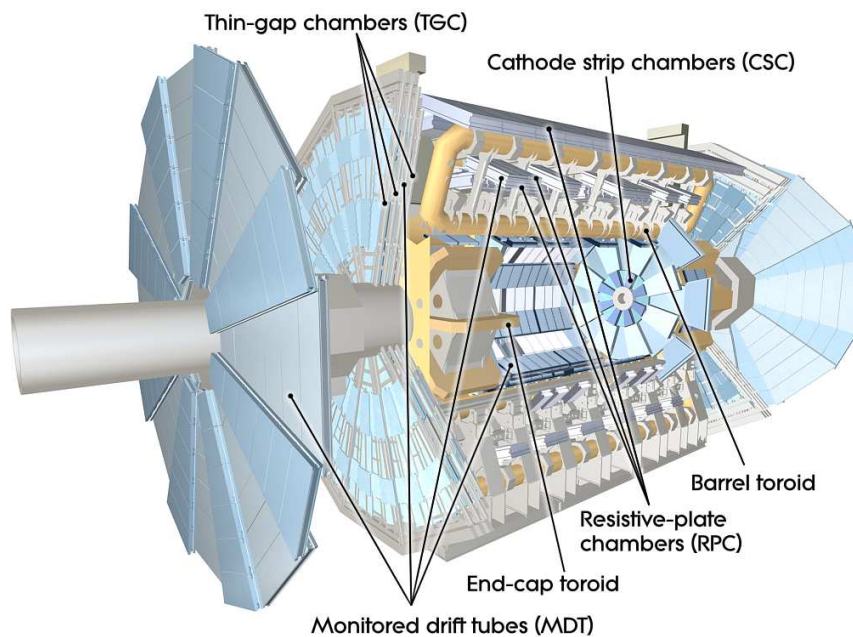
Figure 3.5: The muon system of the ATLAS detector [49]

Therefore, a two level trigger system is installed in the ATLAS detector, shown in figure 3.6. These trigger preselect events based on different observables from fast detector components. The Level-1 trigger is a hardware trigger that reduces the rate of events from 40 MHz to 100 kHz. It consists of the L1 calorimeter system (L1Calo), the L1 muon trigger system (L1Muon), the L1 topological trigger modules (L1Topo) and the Central Trigger Processors (CTP). The L1Calo trigger uses deposited information from the electromagnetic and hadronic calorimeter to select events with a high transverse energy E_T. This trigger was updated for Run-2, so that high L1 rates produced by missing transverse energy through pile-up, were reduced. The L1Muon trigger was already introduced in the previous section. It consists of the RPC and TGC and it preselects events based on a p_T threshold for muons. For Run-2 this trigger has been improved by reducing fake muon rates that were produced by charged low-p_T particles away from the central interaction point. Furthermore, there are additional muon chambers installed in the barrel region to increase the acceptance of L1 muons. The L1Topo trigger was added for Run-2 and it preselects events by calculating topological quantities between different L1 objects. This includes angular separation between L1 objects, invariant mass reconstruction of L1 pairs and global quantities like the missing transverse energy E_T^{miss}. The information from all these triggers is then sent to the CTP that decides if an event is triggered. Such an event is then forwarded to the L2 trigger, the High Level Trigger (HLT). [41,54]

In comparison to the L1 trigger system, the HLT is a software based trigger. After receiving the information from the L1 trigger the HLT uses the full detector information to preselect events even further to a rate of around 1 kHz. Afterwards, the events are stored in the storage system of the detector. The preselection of the HLT can be optimized to look for certain physical objects in an event. However, due to the limited bandwidth rate, it can happen that the trigger rate of the HLT is too high for the system to handle. In this case, not every event is written to the storage. Therefore, a prescale factor is calculated for each of the HLT, that can be later used to recalculate the real number
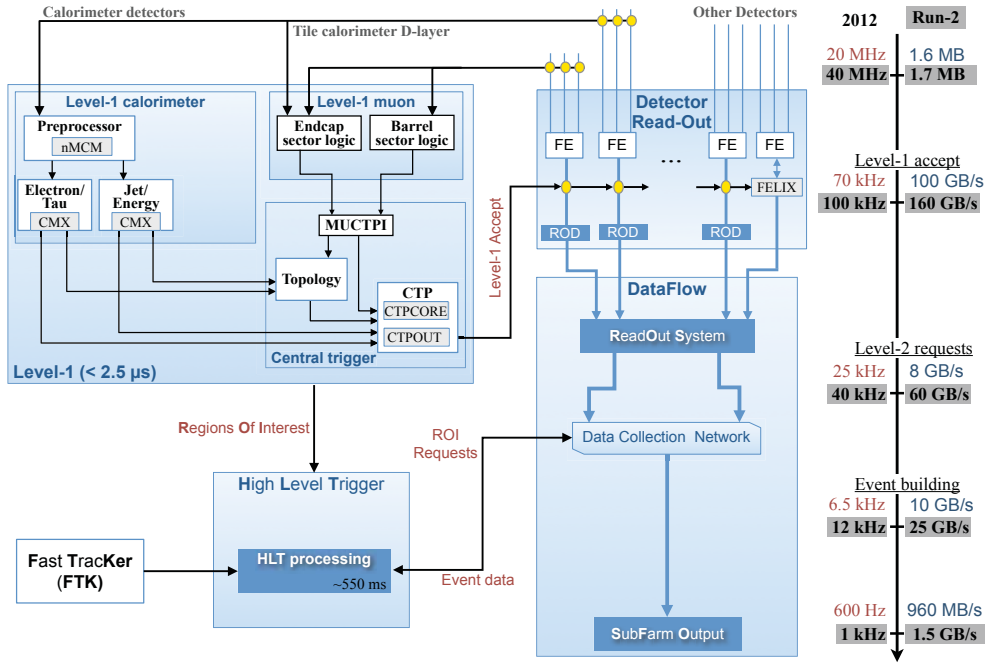
Figure 3.6: Overview of the ATLAS trigger system for Run-2 [54]

of events. [41]

4 Analysis

4.1 Process

The definition of an analysis is always dependent on the theory it is based on. Therefore, the motivation for this analysis is shortly repeated in the beginning of this section. It was shown in section 2.2.1 that the measured value of the anomalous magnetic moment of the muon deviates from the expected value in the SM. Because of that, a new model is needed that goes beyond the SM and that can explain this deviation. This model is the 2HDM. However, as it was seen in section 2.2.3 certain requirements in this model are needed so that the contributions of the 2HDM are high enough to explain the deviation. The first requirement is that the mass of the CP-odd Higgs boson A must be small. The second requirement is that the coupling parameter to leptons and up-type quarks needs to be high. The coupling to down-type quarks is not important during this analysis as it does not contribute much to the value of the anomalous magnetic moment of the muon. So it can be assumed that it is small in comparison to the other couplings.

A sign of evidence for this particular theory can be the existence of a particle predicted by it. Most theories, even those that are part of the 2HDM, do not predict a light CP-odd Higgs boson. The best way to search for evidence of this particular theory is therefore by searching for a light CP-odd Higgs boson A. The next step of the analysis is to determine how this particle could be created in the LHC and how it can be detected by the ATLAS detector.

In the LHC two protons collide, which means that the main interaction is between gluons and quarks. It was assumed that the coupling to up-type quarks is high. So the A boson should be produced by two up-type quarks. One way could be that two up-type quarks from the protons interact with each other to produce a CP-odd Higgs boson. However, the masses of the quarks making up a proton are small and therefore the cross-section for them to create a Higgs boson is low. A higher cross-section is achieved by a process called gluon fusion. In this process two gluons can produce a Higgs boson by interacting through a quark loop. The quark in this loop can theoretically be any quark. But because of the high top-quark mass, the highest cross-section for an A boson can be achieved through a loop with top-quarks.

After the production process the A boson needs to be detected. But as most particles, it decays before it can reach the detector. In theory the CP-odd Higgs boson can decay in different ways. But because the coulings to leptons were set to a high value, it can be assumed that the boson will decay into a pair of leptons in most cases. Furthermore, the decay into a pair of τ leptons is more likely, because of the higher τ mass. The branching ratio for the process $A \to \tau\tau$ is nearly 100% in this theory [32]. The whole production and decay process is shown in figure 4.1.

However, this figure does not describe the final state of the process. Because τ leptons themselves decay before reaching the detector only stable decay products of the τ leptons can be measured. τ leptons decay into a $W^{\pm}$ boson and a τ neutrino. The $W^{\pm}$ boson can then decay into either a pair of
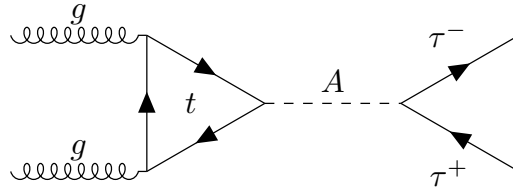
Figure 4.1: Production and decay of the CP-odd Higgs boson

quarks or into a lepton (electron or muon) and its corresponding lepton neutrino, shown in figure 4.2. If a τ lepton decays into two quarks, this is called the hadronic channel and if it decays into a lepton, it is called the leptonic channel. The branching ratio for the hadronic decay is approximately 65% and the probability for the leptonic channel 35% [55]. This analysis will only focus on the leptonic decay channel. While the branching ratio is lower, the analysis of hadronic decaying τ leptons has higher uncertainties and backgrounds. The reason for this is that quarks will not stay isolated as it was explained in section 2.1.1. This means that a hadronic decaying τ lepton can only be measured through its corresponding jet. Furthermore, the p_T threshold of the triggers are higher for hadronically decaying τ leptons. Electrons and muons on the other hand can be very easily identified and the energy and momentum can be measured very precisely in the ATLAS detector. But there is also a problem with the fully leptonic decay channel. In the process there are two τ leptons from the A boson decay. This means that the branching ratio of the process is only 12%, because both τ leptons decay leptonically with a probability of 35%. On top of that, the possible background through other processes has to be considered. A process with a high cross-section and two leptons in the final state is the Z decay $Z \to ll$. However, in this case both leptons need to have the same flavour. Therefore, this background can be reduced by only analysing events where one τ decays into an electron and the other into a muon. This leads to a branching ratio of about 6%. With that the definition of the process is finished and can be seen in figure 4.3. This means the final state of this process contains one electron, one muon and a total of four neutrinos.
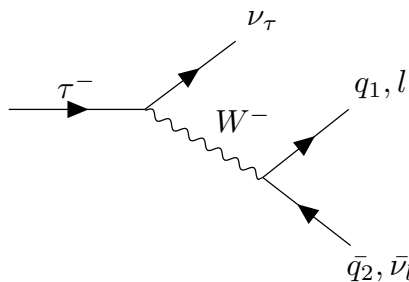
Figure 4.2: Possible decay channels of the τ lepton
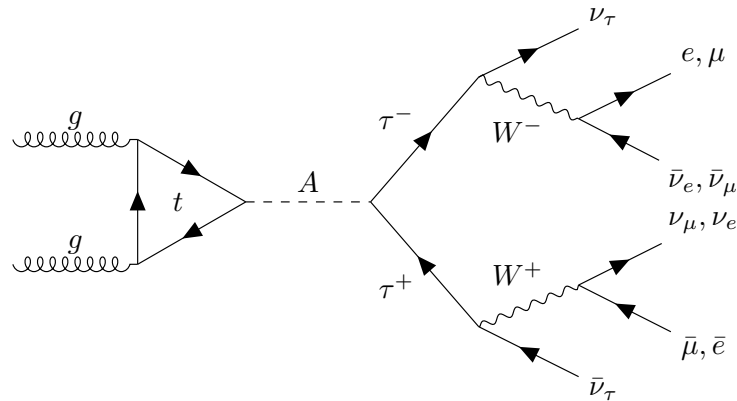
Figure 4.3: Full production and decay process of the analysis

4.2 Monte Carlo Samples

4.2.1 Motivation

In the previous section it was shown how the A boson can be found with data of the LHC through its production and decay process. However, it is not possible to take all the events containing one electron, one muon and neutrinos - shown through the missing transverse momentum - and then suppose that these are the results of an A boson decay. When colliding two protons, it can not be regulated what particles are produced. Only their final state can be measured. But some other produced particles have a similar or even nearly identical final state compared to the one of the A boson. Therefore, a certain number of events with this final state must be expected to be background. Background processes are usually described in the SM and the number of events produced by these processes can be predicted through calculation within the SM. The idea of the analysis is to take the data from the LHC, apply certain selection criteria, compare it to the SM prediction and then analyse if there is a significant deviation between them.

The problem is that the prediction of a process always includes different probabilities. This means that every collision of two protons is a process of chance. Only a probability for the identities of the produced particles can be predicted by using probability density functions (PDF). The same applies to the properties of the produced particles. For example the process $Z \rightarrow ee$ can include a Z boson with or without a momentum of itself. This leads to different properties of its decay products. This means that an observable of a $Z \rightarrow ee$ process can have different values in two events. To create this kind of unpredictability Monte Carlo simulations are used in this analysis for the signal and the background processes, which will be shown and discussed in section 4.3. During a Monte Carlo simulation several thousand events of a certain process are generated. But the exact outcome of each event is random, based on the probabilities that the event generator was given. Each event contains the information on what particles were created, which particles they decayed into and what the different properties of each particle are. The produced events can then be analysed like data from the LHC to analyse the shape of the distribution after the same cuts were applied. But the Monte Carlo simulation (MC) still differs in two aspects from real data. First, the simulation has to be modified so that effects from the real experiment are taken into account. On the one hand this means, that the properties of the particles have to be corrected to account for detector effects that can influence the measured

data. On the other hand, background processes have to be added to the simulated process. During a proton-proton collision different processes happen at the same time, because every proton consists of more than one particle. The main process is referred to as the hard scattering process, which is the process with the highest momentum transfer. But there are also a lot of underlying processes that can produce particles that are measured in the detector or that can just influence the interesting particles. [56]

Second, MC generators generate samples corresponding to a specific luminosity. This means that the samples have to be scaled to match the luminosity measured with the detector. Therefore, every MC event has to be weighted with its cross-section and the integrated luminosity of the data. In this analysis the integrated luminosity is $36.1\,\mathrm{fb}^{-1}$ and the cross-section for the different MC samples can be found in the tables of appendix A. The other factors in the tables are the K-Factor and the filter efficiency. The K-Factor is a modification of the cross-section for higher orders of the process. The filter efficiency is a factor originating from the MC event generator for filtering events that do not comply with given requirements. Sometimes, these factors are already included in the cross-section. Of course the branching ratio of the different processes is also important. This value is most of time included in the cross-section value as well. This means, that the cross-section in the tables of appendix A is the product of the cross-section and the branching ratio in most cases. But sometimes the branching ratio can also be included in the filter efficiency value, i. e. in the $t\bar{t}$ samples.

During this analysis only MC samples with the "HIGG4D1" derivation are used. To reduce computing time, an analysis does not run over the full MC and data sets, but only over a preselected subset. This subset is chosen depending on the analysed process. The "HIGG4D1" derivation includes at least two leptons with certain properties in the final state. The first lepton needs to have a transverse momentum of at least $13\,\mathrm{GeV}$ and the second of at least $13\,\mathrm{GeV}$ if it is an electron or $9\,\mathrm{GeV}$ if it is a muon. Furthermore, if the first or second lepton[1] is an electron it has to match loose identification criteria. Electrons are identified by different criteria, which are called loose, medium and tight. The tighter the identification, the more background is rejected. But that also means that the signal efficiency is lowered [57]. Also every muon is only allowed to have an absolute η value of maximum 2.5.

4.2.2 Signal cross-section

In the tables of the appendix A the MC samples and their cross-sections are shown for all background processes. For these processes the cross-section and all other parameters were already known. But for the signal samples these values have to be calculated from the new model presented in section 2.2. The cross-section for the production of an A boson is similar to the cross-section of a Standard Model Higgs boson of the same mass. But the cross-section has to be weighted in dependence on the coupling to up-type quarks, shown in figure 4.4. The cross-sections of a Standard Model Higgs boson for different masses and orders were calculated with a program called "ggHiggs" [58] at version 3.5. The results can be found in table 4.1. For the analysis the $\mathrm{N}^3\mathrm{LO}$ cross-section is used and because the branching ratio of the process $A \rightarrow \tau\tau$ is approximately 100% this is also directly the value for the cross-section multiplied with the branching ratio. Furthermore, it has to be taken into account, that

---

[1] Leptons are usually ordered by their transverse momentum, so the first leptons is always referred to the lepton with the highest transverse momentum in this analysis.

$\frac{\sigma_{tot}\ (\text{gg}\rightarrow\text{A})}{\sigma_{tot}\ (\text{gg}\rightarrow\text{h})}$						
$\xi_u \backslash M_A$,GeV	40	50	60	70	80	90
−0.5	0.724709	0.73016	0.71214	0.692202	0.675268	0.66192
−0.4	0.479624	0.479331	0.465009	0.450292	0.43806	0.428496
−0.3	0.28573	0.281465	0.270539	0.2603	0.252045	0.245669
0.3	0.197376	0.206493	0.209603	0.21063	0.211	0.211232
0.4	0.361818	0.379368	0.383761	0.384066	0.383334	0.382581
0.5	0.577452	0.605206	0.61058	0.60942	0.60686	0.604526

Figure 4.4: Ratio of the cross-section for a CP-odd Higgs boson to the cross-section of a Standard Model Higgs boson depending on the mass and coupling to up-type quarks for $\zeta_d = -0.3$, calculated by Vladimir Khasianevich and Dominik Stöckinger from [32]

Mass [GeV]	XSec [pb]			
	LO	NLO	NNLO	N^{3}LO
60	43.897	109.278	151.238	166.827
70	35.0192	85.44	117.398	129.316
80	28.5669	68.6164	93.6927	103.082
90	23.7323	56.2314	76.4134	83.9884

Table 4.1: Cross-section for a Standard Model Higgs boson with different mass and orders, calculated with ggHiggs [58]

the τ leptons in these samples are only allowed to decay into either an electron or muon. Because the branching ratio of $\tau^- \rightarrow e^- \bar{\nu}_e \nu_\tau$ is 17.83% and the branching ratio of $\tau^- \rightarrow \mu^- \bar{\nu}_\mu \nu_\tau$ is 17.41% [59] the probability for a leptonic decaying τ is 35.24%. If two τ leptons have to decay leptonically this process has a probability of 12.42%. This is included as filter efficiency in the calculations. Because the higher order calculations are already included in the cross-section, the K-Factor for all samples is set to 1.0. The samples for the signal are listed in the appendix A.11.

4.3 Background

As it was explained before, only the probability of the produced particles in the proton-proton collision can be predicted. Furthermore, a lot of SM processes have a higher cross-section and therefore a higher production rate than the signal process. The task of the analysis is to understand the final state of the signal process and to only select the events that meet certain requirements. These requirements are called cuts. The cuts should be chosen in a way that most of the signal process is preserved, but most of the background processes are sorted out. The cuts that are used for this can be found in section 4.4. However, to be able to set these cuts most effectively, the background processes have to be analysed first. Therefore, in the following sections the most important backgrounds are listed and compared to the signal process.

4.3.1 $Z \rightarrow \tau\tau$

The process $Z \rightarrow \tau\tau$ is one of the most problematic backgrounds of this analysis, because the Z boson decays into a pair of τ leptons as can be seen in figure 4.5. The τ leptons can decay into the same final state as the signal final state, which makes it difficult to distinguish the signal from the background.
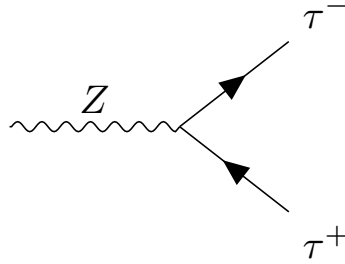
Figure 4.5: The background process $Z \to \tau\tau$

Differences between the two bosons can only result from the different masses. Unfortunately, the total mass can not be compared, because there are neutrinos in the final state. But there are other ways to compare the masses. The first mass observable is the invariant mass of the lepton system. This is the mass calculated only from the two leptons without the neutrinos through the equation

$$m^2 = p^\mu p_\mu = ((p_{l1} + p_{l2})^\mu)^2 \tag{4.1}$$

with p_{l1} and p_{l2} being the four-momenta of both leptons. Another possible mass observable is the total transverse mass. This mass is calculated from the transverse fraction of the leptons together with the missing transverse momentum, which is equal to the missing transverse energy in the assumption that it is only made of neutrinos. The last option used in this analysis is the missing mass calculator [60]. Here the additional knowledge of τ decay kinematics is used to create probability density functions of the possible solutions to find a better estimator for the mass of the di-τ system.

Another difference between the two processes is that the Z boson is a CP-even particle with a total angular momentum of 1 while the A boson is a CP-odd particle with a total angular momentum of 0. Both, the CP value as well as the total angular momentum can lead to differences in certain observables, specifically the angle between the decay planes of the τ leptons. Figure 4.6 shows two particles with the total angular momentum of 0 decaying into a pair of τ leptons. On the left side, the mother particle has a spin of 1. This results in the spin of the two τ particles being parallel to each other. Because of the fact, that neutrinos are always left-handed and anti-neutrinos always
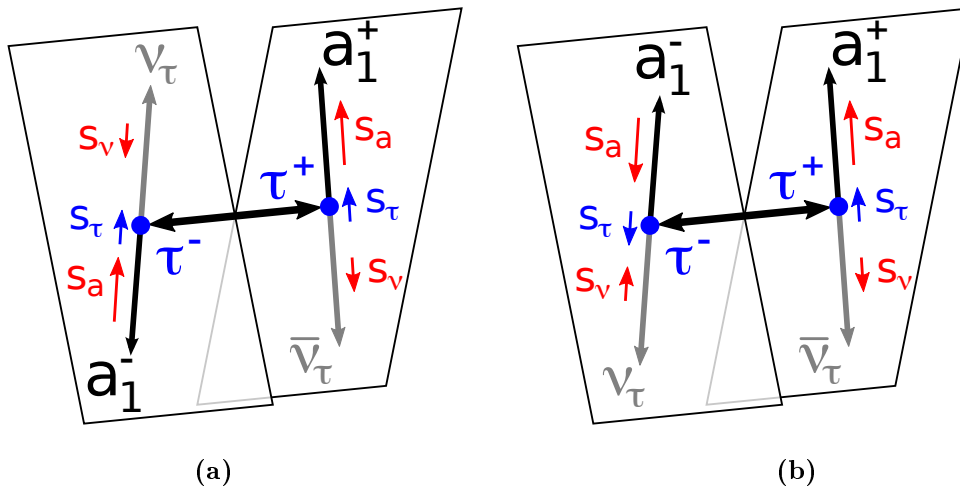
Figure 4.6: Decay planes of the τ leptons for (a) a scalar boson (b) a pseudoscalar boson [61]

right-handed, the spin orientation of neutrinos has to be anti-parallel to their momentum, while the spin orientation of anti-neutrinos must be parallel to their momentum. The angle between the decay planes measured through the visible decay products, is then approximately π. Because the total angular momentum of the mother particle is 0 and the spin is 1, the angular momentum has to be 1 as well. Equations (2.39) and (2.41) then lead to the result, that the particle has a positive parity and charge conjugation eigenvalue, what makes it CP-even and therefore a scalar boson. On the right side, the spin of the mother particle is 0, which leads to a small angle between the decay planes measured through the visible decay products. Because the total angular momentum is again 0, the angular momentum must be 0 as well. This leads to a negative parity and a positive charge conjugation eigenvalue making it CP-odd and a pseudoscalar boson. As the Z boson has a total angular momentum of 1, its angle between the decay planes looks different from the two presented here [30]. The different distributions of the angle between the decay planes are shown in figure 4.7. The decay planes for this figure were created from the properties of the leptons and their corresponding neutrinos on the truth level of the MC samples[2]. However, there is one problem when analysing this observable for the signal process of this thesis. The products a$^-$ and a$^+$ are not completely visible in this thesis, because they include a second neutrino originating from the W decay. This means that the reconstruction of the decay planes through the visible decay products [61] is not precise enough to use this observable during the analysis. But it can be used in a future analysis, where the τ leptons decay hadronically.

4.3.2 $Z \to ll$

A similar process to $Z \to \tau\tau$ is the decay of the Z boson into a pair of leptons, shown in figure 4.8. While this process has a higher branching ratio it is not as problematic for the signal, because there are two differences. First, an electron or muon does not decay before reaching the detector. This means that the final state only consists of two leptons without any neutrinos. Therefore, the missing transverse energy of this process should be lower than the missing transverse energy in the signal process. But the most important difference is that the Z boson can only decay into a pair of leptons from the same generation. So it decays either into a pair of electrons or a pair of muons. In comparison the signal process includes exactly one electron and one muon. So this background process is strongly suppressed through the definition of the signal process. A complete rejection of the process is not possible, because sometimes muons, electrons or jets can get misidentified.

4.3.3 $t\bar{t}$ and Single Top

These two processes are usually combined into one Top background category. Both backgrounds feature the top-quark in their processes, which decays in more than 90% of the cases into a b-quark and a W boson [62]. The W boson can then decay into a lepton-neutrino pair. This decay is presented in figure 4.9. With two top-quarks decaying in the $t\bar{t}$ background this process can be very similar to the signal process. The single top decay on the other hand differs a lot more from the signal process as it can only produce a maximum of one lepton through its decay. However, it is again possible that a jet is misidentified, i. e. as an electron, resulting in an event with supposedly two leptons.

---

[2]When analysing MC samples on the truth level, the properties of every particle are known. This also applies to particles that can not be measured by the detector like neutrinos.

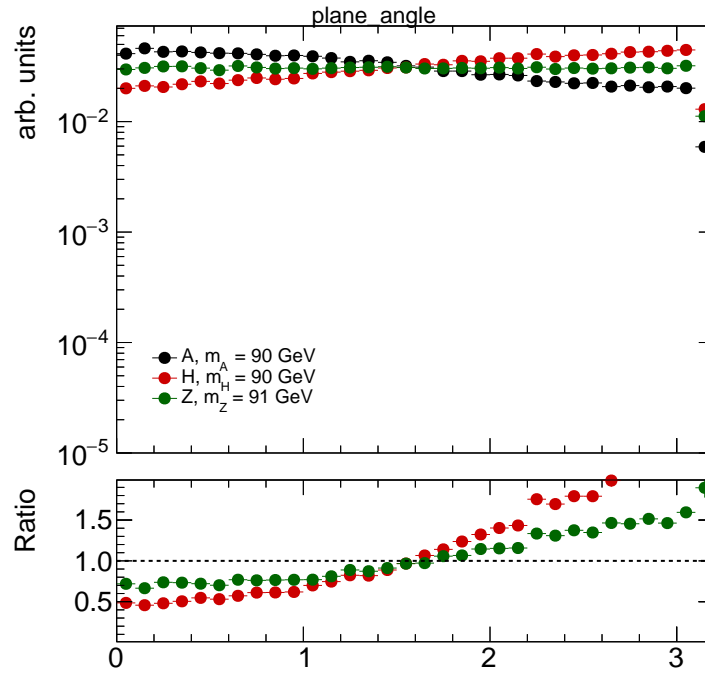**Figure 4.7:** The angle ϕ between the decay planes of the τ leptons for a CP-even Higgs boson H, a CP-odd Higgs boson A and a Z boson
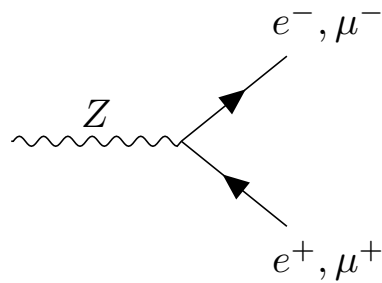

Figure 4.8: The Background process $Z \to ll$
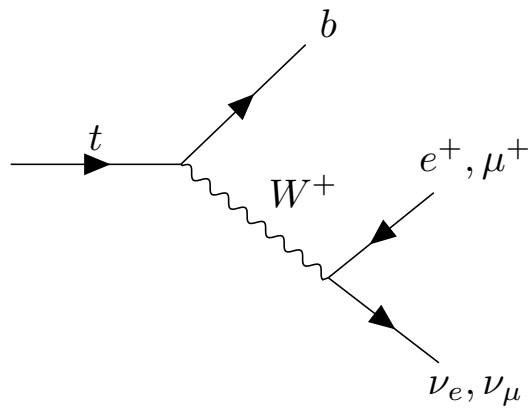
Figure 4.9: The leptonic decay of a top-quark

The first difference between the top and the signal process is that there are at least two neutrinos less in the background process than the signal process. This should result in a smaller missing transverse energy. But this is not very precise, because the missing transverse energy is not the sum of the neutrino energies. For example, if two neutrinos are created back to back, the momentum adds up to zero resulting in a missing transverse energy of zero. Fortunately, there is another difference. As mentioned before, most top quarks decay into a bottom quark which hadronises to a b-jet. Therefore, if all events containing a b-jet are sorted out, the number of top background processes can be minimised. It has to be kept in mind, that the algorithm for tagging b-jets has an efficiency of 70%. This means that in this analysis, events with a b-jet are rejected with 70% efficiency. Therefore, it is not possible to suppress the whole top-quark background with this method. Furthermore, this selection will also sort out some of the signal events as it is possible that a b-jet is created in an underlying process or a particle from a leptonic τ decay is misidentified as a b-jet.

4.3.4 $H_{125} \rightarrow \tau\tau$

This process is the SM equivalent to the signal process. Like the $Z \rightarrow \tau\tau$ background its final state is identical to the signal process. But in comparison to the Z decay, this process has a lower cross-section, so its contribution to the background is not as high as the $Z \rightarrow \tau\tau$ background. Like the $Z \rightarrow \tau\tau$ background this process can be primarily suppressed through a mass observable as the SM Higgs boson has a mass of 125 GeV while the CP-odd Higgs boson has a mass of less than 100 GeV. Like before, those mass observables can be the mass of the dilepton system, the total transverse mass or the mass calculated by the missing mass calculator. The other difference of this background to the signal process is the fact, that the SM Higgs boson is a CP-even boson while the signal process includes a CP-odd boson. This leads to a difference in the angle between the decay planes. This was already shown in the analysis of the $Z \rightarrow \tau\tau$ background. But as it was also explained, this observable is not precise enough to use in an analysis where the τ leptons decay leptonically.

4.3.5 $W \rightarrow \tau\nu_\tau$ and $W \rightarrow l\nu_l$

Like τ leptons, W bosons can decay in different ways. It can either decay hadronically into a pair of quarks or leptonically into a lepton and its corresponding neutrino. Since the hadronic decay channel does not include a lepton, its final state is very different from the signal final state and this process is thereby suppressed. In the leptonic decay channel, the W boson can decay into a τ lepton and its neutrino. The τ lepton then decays hadronically or leptonically. With the same motivation, only the leptonic decay channel is of interest, since the hadronic decay channel does not include any leptons and is thereby suppressed. The second decay of the leptonic decay channel of the W boson is the direct decay into an electron or muon and its corresponding neutrino. Both leptonic decay processes are presented in figure 4.10. Even though the leptonic decay processes are not suppressed as strongly as the hadronic decay channels, their final states include only one lepton. This differs from the signal final state containing two leptons. Therefore this process is also suppressed through the definition of the signal process. But like mentioned before, there will still be background from both processes since jets can be misidentified as leptons.
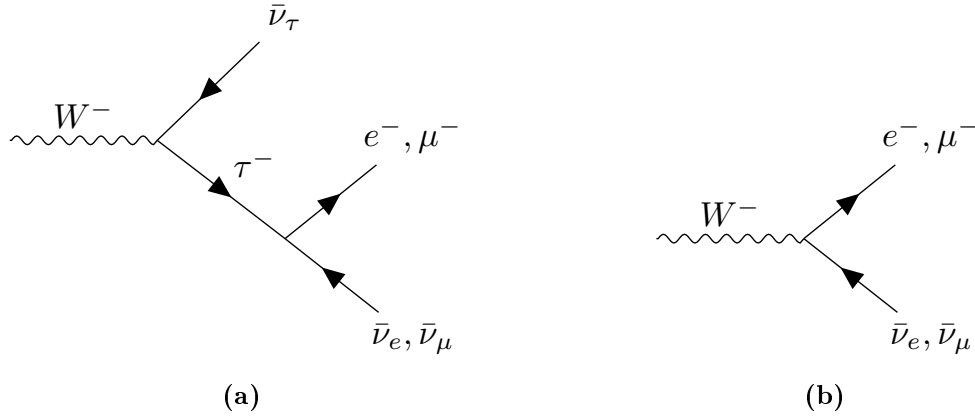
Figure 4.10: Leptonic decay processes of the W boson (a) $W \to \tau \nu_\tau$ (b) $W \to l \nu_l$

4.3.6 Diboson background

The diboson background is a continuation of the Z and W background. It contains two bosons, which can be any combination of W and Z bosons together with every possible decay for both bosons. This can lead to final states, that are not similar to the signal final state, i. e. if two Z bosons decay leptonically producing four leptons. But this can also lead to final states that are very similar to the signal final state, i. e. if two W bosons decay leptonically producing two leptons and two neutrinos. A difference for processes similar to the signal process can be the different mass observables that were already mentioned. Since two leptons can only originate from one Z boson, two Z bosons, two W bosons or a combination of a Z and a W boson, the reconstructed masses should be higher than the masses of the light CP-odd Higgs bosons in most cases.

4.3.7 QCD background

The QCD background describes all the processes that include some form of hadronically decaying particles. In most cases these include top-quarks, W bosons and τ lepton decays. All of these particles can either decay leptonically or hadronically producing QCD background. QCD background can also be produced through underlying events that are not part of the hard scattering process. These QCD events can be predicted by MC samples that can be found in the appendix A. Because two leptons are required in the final state, most of the aforementioned processes do not include a hadronic decaying particle as the possible candidates have to decay leptonically to result in a similar final state.

4.4 Event Selection

In this section the selection of the events is shown. Without an event selection the background contributions would be too high to find a possible signal from a CP-odd Higgs boson. Therefore cuts are applied to the events, so that only events remain with a high signal contribution. This is done by maximising the expected discovery significance for the different cuts. However, because the mass of the CP-odd Higgs boson is not known, four mass predictions are analysed. These include a CP-odd Higgs boson with a mass of 60 GeV, 70 GeV, 80 GeV and 90 GeV. Since their masses are different their distributions also differ from each other. First some general cuts will be defined that are applied for

all mass predictions. These cuts are called baseline cuts. Afterwards, cuts are chosen differently for every mass prediction, so that the significance is maximised.

4.4.1 Baseline Selection

In this section the baseline selection is presented. This selection consists of the same cuts for all the mass predictions. This section will explain why these cuts are used by explaining their influence on the signal and background processes. Cuts depending on the mass of the A boson will be presented later in section 4.4.2. First, the properties of the process itself are transformed into different cuts. As it was explained in section 4.1 the final state of the process will include two leptons and four neutrinos with the two leptons being exactly one electron and one muon. Because of that, the trigger for the analysis will be an electron-muon trigger. Different triggers have to be used for 2015 and 2016 data. These are shown in table 4.2. It can be seen, that the p_T of the electron and the muon has to be at least 7 GeV and 24 GeV. This means, that an event is only triggered if minimum one electron with a p_T of at least 7 GeV and one muon with a p_T of at least 24 GeV are found. However, to have high efficiencies for the triggers, the p_T of the triggered leptons have to be higher than the p_T threshold of the trigger. The p_T of the muon has to be 1.05 times higher than the trigger threshold and the p_T of the electron has to be 1 GeV higher than the trigger threshold [63,64]. Therefore, when counting the electrons and muons in an event, only electrons with a p_T of at least 8 GeV and only muons with a p_T of 25 GeV are considered. Additionally, the identification criteria for electrons and muons is set to medium. In addition to that, criteria on the isolation of electrons and muons are defined. The idea of the isolation criteria is that the sum of all transverse momenta in a defined cone around the lepton is not allowed to be too high in comparison to the transverse momentum of the lepton. The isolation working point used in this analysis for electrons and muons is set to "Gradient" [65,66]. Furthermore, in order to reduce Diboson background, especially ZZ and WZ background, only events are selected that have exactly one electron and one muon with the mentioned properties. This can also lead to the reduction of some signal events, as it is possible that a jet is misidentified as an electron or additional leptons are created in underlying processes. However, the reduction of the signal is not as strong as the suppression of the Diboson background. The last definition for the process is that the leptons need to have opposite charge, because the CP-odd boson is a neutral particle, which means that it can only decay into a τ lepton and an anti-τ lepton.

After choosing cuts that define the process, the remaining cuts are chosen to reduce the background. As it was explained in section 4.3 some of the processes are already suppressed through the definition of the process itself. These processes are the QCD, W, Diboson and $Z \to ll$ background. This means, that the processes that have to be considered when searching for additional cuts are $H_{125} \to \tau\tau$, $Z \to \tau\tau$ and $t\bar{t}$ with single top. It was shown in section 4.3 that the $H_{125} \to \tau\tau$ and $Z \to \tau\tau$

Trigger	Data Period	p_T
`HLT_e7_lhmedium_nod0_mu24`	2016	$p_T^\mu > 24$ GeV $p_T^e > 7$ GeV
`HLT_e7_lhmedium_mu24`	2015	$p_T^\mu > 24$ GeV $p_T^e > 7$ GeV

Table 4.2: Triggers used during the Event Selection

background are very similar to the signal process and can therefore only be suppressed through mass selections. But mass selections have to be dependent on the prediction, so these will be analysed in section 4.4.2. This leaves only the $t\bar{t}$ background to analyse. As it was shown in section 4.3.3 this process differs from the signal process through the production of b-jets in the final state. So this background can be suppressed by only selecting events, that do not contain a b-jet. For this the "BTaggingEfficiencyTool" [67] is used with an efficiency of 70%. However, because there are a lot of jets that are produced in underlying events, this could also suppress a lot of the signal events. To make sure, that the observed jets were produced in the hard scattering $t\bar{t}$ process, only jets are analysed that have a p_T of at least 20 GeV. Still, through jet production from gluons it is possible that some of the signal events will not be selected. And because the tool has an efficiency of 70%, it is also possible that some $t\bar{t}$ events will still be selected and contribute to the background.

4.4.2 Event selection for different mass predictions

After the baseline selection, the further cuts now have to be selected in dependence on the distribution of the different signal predictions. For this the distribution of the signal prediction against the background has to be analysed. Because the baseline selection did not reduce the $Z \to \tau\tau$ background significantly, this process becomes the most important background for the further analysis. As it was shown in section 4.3.1 this process primarily differs from the signal processes through the mass of the mother particle. Therefore cuts on mass distributions could reduce the background most effectively. However, the signal distributions are also dependent on the mass prediction of the A boson. This can be seen in figure 4.11, where the distributions of the total transverse mass, the dilepton mass and the mass calculated through the missing mass calculator are shown for an A boson with a mass of 60 GeV and 80 GeV. The mass distributions for an A boson with a mass of 70 GeV and 90 GeV can be found in appendix B.1. These figures show that the background can be heavily reduced by selecting events, where these mass observables are small, because the masses of the CP-odd Higgs bosons A are small. Because of the neutrinos in the final state the total mass can never be completely reconstructed. Therefore, the sensitivity can be mostly increased by defining cuts for all three mass distributions. The expected discovery significance is then used to determine the exact numbers for every mass selection. For example for a 60 GeV boson only events are selected where the total transverse mass $m_T^{tot} < 55$ GeV, the dilepton mass $m_{ll} < 40$ GeV and the mass calculated from the missing mass calculator $m_{MMC} < 65$ GeV. The cuts for the different signal processes can be found in table 4.3.

However, the mass alone is not the only observable that is different for the signal processes in comparison to the background. The second observable is a result of the low mass of the A boson combined with the high p_T lepton requirements from the trigger in the baseline selection. Because of the trigger an event always consists of a muon with a p_T of at least 25 GeV and an electron with a p_T of at least 8 GeV. Together this sums up to an energy of 33 GeV, which is already more than half the mass of a 60 GeV Higgs boson. In addition to that, there are four neutrinos in the final state, which also have a certain energy. Everything combined often leads to the rejection of events with an A boson at rest. While this is a problem, because the number of signal events is then reduced for light A bosons due to the baseline selection, this also creates a new difference between the signal and background processes. Because the A boson often has a transverse momentum in the selected events, the angle between

(a)

(b)

(c)

(d)

(e)

(f)
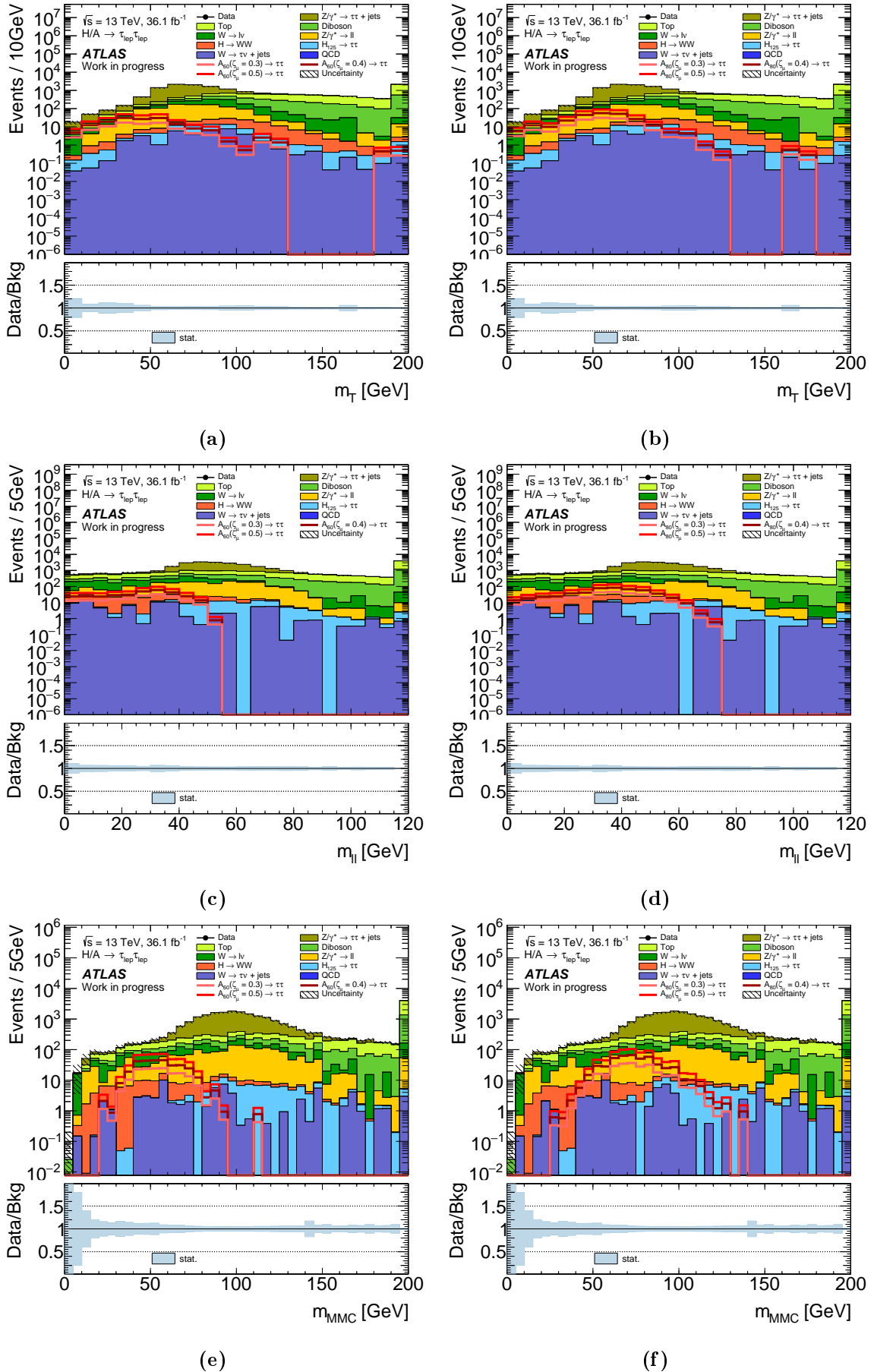
Figure 4.11: Mass distributions of the total transverse mass, the dilepton mass and the mass calculated through the missing mass calculator for an A boson with a mass of 60 GeV (left) and 80 GeV (right)

the daughter particles gets smaller. This is a result of the momentum conservation in the decay of boosted particles. This smaller angle then leads to a smaller angle between the visible leptons in the signal process compared to the background. This is shown in figure 4.12 where ΔR and $\Delta \eta$ between the two leptons are shown for a $60\,\mathrm{GeV}$ and an $80\,\mathrm{GeV}$ CP-odd Higgs boson. The distributions for a $70\,\mathrm{GeV}$ and a $90\,\mathrm{GeV}$ CP-odd Higgs boson can be found in the appendix B.2. It can be seen in figure 4.12a that there are less signal events with a high distance ΔR while the opposite is true for the background. However, figure 4.12b shows that the signal distribution for A bosons with higher masses is more similar to the background. For a $60\,\mathrm{GeV}$ Higgs boson the angular cuts can then be determined as $\Delta \eta_{ll} < 1.6$ and $\Delta R_{ll} < 2.3$. The cuts for the other signal processes can be found in table 4.3.

	$m_A = 60\,\mathrm{GeV}$	$m_A = 70\,\mathrm{GeV}$	$m_A = 80\,\mathrm{GeV}$	$m_A = 90\,\mathrm{GeV}$
Baseline Selection	\# of μ = \# of e = 1 and $q_\mu \cdot q_e = -1$			
	$p_T^\mu > 25\,\mathrm{GeV}$, $p_T^e > 8\,\mathrm{GeV}$			
	\# of b-jets = 0 with $p_T^{jet} > 20\,\mathrm{GeV}$			
Individual Event Selection	$m_T^{tot} < 55\,\mathrm{GeV}$	$m_T^{tot} < 65\,\mathrm{GeV}$	$m_T^{tot} < 75\,\mathrm{GeV}$	$m_T^{tot} < 85\,\mathrm{GeV}$
	$m_{ll} < 40\,\mathrm{GeV}$	$m_{ll} < 40\,\mathrm{GeV}$	$m_{ll} < 50\,\mathrm{GeV}$	$m_{ll} < 60\,\mathrm{GeV}$
	$m_{MMC} < 65\,\mathrm{GeV}$	$m_{MMC} < 75\,\mathrm{GeV}$	$m_{MMC} < 85\,\mathrm{GeV}$	$m_{MMC} < 100\,\mathrm{GeV}$
	$\Delta \eta_{ll} < 1.6$	$\Delta \eta_{ll} < 1.8$	$\Delta \eta_{ll} < 1.8$	$\Delta \eta_{ll} < 2.4$
	$\Delta R_{ll} < 2.3$	$\Delta R_{ll} < 3.1$	$\Delta R_{ll} < 3.0$	$\Delta R_{ll} < 3.1$

Table 4.3: Complete list of cuts for all different signal processes
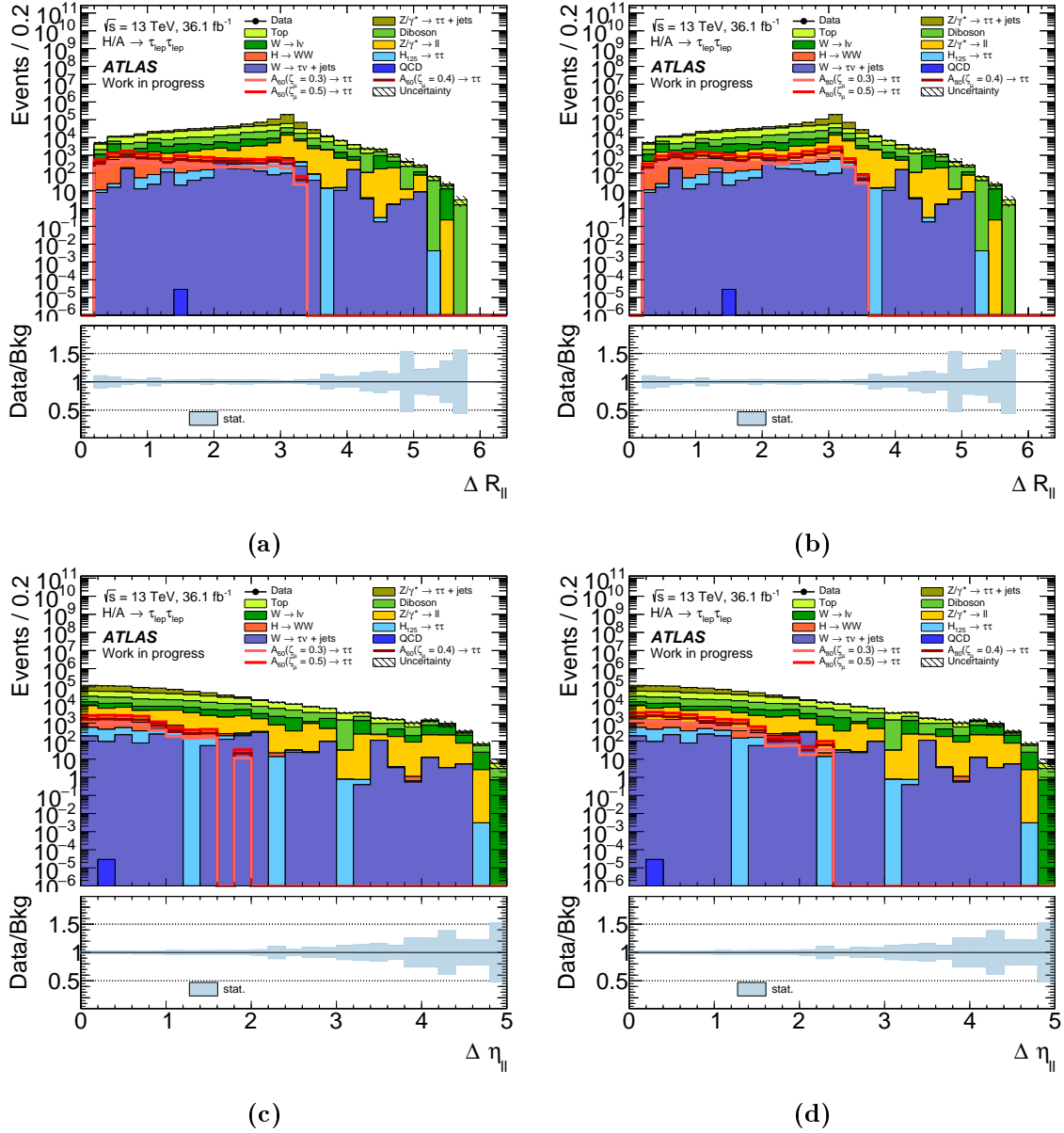
Figure 4.12: Distributions of ΔR and $\Delta \eta$ between the two leptons for an A boson with a mass of 60 GeV (left) and 80 GeV (right)

4.5 Background estimation

As it was explained in section 4.2, Monte Carlo samples are used to determine the background prediction for the analysis. However, to be able to create these large event numbers approximations for the particles, especially those from underlying events, have to be done. This can lead to a small deviation in different Monte Carlo predictions. These deviations are slightly dependent on the analysis and therefore have to be examined for every analysis. A way to find these deviations is by choosing control regions for the most dominant backgrounds. In these control regions only a few cuts are changed so that the background mostly consists of one process while minimising the signal contamination. Through the comparison of data and background a scaling factor for this process can be found to correct the Monte Carlo simulations.

4.5.1 $Z \to \tau\tau$ Control Region

As it was shown before, the most important background is the $Z \to \tau\tau$ process. This process primarily differs from the signal background through the mass of the mother particle. Therefore, the mass cuts for this control region are changed to cuts for a 91 GeV mother particle. This is done by setting the mass calculated through the missing mass calculator between 80 GeV and 100 GeV, while the other mass cuts are not implemented. This leads to a more dominant $Z \to \tau\tau$ background, shown in figure 4.13. The figure shows the p_T of the leading lepton and the mass from the missing mass calculator for the analysis of a 60 GeV Higgs Boson. Especially the histogram for the leading lepton displays that there are slightly more data than simulated background events. Because the background now mainly consists of $Z \to \tau\tau$ background, the reason for this deviation most likely lies in the prediction of this process. Therefore a scale factor of 1.026 is applied to all the $Z \to \tau\tau$ Monte Carlo samples, which leads to the new distributions shown in figure 4.14. As explained this is done for every analysis independently. The different scaling factors are shown in table 4.4 while the plots for these control regions can be found in the appendix B.3.

Mass	60 GeV	70 GeV	80 GeV	90 GeV
$Z \to \tau\tau$ scaling factor	1.026	1.073	1.078	1.068

Table 4.4: Scaling Factors of the $Z \to \tau\tau$ process for the different analyses

4.5.2 Top Control Region

The second important background consists of processes that either contain a top and anti-top quark or just a single (anti-)top quark. The top background was suppressed mostly by not allowing a b-jet in the event. Therefore, the selection for the control region includes at least one b-jet in the event. As shown in figure 4.15, this leads to a dominant top background. Because there are primarily top events as background, every deviation between background and data can be assumed to be caused by the top processes. Therefore, a scaling factor of 1.024 for the analysis of a Higgs boson with a mass of 60 GeV can be determined, which then leads to the distributions displayed in figure 4.16. As before, this scaling factor depends on the mass point specific cuts of the analysis. This means that the scaling factor has to be determined for every mass point analysis. This leads to the scaling factors that are shown in table 4.5 with the corresponding plots in the appendix B.4.

Figure 4.13: $Z \to \tau\tau$ control region plots for the analysis of a Higgs Boson with a mass of $60\,\mathrm{GeV}$ (a) p_T of the leading lepton (b) mass from the missing mass calculator

Figure 4.14: $Z \to \tau\tau$ control region plots for the analysis of a Higgs Boson with a mass of $60\,\mathrm{GeV}$ with a scale factor of 1.026 (a) p_T of the leading lepton (b) mass from the missing mass calculator

Figure 4.15: Top control region plots for the analysis of a Higgs Boson with a mass of 60 GeV (a) p_T of the leading lepton (b) Missing transverse energy

Figure 4.16: Top control region plots for the analysis of a Higgs Boson with a mass of 60 GeV and a scaling factor of 1.024 (a) p_T of the leading lepton (b) Missing transverse energy

Mass	60 GeV	70 GeV	80 GeV	90 GeV
Top scaling factor	1.024	1.025	1.032	1.088

Table 4.5: Scaling Factors of the top processes for the different analyses

4.5.3 $Z \to ll$ Control Region

The $Z \to ll$ background is not as dominant as the two that were discussed before. But due to the high cross-section for the Z production, the background is still important. Because the background was mostly suppressed by the fact that the final state had to contain exactly one electron and one muon, the control region for this process can be achieved by selecting events that either contain two electrons or two muons. But since events were triggered when exactly one muon and one electron were found, the triggers have to be changed. The new triggers for the ee and $\mu\mu$ channel are shown in table 4.6. Similar to section 4.4 the threshold for the p_T of the leptons has to be higher, because of

Trigger	Channel	Data Period	p_T
HLT_2e17_lhvloose_nod0	ee	2016	$p_T^{e_1} > 17\,\text{GeV}$ $p_T^{e_2} > 17\,\text{GeV}$
HLT_2e12_lhloose_L12EM10VH	ee	2015	$p_T^{e_1} > 12\,\text{GeV}$ $p_T^{e_2} > 12\,\text{GeV}$
HLT_2mu14	$\mu\mu$	2016	$p_T^{\mu_1} > 14\,\text{GeV}$ $p_t^{\mu_2} > 14\,\text{GeV}$
HLT_2mu10	$\mu\mu$	2015	$p_T^{\mu_1} > 10\,\text{GeV}$ $p_t^{\mu_2} > 10\,\text{GeV}$

Table 4.6: Triggers used in the $Z \to ll$ control region

the efficiency for the triggers. This means, that the electrons now need to have a p_T of at least 18 GeV and muons a p_T of at least 15 GeV. The rest of the cuts stays the same leading to the distributions in figure 4.17 where the $Z \to ll$ process is now the dominant process. As before a scaling factor can now be determined, because most of the background consists of the process $Z \to ll$. For the analysis of a 60 GeV Higgs boson a scaling factor of 1.145 was determined. The distributions with an applied scaling factor are shown in figure 4.18. Like before this is done for every mass point analysis, which leads to the scaling factors that can be found in table 4.7 together with the plots in appendix B.5.

Mass	60 GeV	70 GeV	80 GeV	90 GeV
$Z \to ll$ scaling factor	1.145	1.089	1.014	0.966

Table 4.7: Scaling Factors of the $Z \to ll$ process for the different analyses

4.5.4 W Control region

The last processes that have to be analysed are the W processes. Like the $Z \to ll$ process these are not dominant backgrounds. But due to their high cross-section they have to be analysed. This background was mostly suppressed by the definition that only events that contain exactly two leptons are selected, because a W boson can only decay into one lepton at maximum. Therefore, the control region of this process requires exactly one lepton which can either be an electron or a muon. But

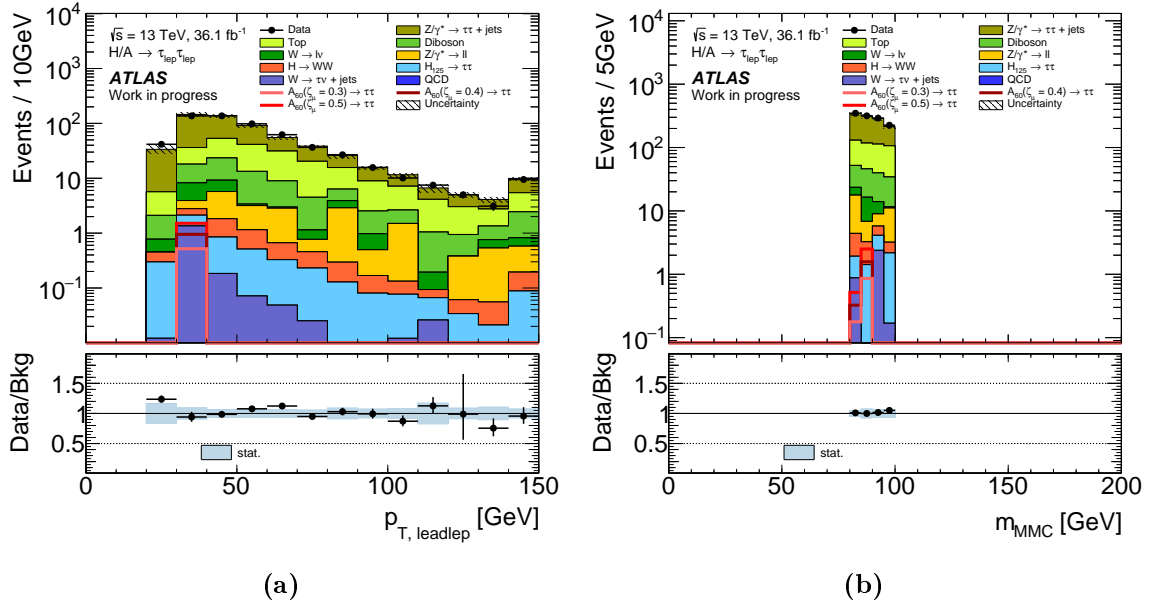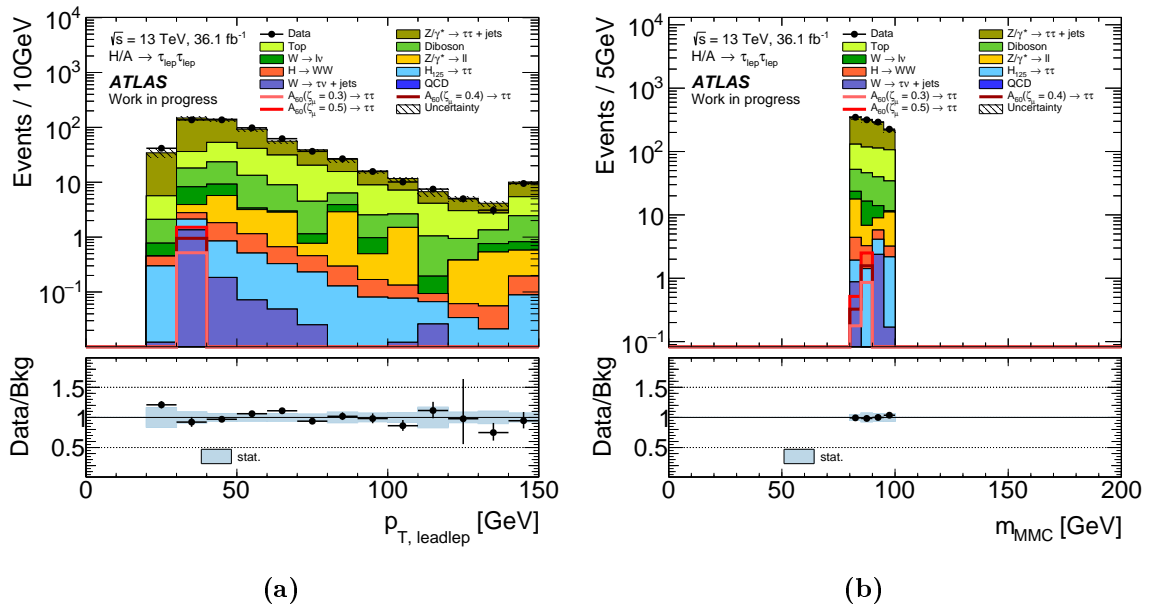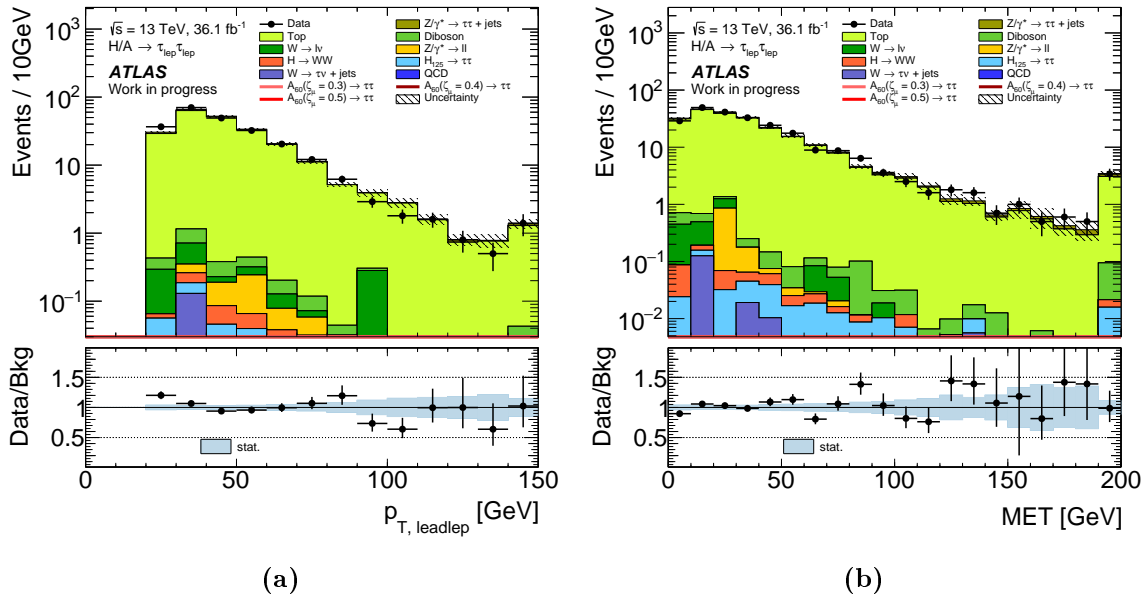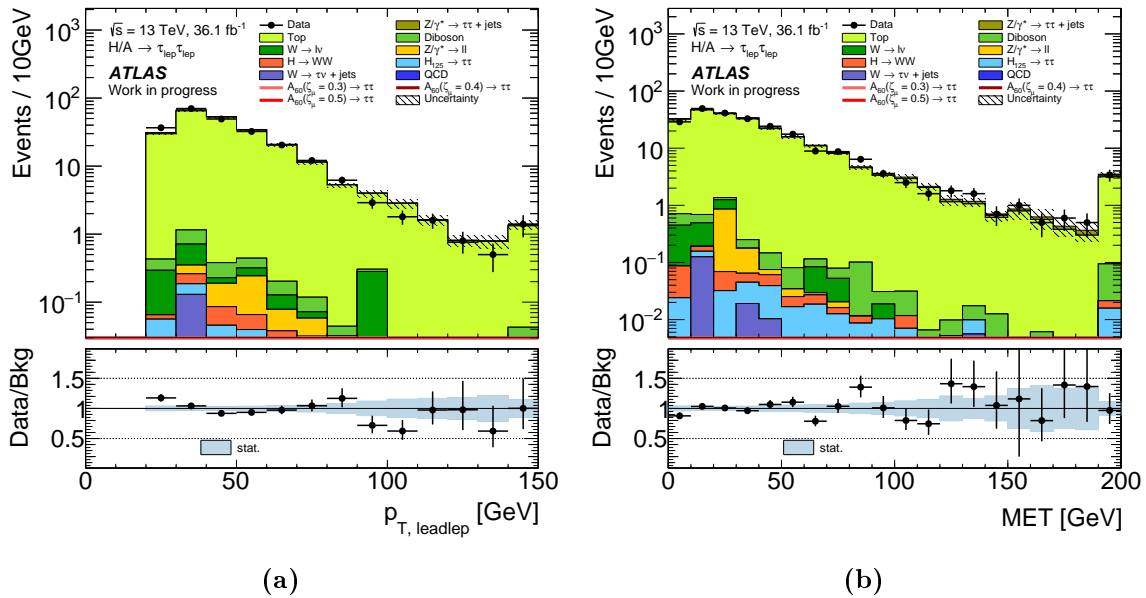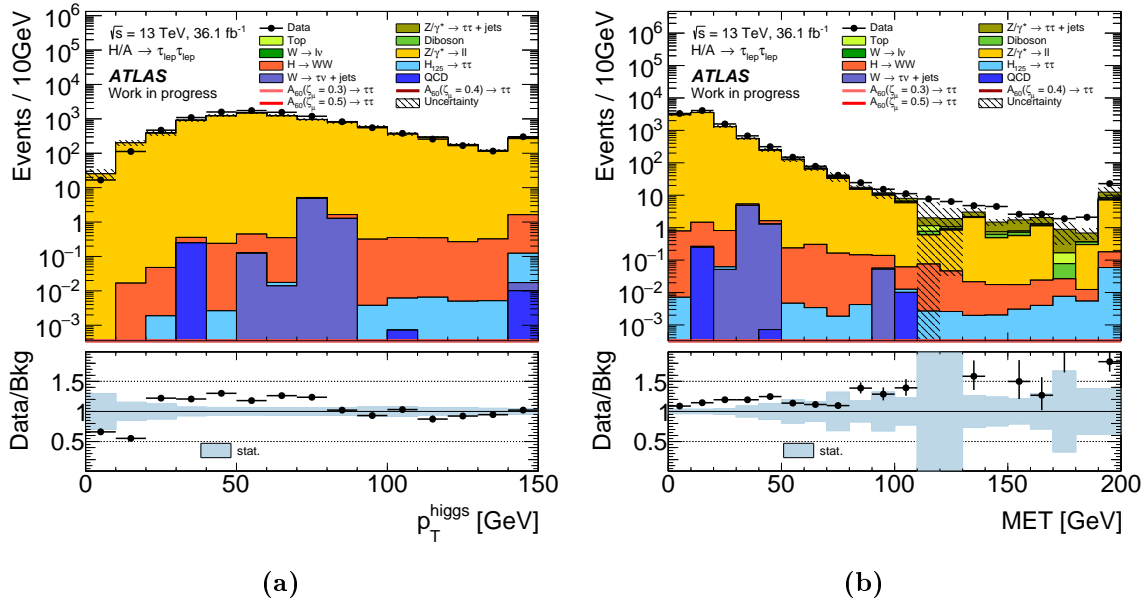**Figure 4.17:** $Z \to ll$ control region plots for the analysis of a Higgs Boson with a mass of 60 GeV (a) p_T of the mother particle (b) Missing transverse energy
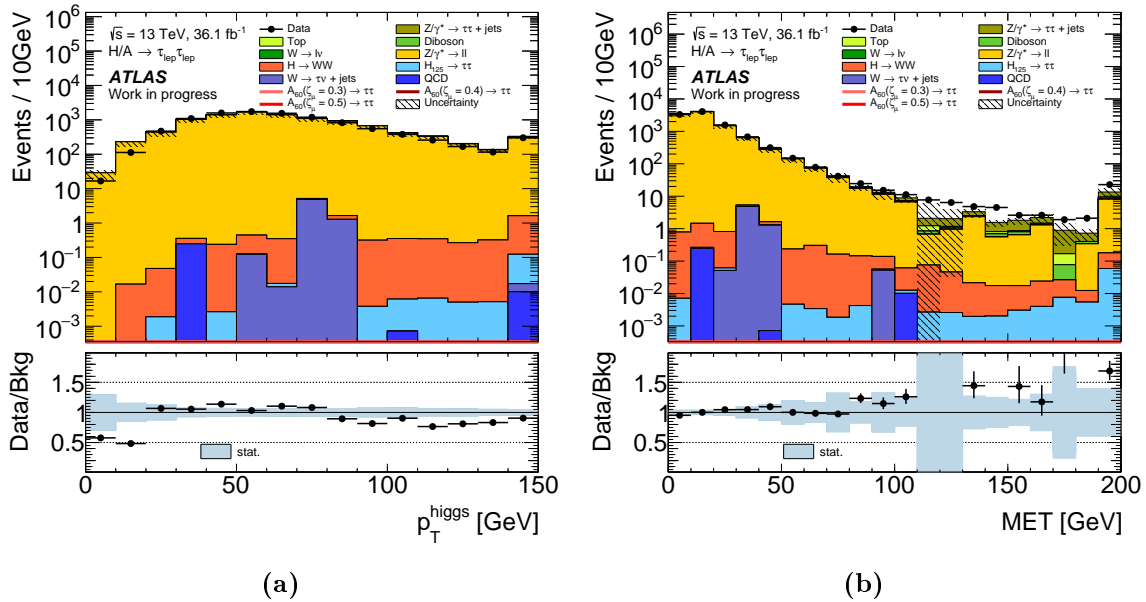

Figure 4.18: $Z \to ll$ control region plots for the analysis of a Higgs Boson with a mass of 60 GeV and a scaling factor of 1.145 (a) p_T of the mother particle (b) Missing transverse energy

similar to the $Z \rightarrow ll$ control region new triggers have to be applied that are shown in table 4.8. The new triggers result in new p_T thresholds for the lepton. A lepton now needs to have a p_T of

Trigger	Channel	Data Period	p_T
`HLT_e26_lhtight_nod0_ivarloose`	e	2016	$p_T^e > 26\,\text{GeV}$
`HLT_e24_lhmedium_L1EM20VH`	e	2015	$p_T^e > 24\,\text{GeV}$
`HLT_mu26_ivarmedium`	μ	2016	$p_T^\mu > 26\,\text{GeV}$
`HLT_mu26_imedium`	μ	2015	$p_T^\mu > 26\,\text{GeV}$

Table 4.8: Triggers used in the W control region

at least 27 GeV. This leads to the distributions shown in figure 4.19. Through this control region a scaling factor for the W processes of 1.806 is determined leading to the distributions in figure 4.20. This scaling factor is very high as it describes that the Monte Carlo samples of the W processes only predict around 55% of the events that should be expected. Another problem of this control region is that it deviates too strongly from the signal regions. Because there is only one lepton allowed in the final state, every cut that requires two leptons can not be applied. This is especially important for the cuts dependent on the different mass predictions, because these only consist of mass cuts and angular cuts. Since there is only one visible lepton, the different masses of the mother particle can not be calculated and there is also no angle between two leptons. This means that all these cuts can not be applied in the control region concluding that the W processes can not be predicted through Monte Carlo samples and a scaling factor. Therefore, they have to be estimated through another method.

4.5.5 Fake Estimation

Fake background usually arises when QCD background is wrongly reconstructed as leptons. This fake background comes mostly from W and QCD multijet events [68]. It can also be generated through hadronically decaying top-quarks, but it was shown that the top background describes the data accurately. Therefore, a fake estimation will be used to describe the QCD and the W background. To estimate the fake background, new control regions have to be defined. The first one is called the same-sign control region (region B). In this region, only events are selected that contain two leptons with an equal charge as opposed to the different charge from the signal region. The second control region is the fake control region (region C). In this region, the lepton requirements are changed slightly. Instead of having medium identification requirements, the requirements for the identification of an electron are set to loose. Furthermore, the isolation requirement of the subleading lepton is reversed. The last control region is the fake same-sign control region, which is the combination of the two aforementioned (region D). With these three control regions, the fake background can be estimated in the signal region (region A).

But before the estimation can be done, it has to be analysed how much signal the control regions contain. This is done to make sure that the calculated fakes are not dependent on a possible signal as the goal for this analysis is to research if the signal exists. For this, the mass from the missing mass calculator in the four different regions is shown in figure 4.21 for a CP-odd Higgs boson with a mass of 60 GeV. The histograms for the other mass predictions can be found in the appendix B.6. It is shown that only the fake control region contains signal events. However, the signal is most of time small enough, especially for higher Higgs boson masses. Therefore, the control regions can be used to
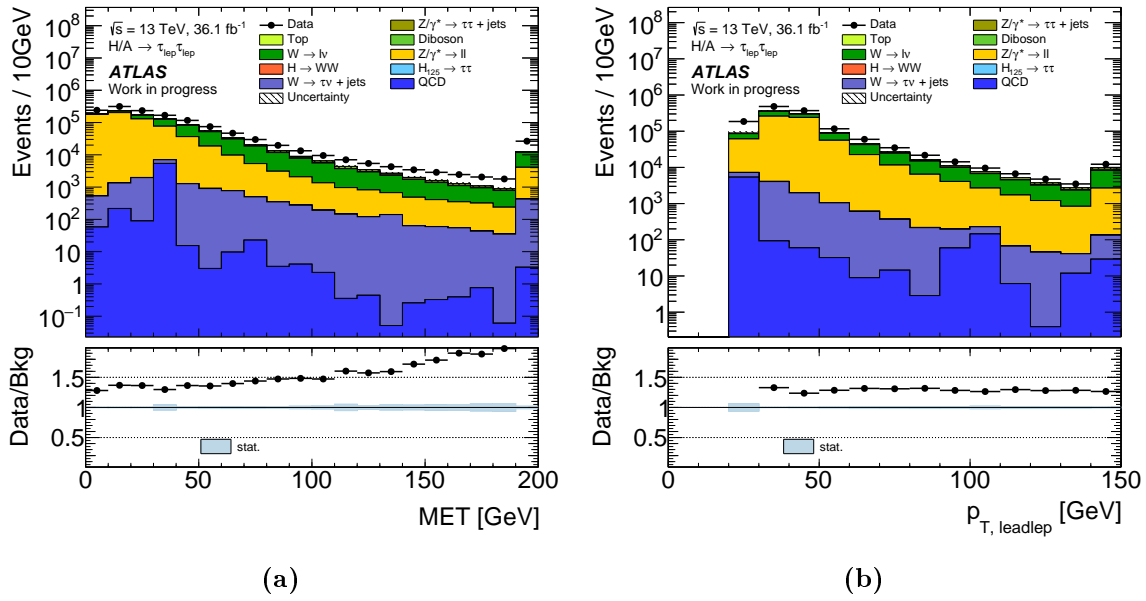
Figure 4.19: W control region plots for the analysis of a Higgs Boson with a mass of 60 GeV (a) Missing transverse energy (b) p_T of the leading lepton

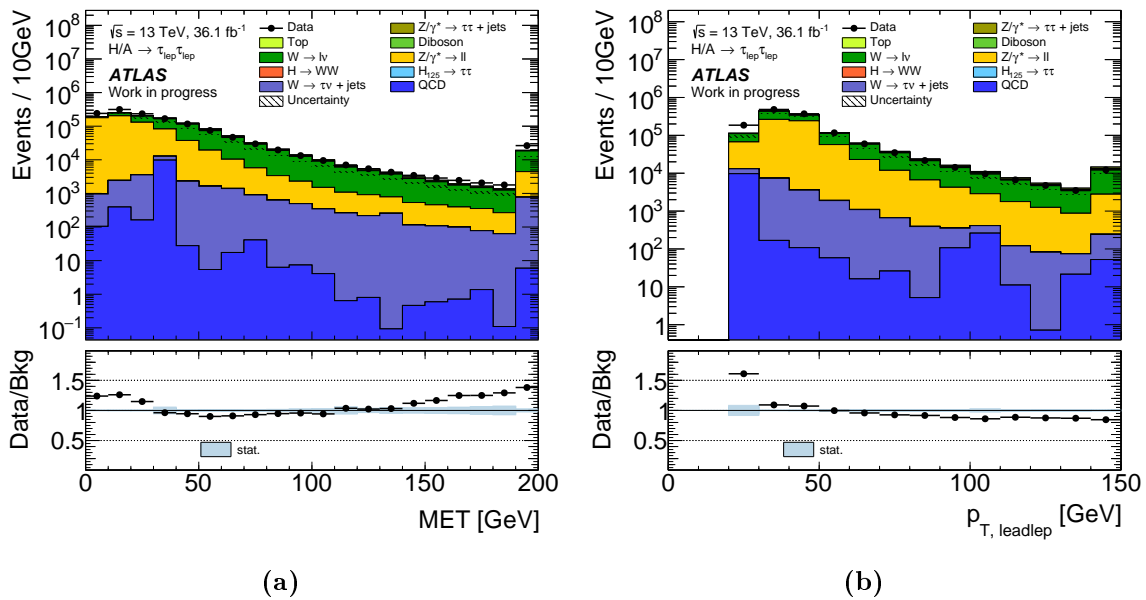**Figure 4.20:** W control region plots for the analysis of a Higgs Boson with a mass of 60 GeV and a scaling factor of 1.806 (a) Missing transverse energy (b) p_T of the leading lepton
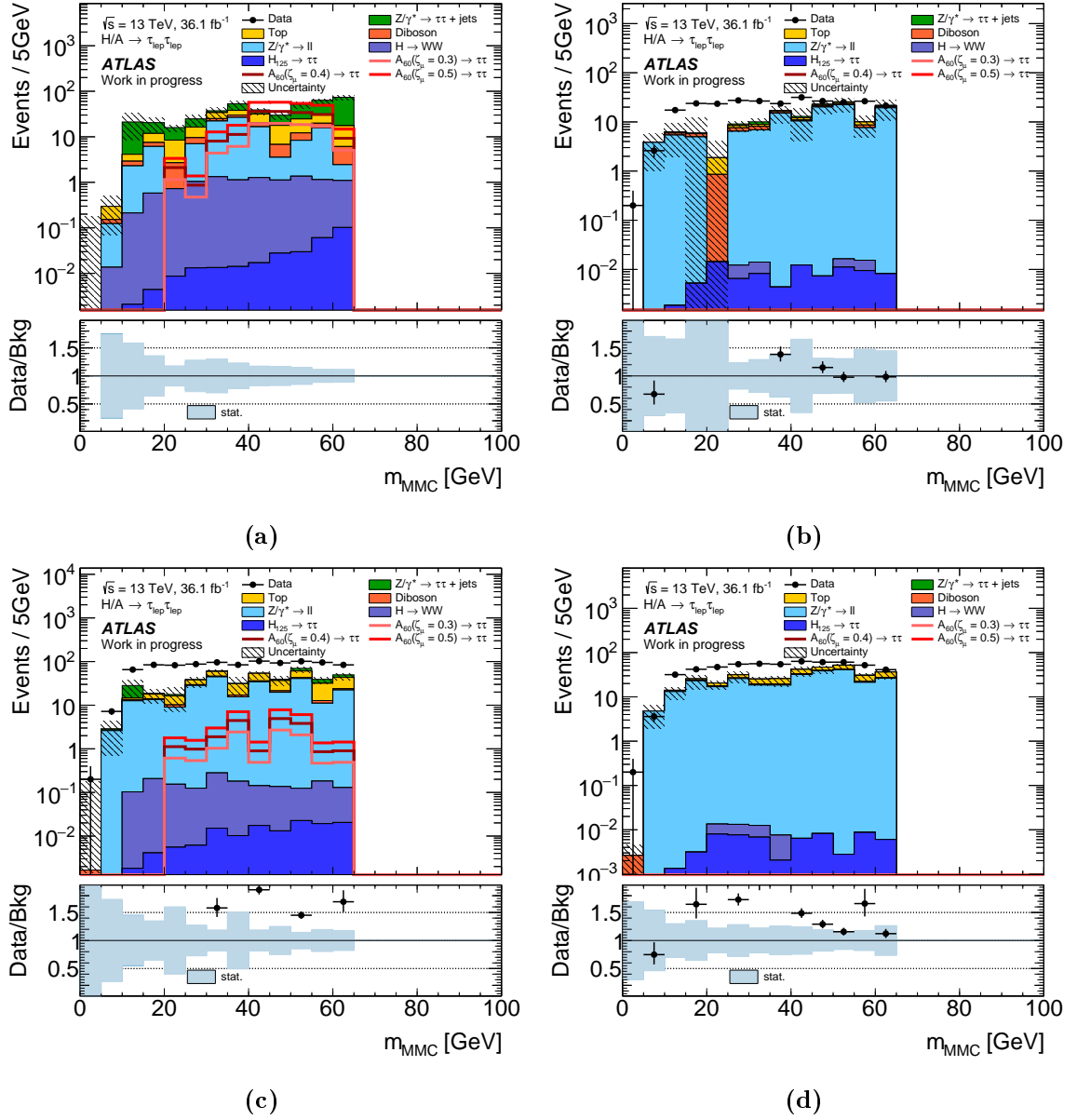
Figure 4.21: Mass from the missing mass calculator in the four different regions for a Higgs boson with a mass of 60 GeV (a) signal region A (b) same-sign region B (c) fake region C (d) fake same-sign region D

estimate the fake background.

For the estimation, the number of fakes is determined in region C for every bin of a histogram. This number is then multiplied with a fake factor that is determined through regions B and D and the fakes in each bin are then added to the histogram in region A. Shortly this can be described through

$$n_{Fakes}^{A} = n_{Fakes}^{C} \cdot f_{trans} \tag{4.2}$$

with f_{trans} being

$$f_{trans} = \frac{n_{Fakes}^{B}}{n_{Fakes.}^{D}} \tag{4.3}$$

But f_{trans} is usually not a global factor. It is parametrised in the transverse momentum of the subleading lepton. Therefore, the distribution for the p_T of the subleading lepton is generated in regions B and D. Both distributions are shown for a 60 GeV Higgs boson in figure 4.22, while the distributions for the other Higgs boson can be found in the appendix B.6. In both histograms the number of fakes is determined by subtracting the background from the data and after that the ratio $\frac{n_{Fakes}^{B}}{n_{Fakes}^{D}}$ is calculated for every bin. Because negative fakes are assumed to be non-existent the number of fakes in a bin is set to 0 if the number of background events is higher than the number of data events. If the number of fakes in a bin is 0 for both control regions B and D, the fake factor is set to 1. With this, the fake factors in dependence on the p_T of the subleading lepton can be calculated for every mass prediction. The fake factors are shown in figure 4.23. The first bin with a range of $0\,\mathrm{GeV} < p_T^{subleadlep} < 8\,\mathrm{GeV}$ has a fake factor of 1.0. This was expected as the subleading lepton has at least a p_T of 8 GeV due to electron requirements. This results in the number of data or background events in this bin being 0 independent of the region and therefore a fake factor of 1. Most of the other bins have a fake factor that is smaller than 1.0, which is expected as the fake control region should contain more fake events. Only the last bin with a range of $p_T > 65\,\mathrm{GeV}$ does not behave like that. However, the large uncertainty leads to the assumption that this is probably a result of the low number of entries in this bin. And since the number of events containing a subleading lepton with a $p_T > 65\,\mathrm{GeV}$ is expected to be low, this will not influence the analysis significantly.

After the fake factors are calculated, the events in control region C can be used to estimate the number of fakes in the signal region. Every event in control region C is weighted with a fake factor dependent on the transverse momentum of the subleading lepton. Then the background events in control region C are subtracted from the data events for every bin and this number of fakes is added to the histogram in the signal region. The result of this estimation can be seen in chapter 5. But before the result can be analysed, it has to be tested, if the calculation of the fakes led to the right background prediction. Therefore, the background combined with the estimated fakes is compared to the data. But this has to be done in a region without signal events to be sure that differences are not resulting from a possible signal. A region that fulfils this requirement can be achieved by selecting events with a mass, calculated from the missing mass calculator, smaller than 20 GeV. Furthermore, the fake estimation in this region is also compared to the original background estimation through W Monte Carlo samples. The results are shown in figure 4.24 for the 60 GeV Higgs boson and in the appendix B.7 for the other Higgs boson masses. It is shown that the estimated fakes together with the other background Monte Carlo samples describe the data well and that the description is better than the estimation with W Monte Carlo samples. Therefore, the prediction with fake background is
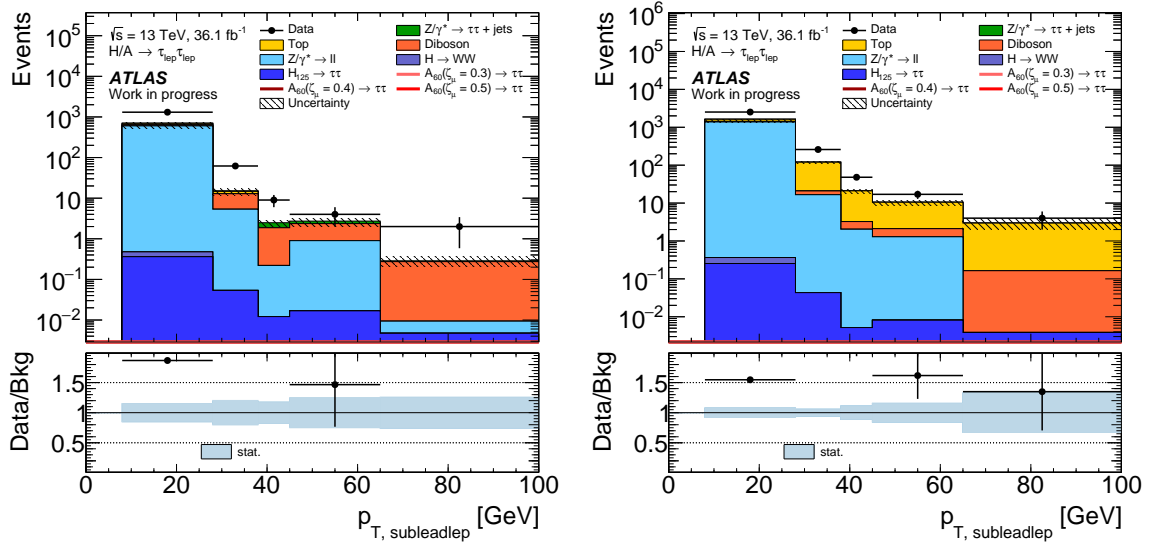
(a)   (b)

Figure 4.22: p_T of the subleading lepton for a 60 GeV Higgs boson in the (a) same-sign control region (b) fake same-sign control region
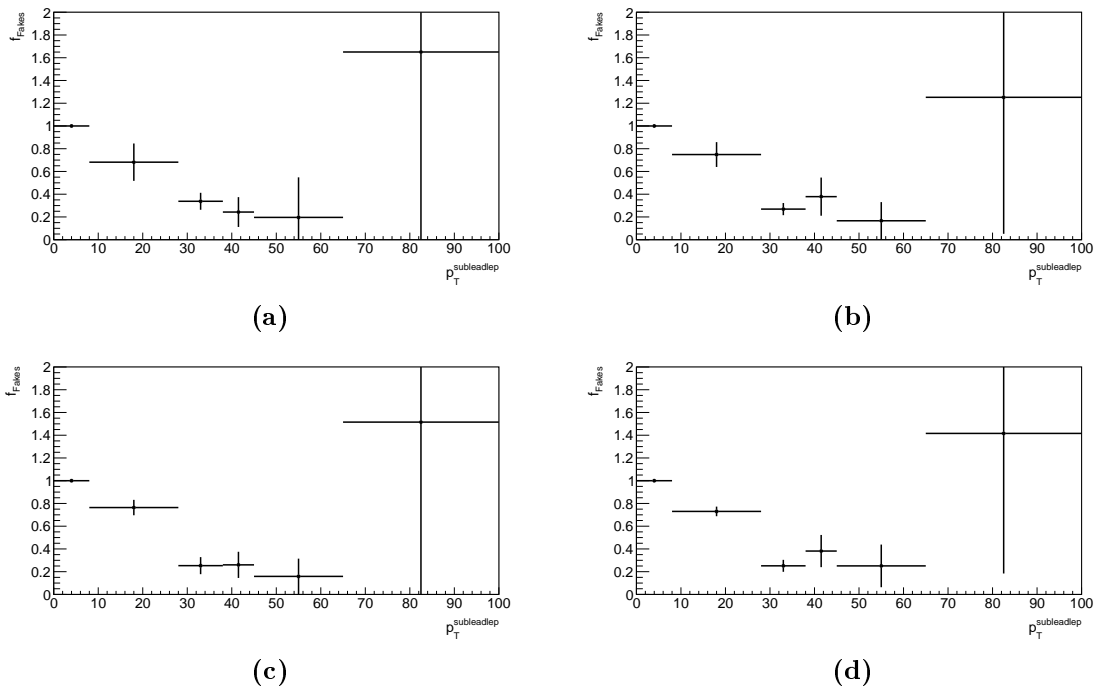
(a)   (b)

(c)   (d)

Figure 4.23: Fake factors in dependence on the p_T of the subleading lepton for a Higgs boson with a mass of (a) 60 GeV (b) 70 GeV (c) 80 GeV (d) 90 GeV
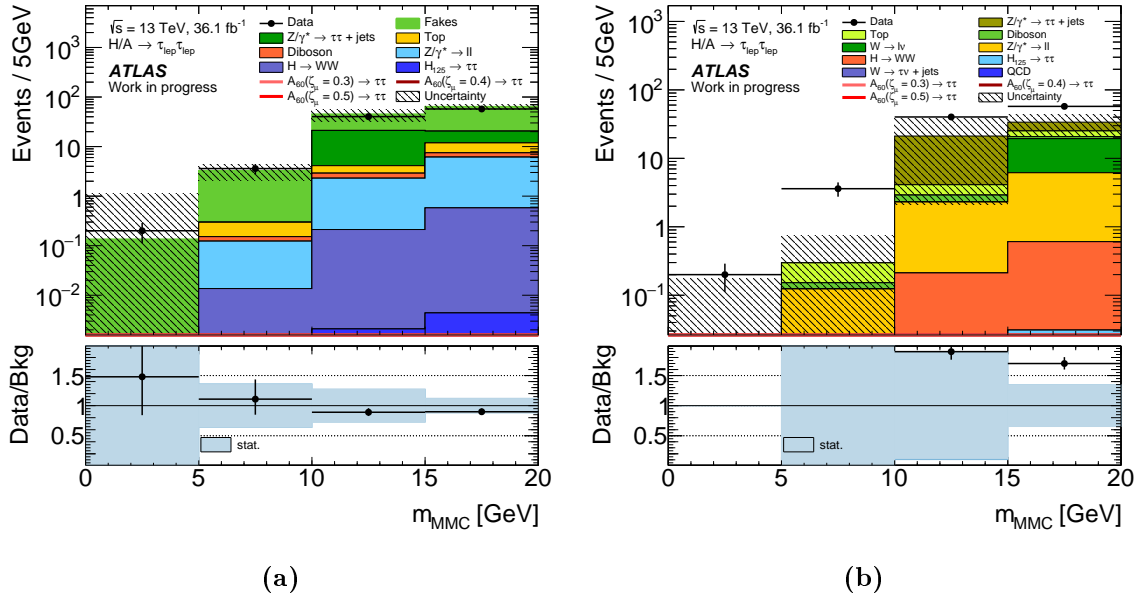
Figure 4.24: Mass distribution from the missing mass calculator in the region $0\,\text{GeV} < m_{MMC} < 20\,\text{GeV}$ for a $60\,\text{GeV}$ Higgs boson (a) with fake estimation (b) without fake estimation

used in this analysis.

5 Results

This section shows the results for the analysis of a light CP-odd Higgs boson. However, an unblinding of the signal region is not done in this master thesis. Therefore, this section will focus on conclusions that can be drawn from an analysis of the Monte Carlo predictions. This includes the calculation of the expected discovery significance to determine the sensitivity of the analysis and the calculation of the expected upper limits for the different mass regions.

5.1 Expected Discovery Significance

After the validation of the background and the calculation of the fake background in the previous chapter the Monte Carlo prediction of the background can now be analysed. The distributions for the mass from the missing mass calculator are shown in figure 5.1 for all mass predictions. It can be noticed that the ratio between background and signal is higher for the lower mass Higgs bosons. Especially for a 60 GeV Higgs boson and $\zeta_\mu = 0.5$, it is shown that the number of signal events is nearly equal to the number of background events in some bins. However, it has to be kept in mind, that there is no visualisation of the statistical uncertainties for the signal. That the statistical uncertainty is not negligible is shown by the slight fluctuations in the signal distribution. For comparison, the results in the mass of the dilepon system are shown in figure 5.2. As expected, the ratio between the signal and background is still good. But unlike before there are no bins, where the number of signal events nearly reaches the number of background events. The conclusion is that some observables might be more sensitive for the analysis, but also that the statistical significance can not be ignored for the signal process.

The overall sensitivities of the analyses are now determined by calculating the expected discovery significance for different predictions. For this, equation (2.80) is used. But it is made aware again, that the expected discovery significance is only calculated with the total number of signal and background events. Therefore, it does not describe the sensitivity of different observables. In addition to that, an exact number for the significance can not be calculated, since the cross-section of the signal is dependent on the coupling to up-type quarks and this is one of the free parameters. A general area for the significance can still be determined. In table 5.1 the expected discovery significance is presented for the different mass predictions and three values for ζ_μ. The significance is shown after the baseline selection and after applying all cuts including the fake background estimation. There are several things that can be analysed with these results. First, it can be seen that nearly all of the observed ζ_μ scenarios have a significance of over 5. This shows that a discovery with the presented analysis is possible for all the researched mass points. It can also be noticed that the significance is very high in a lot of cases with a maximum significance of 20. Especially when comparing this to the discovery significance of the SM Higgs, which was about 5 [69], this result seems very high. However, there are some differences between the two processes. First of all, the value for ζ_μ is vari-

(a)

(b)

(c)

(d)
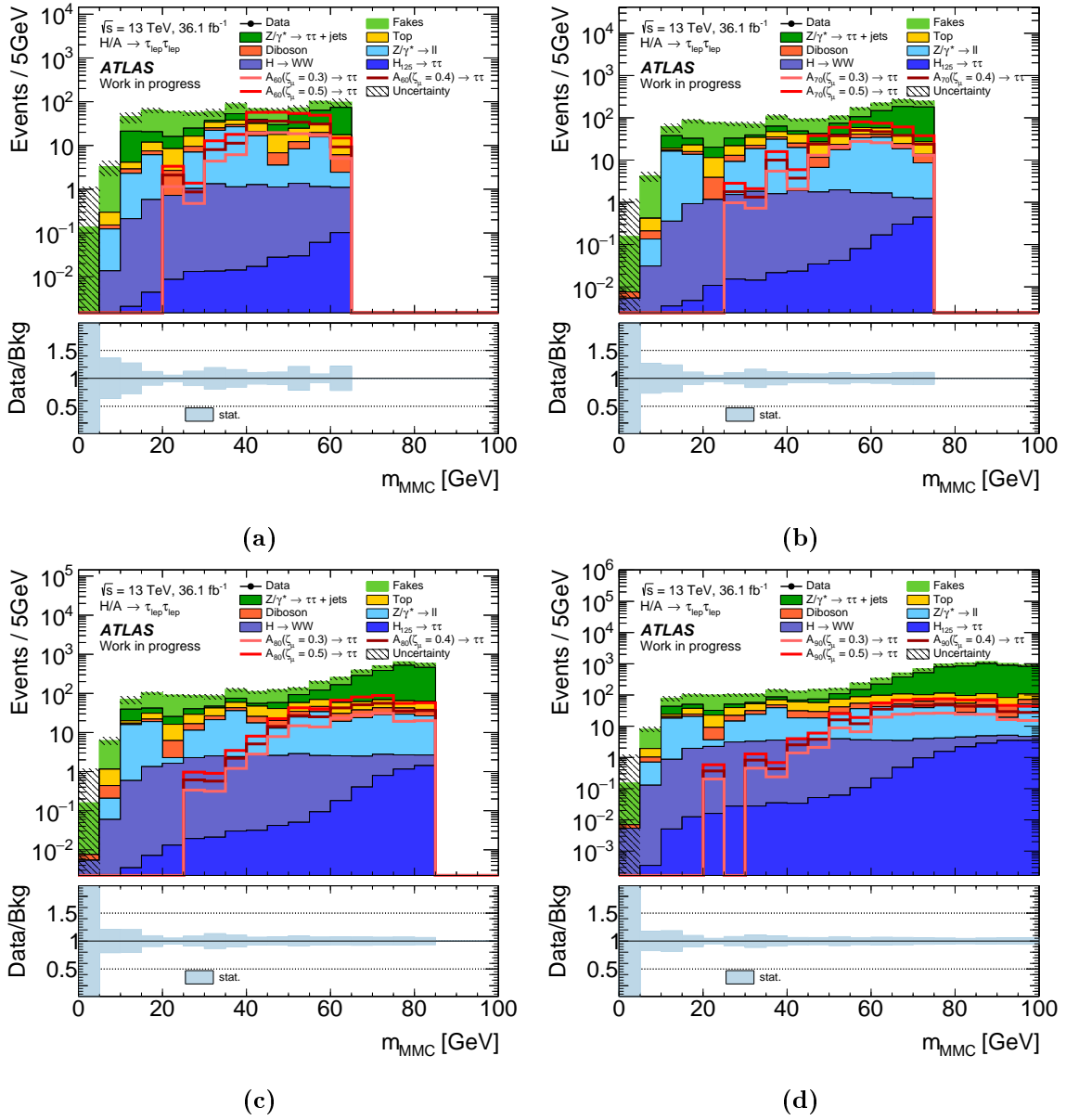
Figure 5.1: Mass distribution from the missing mass calculator in the signal region for a Higgs boson with a mass of (a) 60 GeV (b) 70 GeV (c) 80 GeV (d) 90 GeV

	$\zeta_\mu = 0.3$		$\zeta_\mu = 0.4$		$\zeta_\mu = 0.5$	
	Baseline Selection	Final	Baseline Selection	Final	Baseline Selection	Final
$m_A =$60 GeV	2.15 ± 0.14	7.31 ± 0.61	3.94 ± 0.25	13.19 ± 1.09	6.26 ± 0.40	20.61 ± 1.67
$m_A =$70 GeV	2.81 ± 0.15	7.07 ± 0.53	5.12 ± 0.28	12.77 ± 0.96	8.12 ± 0.44	20.02 ± 1.48
$m_A =$80 GeV	3.40 ± 0.15	6.29 ± 0.37	6.17 ± 0.26	11.35 ± 0.66	9.75 ± 0.42	17.83 ± 1.03
$m_A =$90 GeV	3.66 ± 0.13	4.89 ± 0.21	6.62 ± 0.23	8.84 ± 0.37	10.45 ± 0.37	13.90 ± 0.58

Table 5.1: Expected discovery significance calculated with equation (2.80) for different masses and ζ_μ after the baseline selection and after the final background estimation
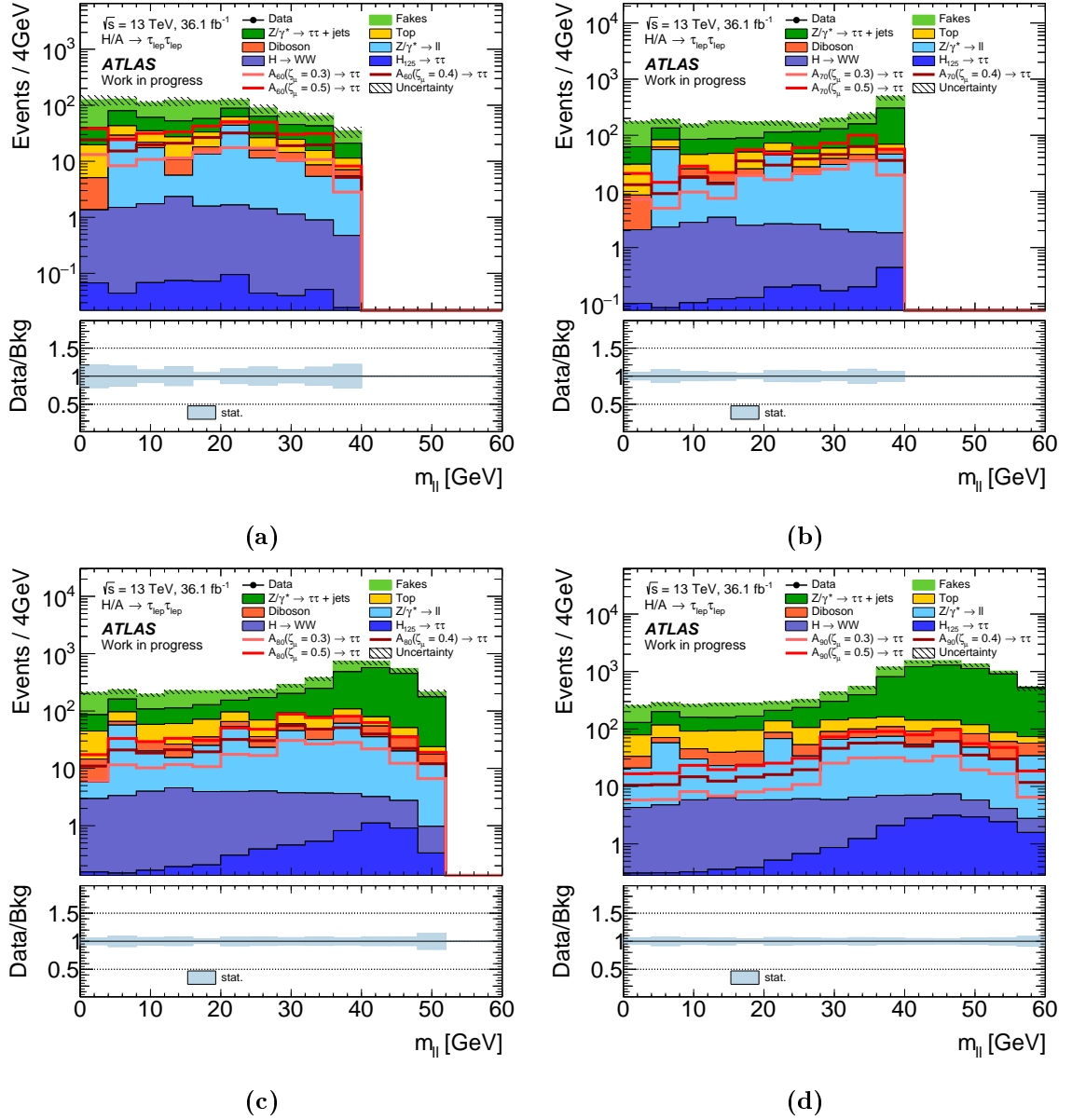
Figure 5.2: Mass of the dilepton system in the signal region for a Higgs boson with a mass of (a) 60 GeV (b) 70 GeV (c) 80 GeV (d) 90 GeV

able. This means that the discovery significance can be smaller. If ζ_μ should have a value of 0.3, the expected discovery significance is 7 at maximum. Another difference is the cross-section of the CP-odd Higgs boson. Because of the small mass, the cross-sections of the possible Higgs bosons can be higher than the cross-section for the SM Higgs boson. A 60 GeV CP-odd Higgs boson for example has a cross-section of around 100 pb if $\zeta_\mu = 0.5$. This is more than double compared to the SM Higgs boson cross-section [70]. This then leads to a higher significance. But the most important difference is probably the branching ratio of the CP-odd Higgs boson. It was assumed that the CP-odd Higgs boson decays with a branching ratio of 100% into a pair of τ leptons which then decay with a ratio of 6.21% into exactly one muon and one electron. In comparison, the important discovery channels for the SM Higgs boson $H \to ZZ$ and $H \to \gamma\gamma$ [69] only had a branching ratio of 2.6% and 0.2% [29]. Furthermore, this decay channel already reduces a lot of the important backgrounds like $Z \to ll$ and the W background. Therefore, a higher discovery significance can be expected.

Second, it can be notice that the expected discovery significance for the lighter CP-odd Higgs bosons is smaller after the baseline selection even though the cross-section of these bosons is supposed to be higher. The reason for this is that the Higgs boson is produced primarily at rest, which means that the combined energy of the two leptons and the four neutrinos equals the mass of the Higgs boson. For a light Higgs boson, this results in a final state where each lepton does not carry a lot of energy. But as it was explained in section 4.4.2, the energy for the leptons must be at least 33 GeV due to the trigger and the muon itself needs to have an energy of at least 25 GeV. This is not always achieved by a light Higgs boson at rest, which is why those events are not selected. This means that more events are rejected in the baseline selection for lighter CP-odd Higgs bosons, which leads to a smaller number of events and therefore a smaller expected discovery significance. But because of the low mass of these Higgs bosons, the cuts dependent on the prediction can be stronger compared to heavier Higgs bosons. In the end this results in an overall higher expected significance for the lighter Higgs bosons. It is also shown that the largest difference in the final significance is found between the 80 GeV and the 90 GeV Higgs boson. This was expected as the 90 GeV Higgs boson has nearly the same mass as the Z boson. Therefore, the mass peak of the 90 GeV Higgs boson is directly at the mass peak of the Z boson and since this is the most dominant background, this leads to a considerably lower expected significance.

5.2 Expected Upper Limits

In this section the expected upper limits for the different mass predictions are shown. The parameter μ that is analysed in this calculation is the coupling to the up-type quarks ζ_μ as this one determines the cross-section of the process. However, there are two problems. The first problem is that table 4.4 only provides six values for this parameter, which increases the uncertainty of the upper limit calculation. The second problem is that the cross-section is not monotonically increasing or decreasing with a rising parameter ζ_μ. This means that two different limits have to be calculated, an upper limit for positive ζ_μ and a lower limit for negative ζ_μ. This results in even less values for the upper limit calculation. However, since the coupling to upper limits only influences the cross-section by providing a scaling factor to the cross-section of a Standard Model Higgs boson of the same mass, the variable μ of the upper limit calculation is set to this scaling factor. The value μ can then take every value above

0. After finding the upper limit on this scaling factor, the corresponding positive and negative ζ_μ are calculated. For this, the six values of table 4.4 are used to interpolate a second order polynomial function that is shown in figure 5.3 for the Higgs Boson with a mass of 60 GeV. The equation for this function is

$$f_\sigma(\zeta_\mu) = 2.633 \cdot \zeta_\mu^2 - 0.102 \cdot \zeta_\mu + 0.003 \tag{5.1}$$

which can then be used to determine the upper and lower limits for ζ_μ from the upper limits of f_σ. The interpolated functions for the other masses are displayed in the appendix B.8.

The results for the upper limits on the scaling factors can be calculated through the method presented in section 2.3.1. But because the signal region is not unblinded, only the expected upper limits are determined, where pseudo data is created through the expected background. The systematic uncertainties on the Monte Carlo samples consist of the uncertainty on the luminosity [47] and the uncertainty on the cross-section calculation. The uncertainties of the fake background are a calculated via Gaussian error propagation of the systematic uncertainties from the backgrounds used. The result is shown in figure 5.4. It can be noticed that the expected upper limits are smaller the lower the mass of the Higgs boson. This was expected as the expected discovery significance is a lot higher for smaller masses and therefore the scaling factor must be small if the SM hypothesis is assumed to be true. From these scaling factors, the expected limits on the up-type quark coupling ζ_μ can be calculated, which are displayed in table 5.2. The table shows, which values outside a certain interval would be excluded if the SM was true with a confidence level of 68% (1σ) and 95% (2σ). For example, the expected limit for the up-type quark coupling of a 60 GeV CP-odd Higgs boson ranges between $0.274^{+0.081}_{-0.069}$ and $-0.236^{+0.069}_{-0.081}$. Values of ζ_μ outside of this interval would be excluded with a significance of $Z = 2$ if the SM theory is true. This corresponds to a confidence level of 95%.

	Mean		$\pm 1\sigma$		$\pm 2\sigma$	
	positive ζ_μ	negative ζ_μ	positive ζ_μ	negative ζ_μ	positive ζ_μ	negative ζ_μ
$m_A =$60 GeV	0.274	-0.236	$+0.041$ -0.039	$+0.039$ -0.041	$+0.081$ -0.069	$+0.069$ -0.081
$m_A =$70 GeV	0.297	-0.265	$+0.047$ -0.043	$+0.043$ -0.047	$+0.097$ -0.076	$+0.076$ -0.097
$m_A =$80 GeV	0.370	-0.344	$+0.062$ -0.052	$+0.052$ -0.061	$+0.127$ -0.095	$+0.096$ -0.126
$m_A =$90 GeV	0.418	-0.395	$+0.086$ -0.047	$+0.047$ -0.087	$+0.169$ -0.097	$+0.096$ -0.170

Table 5.2: Expected limits for the coupling to up-type quarks for the different masses of A
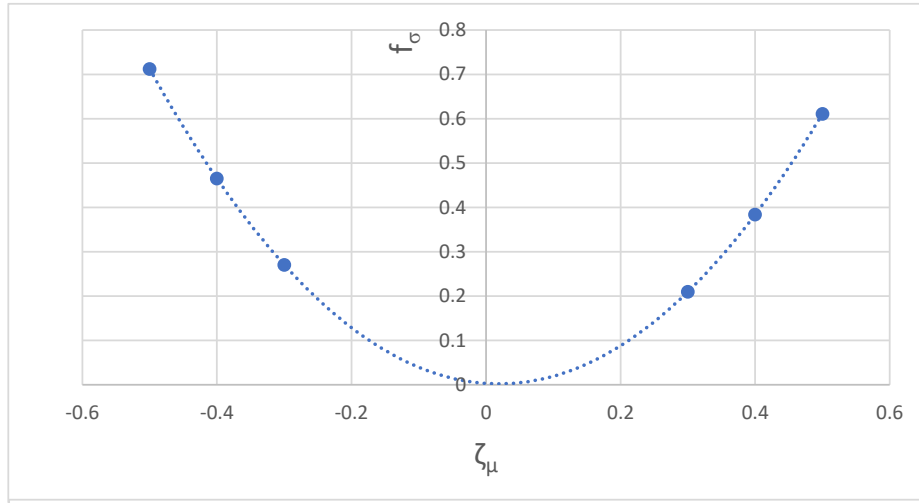
Figure 5.3: Parabolic function for the scale factor on the cross-section in dependence of ζ_μ
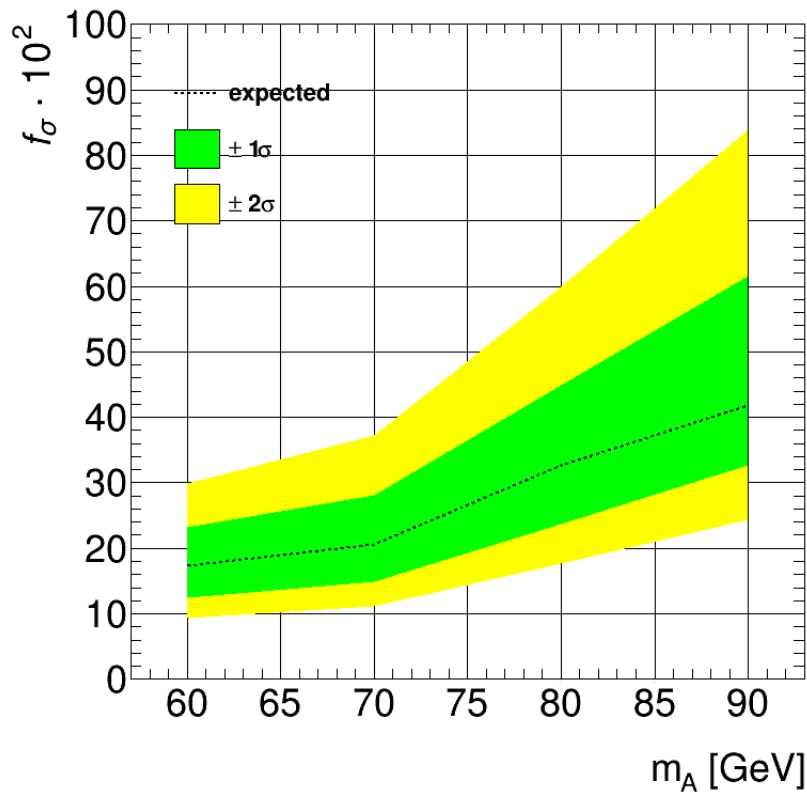

Figure 5.4: Expected upper limits for the scaling factor on the A boson cross-section in dependence on the mass. The green band represents the 1σ uncertainty and the yellow band the 2σ uncertainty.

6 Summary and Outlook

In this study an analysis was shown to test for the existence of a light CP-odd Higgs boson. The analysis was done for data taken with the ATLAS detector at a center-of-mass energy of $13\,\mathrm{TeV}$ and a luminosity of $36.1\,\mathrm{fb}^{-1}$. During this thesis, the background was analysed and estimated. Cuts for the different mass predictions were shown so that the expected discovery significance was maximised. The background in the signal region is mostly estimated with Monte Carlo simulations and is scaled with scaling factors determined from different control regions. However, the W and QCD backgrounds are estimated with data using a fake factor method that includes three different control regions. These control regions are a same-sign, a fake and a fake same-sign control region. The fake factors are calculated in dependence on the p_T of the subleading lepton in the same-sign and fake same-sign control region. After that, the fake background from the fake region is weighted with these fake factors to estimate the fake background in the signal region. It was shown that this fake background can describe the data well.

The results of the analysis focus on an evaluation of the background and the signal of the predicted Higgs bosons. It was shown that a very high expected discovery significance can be achieved, especially for the light CP-odd Higgs bosons. This could lead to a discovery. However, it was also shown that the expected discovery significance decreases for CP-odd Higgs bosons with masses similar to the Z boson mass. For one certain up-type quark coupling, this led to an expected significance below $Z = 5$, which would not be enough for a discovery. In this case, the analysis could be extended on the semi-leptonic or even hadronic decay channels of the τ lepton. It was shown in section 4.3.1 that the angle between the decay planes of the visible decay products differs for a Z boson and a CP-odd Higgs boson. This could be used to distinguish the signal more from the background. But it has to be kept in mind, that other challenges come with the observation of hadronically decaying τ leptons. For example, measuring the properties of electrons and muons is more precise than that of a jet produced by a τ lepton. Furthermore, the QCD background that was rejected mostly during this analysis would be larger. This also influences the calculation of the fake background.

Additionally, the expected upper limits for the Higgs bosons show that even without a discovery a lot of information can be gained from this analysis. Especially for light CP-odd Higgs bosons a lot of values for the up-type quark coupling could be excluded if the data in the signal region is similar to the SM prediction. This could be very important as a certain value for the up-type quark coupling is needed so that the contributions of the 2HDM are enough to explain the deviation between the SM prediction and the measurements of the anomalous magnetic moment of the muon.

Therefore, unblinding the signal region can give important information about the flavour-aligned 2HDM in the future and what mass regions should be investigated furhter. Nevertheless, the analysis can also be extended in certain ways. The first extension can be the analysis of Higgs bosons with a lower mass than $60\,\mathrm{GeV}$, because in the theory of the flavour-aligned 2HDM the mass of the Higgs boson can be far lower. Analysis of a lighter CP-odd Higgs boson could use harder cuts on mass

and angular distributions which could lead to a very high discovery significance. However, it was also shown in table 5.1 that the number of signal events after the baseline selection decreases with a lower mass due to the p_T of the lepton trigger. This could become problematic for lower masses as too few signal events would lead to high uncertainties in the analysis. Therefore, it has to be estimated first how many signal events are selected through the baseline selection. In the case that these are too few, a solution could be to use another trigger. But while single-lepton triggers usually need a lower p_T requirement of around $26\,\mathrm{GeV}$, this would also increase other backgrounds like the W background. Furthermore, jet and MET triggers also require a very high p_T for a jet or a very high missing transverse energy. This is not often achieved by a light CP-odd Higgs boson. Another solution could be the increase of the luminosity. In the future, the goal for the LHC is to reach an integrated luminosity of $100\,\mathrm{fb}^{-1}$ in 2019 and $300\,\mathrm{fb}^{-1}$ in 2024 [71]. This increase in luminosity would also increase the number of signal events for a light CP-odd Higgs boson and therefore decrease the statistical uncertainties. And while this also increases the number of background events, the harder cuts would probably lead to a higher expected discovery significance.

The second way to extend the analysis is by looking into more of the parameters. For example in this analysis the coupling to leptons ζ_l was assumed to be very high, so that the branching ratio of $A \to \tau\tau$ is nearly 100%. Upper limits could be calculated for ζ_l and for a combination of ζ_l and ζ_μ. Furthermore, the influence on the coupling to down-type quarks can be analysed and upper limits can be found for this parameter. It could be determined, which combination of parameters is excluded and which combination of not excluded parameters is still able to explain the deviation between the SM prediction and the measurement of the anomalous magnetic moment of the muon.

A List of Monte-Carlo Samples

In this section, the MC samples together with their cross-section, K-Factor and filter efficiency are shown. The values for cross-section, K-Factor and filter efficiency were taken from [72].

A.1 $Z \to \tau\tau$

Dataset Name	XSec [pb]	K-Factor	Filter Eff.
mc15_13TeV.364128.Sherpa_221_NNPDF30NNLO_Ztautau_MAXHTPTV0_70_CVetoBVeto.merge.DAOD_HIGG4D1.e5307_s2726_r7772_r7676_p3017	1981.7	0.9751	0.82142
mc15_13TeV.364129.Sherpa_221_NNPDF30NNLO_Ztautau_MAXHTPTV0_70_CFilterBVeto.merge.DAOD_HIGG4D1.e5307_s2726_r7772_r7676_p3017	1981.6	0.9751	0.10907
mc15_13TeV.364130.Sherpa_221_NNPDF30NNLO_Ztautau_MAXHTPTV0_70_BFilter.merge.DAOD_HIGG4D1.e5307_s2726_r7772_r7676_p3017	1982.1	0.9751	0.065759
mc15_13TeV.364131.Sherpa_221_NNPDF30NNLO_Ztautau_MAXHTPTV70_140_CVetoBVeto.merge.DAOD_HIGG4D1.e5307_s2726_r7772_r7676_p3017	110.56	0.9751	0.6926
mc15_13TeV.364132.Sherpa_221_NNPDF30NNLO_Ztautau_MAXHTPTV70_140_CFilterBVeto.merge.DAOD_HIGG4D1.e5307_s2726_r7772_r7676_p3017	110.55	0.9751	0.1902
mc15_13TeV.364133.Sherpa_221_NNPDF30NNLO_Ztautau_MAXHTPTV70_140_BFilter.merge.DAOD_HIGG4D1.e5307_s2726_r7772_r7676_p3017	110.63	0.9751	0.110886
mc15_13TeV.364134.Sherpa_221_NNPDF30NNLO_Ztautau_MAXHTPTV140_280_CVetoBVeto.merge.DAOD_HIGG4D1.e5307_s2726_r7772_r7676_p3017	40.793	0.9751	0.61823
mc15_13TeV.364135.Sherpa_221_NNPDF30NNLO_Ztautau_MAXHTPTV140_280_CFilterBVeto.merge.DAOD_HIGG4D1.e5307_s2726_r7772_r7676_p3017	40.718	0.9751	0.23417
mc15_13TeV.364136.Sherpa_221_NNPDF30NNLO_Ztautau_MAXHTPTV140_280_BFilter.merge.DAOD_HIGG4D1.e5307_s2726_r7772_r7676_p3017	40.735	0.9571	0.15608
mc15_13TeV.364137.Sherpa_221_NNPDF30NNLO_Ztautau_MAXHTPTV280_500_CVetoBVeto.merge.DAOD_HIGG4D1.e5307_s2726_r7772_r7676_p3017	8.6642	0.9751	0.56327
mc15_13TeV.364138.Sherpa_221_NNPDF30NNLO_Ztautau_MAXHTPTV280_500_CFilterBVeto.merge.DAOD_HIGG4D1.e5313_s2726_r7772_r7676_p3017	8.6756	0.9751	0.17626
mc15_13TeV.364139.Sherpa_221_NNPDF30NNLO_Ztautau_MAXHTPTV280_500_BFilter.merge.DAOD_HIGG4D1.e5313_s2726_r7772_r7676_p3017	8.6797	0.9751	0.17626
mc15_13TeV.364140.Sherpa_221_NNPDF30NNLO_Ztautau_MAXHTPTV500_1000.merge.DAOD_HIGG4D1.e5307_s2726_r7772_r7676_p3017	1.8079	0.9751	1.0
mc15_13TeV.364141.Sherpa_221_NNPDF30NNLO_Ztautau_MAXHTPTV1000_E_CMS.merge.DAOD_HIGG4D1.e5307_s2726_r7772_r7676_p3017	0.14823	0.9751	1.0
mc15_13TeV.364210.Sherpa_221_NN30NNLO_Ztt_Ml110_40_MAXHTPTV0_70_BVeto.merge.DAOD_HIGG4D1.e5421_s2726_r7772_r7676_p3017	2415.3	0.9751	0.96539
mc15_13TeV.364211.Sherpa_221_NN30NNLO_Ztt_Ml110_40_MAXHTPTV0_70_BFilter.merge.DAOD_HIGG4D1.e5421_s2726_r7772_r7676_p3017	2414.3	0.9751	0.034653
mc15_13TeV.364212.Sherpa_221_NN30NNLO_Ztt_Ml110_40_MAXHTPTV70_280_BVeto.merge.DAOD_HIGG4D1.e5421_s2726_r7772_r7676_p3017	50.408	0.9751	0.89316
mc15_13TeV.364213.Sherpa_221_NN30NNLO_Ztt_Ml110_40_MAXHTPTV70_280_BFilter.merge.DAOD_HIGG4D1.e5421_s2726_r7772_r7676_p3017	50.456	0.9751	0.10985
mc15_13TeV.364214.Sherpa_221_NN30NNLO_Ztt_Ml110_40_MAXHTPTV280_E_CMS_BVeto.merge.DAOD_HIGG4D1.e5421_s2726_r7772_r7676_p3017	3.2837	0.9751	0.85492
mc15_13TeV.364215.Sherpa_221_NN30NNLO_Ztt_Ml110_40_MAXHTPTV280_E_CMS_BFilter.merge.DAOD_HIGG4D1.e5421_s2726_r7772_r7676_p3017	3.2805	0.9751	0.15568
mc15_13TeV.344443.Sherpa_NNPDF30NNLO_Ztautau2jets_Min_N_TChannel_CSSKIN.merge.DAOD_HIGG4D1.e5231_s2726_r7772_r7676_p2949	0.63487	1.0	1.0

A.2 $Z \to ee$

Dataset Name	XSec [pb]	K-Factor	Filter Eff.
mc15_13TeV.364114.Sherpa_221_NNPDF30NNLO_Zee_MAXHTPTV0_70_CVetoBVeto.merge.DAOD_HIGG4D1.e5299_s2726_r7772_r7676_p3017	1981.5	0.9751	0.82141
mc15_13TeV.364115.Sherpa_221_NNPDF30NNLO_Zee_MAXHTPTV0_70_CFilterBVeto.merge.DAOD_HIGG4D1.e5299_s2726_r7772_r7676_p3017	1981.7	0.9751	0.11405
mc15_13TeV.364116.Sherpa_221_NNPDF30NNLO_Zee_MAXHTPTV0_70_BFilter.merge.DAOD_HIGG4D1.e5299_s2726_r7772_r7676_p3017	1982.1	0.9751	0.065757
mc15_13TeV.364117.Sherpa_221_NNPDF30NNLO_Zee_MAXHTPTV70_140_CVetoBVeto.merge.DAOD_HIGG4D1.e5299_s2726_r7772_r7676_p3017	110.63	0.9751	0.69432
mc15_13TeV.364118.Sherpa_221_NNPDF30NNLO_Zee_MAXHTPTV70_140_CFilterBVeto.merge.DAOD_HIGG4D1.e5299_s2726_r7772_r7676_p3017	110.45	0.9751	0.18697
mc15_13TeV.364119.Sherpa_221_NNPDF30NNLO_Zee_MAXHTPTV70_140_BFilter.merge.DAOD_HIGG4D1.e5299_s2726_r7772_r7676_p3017	110.49	0.9751	0.1197
mc15_13TeV.364120.Sherpa_221_NNPDF30NNLO_Zee_MAXHTPTV140_280_CVetoBVeto.merge.DAOD_HIGG4D1.e5299_s2726_r7772_r7676_p3017	40.711	0.9751	0.61632
mc15_13TeV.364121.Sherpa_221_NNPDF30NNLO_Zee_MAXHTPTV140_280_CFilterBVeto.merge.DAOD_HIGG4D1.e5299_s2726_r7772_r7676_p3017	40.671	0.9751	0.23293
mc15_13TeV.364122.Sherpa_221_NNPDF30NNLO_Zee_MAXHTPTV140_280_BFilter.merge.DAOD_HIGG4D1.e5299_s2726_r7772_r7676_p3017	40.674	0.9751	0.15333
mc15_13TeV.364123.Sherpa_221_NNPDF30NNLO_Zee_MAXHTPTV280_500_CVetoBVeto.merge.DAOD_HIGG4D1.e5299_s2726_r7772_r7676_p3017	8.6718	0.9751	0.56351
mc15_13TeV.364124.Sherpa_221_NNPDF30NNLO_Zee_MAXHTPTV280_500_CFilterBVeto.merge.DAOD_HIGG4D1.e5299_s2726_r7772_r7676_p3017	8.6654	0.9751	0.26618
mc15_13TeV.364125.Sherpa_221_NNPDF30NNLO_Zee_MAXHTPTV280_500_BFilter.merge.DAOD_HIGG4D1.e5299_s2726_r7772_r7676_p3017	8.86821	0.9751	0.17627
mc15_13TeV.364126.Sherpa_221_NNPDF30NNLO_Zee_MAXHTPTV500_1000.merge.DAOD_HIGG4D1.e5299_s2726_r7772_r7676_p3017	1.8098	0.9751	1.0
mc15_13TeV.364127.Sherpa_221_NNPDF30NNLO_Zee_MAXHTPTV1000_E_CMS.merge.DAOD_HIGG4D1.e5299_s2726_r7772_r7676_p3017	0.1487	0.9751	1.0
mc15_13TeV.364204.Sherpa_221_NN30NNLO_Zee_Ml110_40_MAXHTPTV0_70_BVeto.merge.DAOD_HIGG4D1.e5421_s2726_r7772_r7676_p3017	2415.4	0.9751	0.96508
mc15_13TeV.364205.Sherpa_221_NN30NNLO_Zee_Ml110_40_MAXHTPTV0_70_BFilter.merge.DAOD_HIGG4D1.e5421_s2726_r7772_r7676_p3017	2415.2	0.9751	0.034741
mc15_13TeV.364206.Sherpa_221_NN30NNLO_Zee_Ml110_40_MAXHTPTV70_280_BVeto.merge.DAOD_HIGG4D1.e5421_s2726_r7772_r7676_p3017	50.33	0.9751	0.89314
mc15_13TeV.364207.Sherpa_221_NN30NNLO_Zee_Ml110_40_MAXHTPTV70_280_BFilter.merge.DAOD_HIGG4D1.e5421_s2726_r7772_r7676_p3017	50.458	0.9751	0.1087
mc15_13TeV.364208.Sherpa_221_NN30NNLO_Zee_Ml110_40_MAXHTPTV280_E_CMS_BVeto.merge.DAOD_HIGG4D1.e5421_s2726_r7772_r7676_p3017	3.2544	0.9751	0.85473
mc15_13TeV.364209.Sherpa_221_NN30NNLO_Zee_Ml110_40_MAXHTPTV280_E_CMS_BFilter.merge.DAOD_HIGG4D1.e5421_s2726_r7772_r7676_p3017	3.2512	0.9751	0.15349
mc15_13TeV.344442.Sherpa_NNPDF30NNLO_Zee2jets_Min_N_TChannel_CSSKIN.merge.DAOD_HIGG4D1.e5231_s2726_r7772_r7676_p2949	0.63573	1.0	1.0
mc15_13TeV.345101.Sherpa_221_NNPDF30NNLO_Zee_MAXHTPTV0_70_VBFfilt.merge.DAOD_HIGG4D1.e5679_s2726_r7772_r7676_p3017	1981.8	0.9751	0.0086915
mc15_13TeV.345102.Sherpa_221_NNPDF30NNLO_Zee_MAXHTPTV70_140_VBFfilt.merge.DAOD_HIGG4D1.e5679_s2726_r7772_r7676_p3017	110.65	0.9751	0.081571

A.3 $Z \to \mu\mu$

Dataset Name	XSec [pb]	K-Factor	Filter Eff.
mc15_13TeV.364100.Sherpa_221_NNPDF30NNLO_Zmumu_MAXHTPTV0_70_CVetoBVeto.merge.DAOD_HIGG4D1.e5271_s2726_r7772_r7676_p3017	1982.3	0.9751	0.82179
mc15_13TeV.364101.Sherpa_221_NNPDF30NNLO_Zmumu_MAXHTPTV0_70_CFilterBVeto.merge.DAOD_HIGG4D1.e5271_s2726_r7772_r7676_p3017	1982.1	0.9751	0.11356
mc15_13TeV.364102.Sherpa_221_NNPDF30NNLO_Zmumu_MAXHTPTV0_70_BFilter.merge.DAOD_HIGG4D1.e5271_s2726_r7772_r7676_p3017	1981.6	0.9751	0.06574
mc15_13TeV.364103.Sherpa_221_NNPDF30NNLO_Zmumu_MAXHTPTV70_140_CVetoBVeto.merge.DAOD_HIGG4D1.e5271_s2726_r7772_r7676_p3017	109.07	0.9751	0.68978
mc15_13TeV.364104.Sherpa_221_NNPDF30NNLO_Zmumu_MAXHTPTV70_140_CFilterBVeto.merge.DAOD_HIGG4D1.e5271_s2726_r7772_r7676_p3017	108.94	0.9751	0.19588
mc15_13TeV.364105.Sherpa_221_NNPDF30NNLO_Zmumu_MAXHTPTV70_140_BFilter.merge.DAOD_HIGG4D1.e5271_s2726_r7772_r7676_p3017	108.98	0.9751	0.12052
mc15_13TeV.364106.Sherpa_221_NNPDF30NNLO_Zmumu_MAXHTPTV140_280_CVetoBVeto.merge.DAOD_HIGG4D1.e5271_s2726_r7772_r7676_p3017	39.884	0.9751	0.60179
mc15_13TeV.364107.Sherpa_221_NNPDF30NNLO_Zmumu_MAXHTPTV140_280_CFilterBVeto.merge.DAOD_HIGG4D1.e5271_s2726_r7772_r7676_p3017	39.857	0.9751	0.23545
mc15_13TeV.364108.Sherpa_221_NNPDF30NNLO_Zmumu_MAXHTPTV140_280_BFilter.merge.DAOD_HIGG4D1.e5271_s2726_r7772_r7676_p3017	39.892	0.9751	0.15628
mc15_13TeV.364109.Sherpa_221_NNPDF30NNLO_Zmumu_MAXHTPTV280_500_CVetoBVeto.merge.DAOD_HIGG4D1.e5271_s2726_r7772_r7676_p3017	8.526	0.9751	0.56012
mc15_13TeV.364110.Sherpa_221_NNPDF30NNLO_Zmumu_MAXHTPTV280_500_CFilterBVeto.merge.DAOD_HIGG4D1.e5271_s2726_r7772_r7676_p3017	8.5261	0.9751	0.26632
mc15_13TeV.364111.Sherpa_221_NNPDF30NNLO_Zmumu_MAXHTPTV280_500_BFilter.merge.DAOD_HIGG4D1.e5271_s2726_r7772_r7676_p3017	8.5276	0.9751	0.17657
mc15_13TeV.364112.Sherpa_221_NNPDF30NNLO_Zmumu_MAXHTPTV500_1000.merge.DAOD_HIGG4D1.e5271_s2726_r7772_r7676_p3017	1.7871	0.9751	1.0
mc15_13TeV.364113.Sherpa_221_NNPDF30NNLO_Zmumu_MAXHTPTV1000_E_CMS.merge.DAOD_HIGG4D1.e5271_s2726_r7772_r7676_p3017	0.14758	0.9751	1.0
mc15_13TeV.364198.Sherpa_221_NN30NNLO_Zmm_Mll10_40_MAXHTPTV0_70_BVeto.merge.DAOD_HIGG4D1.e5421_s2726_r7772_r7676_p3017	2414.1	0.9751	0.9653
mc15_13TeV.364199.Sherpa_221_NN30NNLO_Zmm_Mll10_40_MAXHTPTV0_70_BFilter.merge.DAOD_HIGG4D1.e5421_s2726_r7772_r7676_p3017	2414.9	0.9751	0.034454
mc15_13TeV.364200.Sherpa_221_NN30NNLO_Zmm_Mll10_40_MAXHTPTV70_280_BVeto.merge.DAOD_HIGG4D1.e5421_s2726_r7772_r7676_p3017	50.355	0.9751	0.89328
mc15_13TeV.364201.Sherpa_221_NN30NNLO_Zmm_Mll10_40_MAXHTPTV70_280_BFilter.merge.DAOD_HIGG4D1.e5421_s2726_r7772_r7676_p3017	50.274	0.9751	0.10899
mc15_13TeV.364202.Sherpa_221_NN30NNLO_Zmm_Mll10_40_MAXHTPTV280_E_CMS_BVeto.merge.DAOD_HIGG4D1.e5421_s2726_r7772_r7676_p3017	3.2385	0.9751	0.85348
mc15_13TeV.364203.Sherpa_221_NN30NNLO_Zmm_Mll10_40_MAXHTPTV280_E_CMS_BFilter.merge.DAOD_HIGG4D1.e5421_s2726_r7772_r7676_p3017	3.2818	0.9751	0.16029
mc15_13TeV.344441.Sherpa_NNPDF30NNLO_Zmm2jets_Min_N_TChannel_CSSKIN.merge.DAOD_HIGG4D1.e5231_s2726_r7772_r7676_p2949	0.63717	1.0	1.0
mc15_13TeV.345099.Sherpa_221_NNPDF30NNLO_Zmumu_MAXHTPTV0_70_VBFfilt.merge.DAOD_HIGG4D1.e5679_s2726_r7772_r7676_p3017	1981.0	0.9751	0.0035647
mc15_13TeV.345100.Sherpa_221_NNPDF30NNLO_Zmumu_MAXHTPTV70_140_VBFfilt.merge.DAOD_HIGG4D1.e5679_s2726_r7772_r7676_p3017	108.71	0.9751	0.067763

A.4 $W \to \tau\tau$

Dataset Name	XSec [pb]	K-Factor	Filter Eff.
mc15_13TeV.364184.Sherpa_221_NNPDF30NNLO_Wtaunu_MAXHTPTV0_70_CVetoBVeto.merge.DAOD_HIGG4D1.e5340_s2726_r7772_r7676_p3017	19156.0	0.9702	0.82465
mc15_13TeV.364185.Sherpa_221_NNPDF30NNLO_Wtaunu_MAXHTPTV0_70_CFilterBVeto.merge.DAOD_HIGG4D1.e5340_s2726_r7772_r7676_p3017	19149.0	0.9702	0.13157
mc15_13TeV.364186.Sherpa_221_NNPDF30NNLO_Wtaunu_MAXHTPTV0_70_BFilter.merge.DAOD_HIGG4D1.e5340_s2726_r7772_r7676_p3017	19147.0	0.9702	0.045038
mc15_13TeV.364187.Sherpa_221_NNPDF30NNLO_Wtaunu_MAXHTPTV70_140_CVetoBVeto.merge.DAOD_HIGG4D1.e5340_s2726_r7772_r7676_p3017	944.97	0.9702	0.67644
mc15_13TeV.364188.Sherpa_221_NNPDF30NNLO_Wtaunu_MAXHTPTV70_140_CFilterBVeto.merge.DAOD_HIGG4D1.e5340_s2726_r7772_r7676_p3017	946.38	0.9702	0.24292
mc15_13TeV.364189.Sherpa_221_NNPDF30NNLO_Wtaunu_MAXHTPTV70_140_BFilter.merge.DAOD_HIGG4D1.e5340_s2726_r7772_r7676_p3017	945.6	0.9702	0.10391
mc15_13TeV.364190.Sherpa_221_NNPDF30NNLO_Wtaunu_MAXHTPTV140_280_CVetoBVeto.merge.DAOD_HIGG4D1.e5340_s2726_r7772_r7676_p3017	339.79	0.9702	0.59869
mc15_13TeV.364191.Sherpa_221_NNPDF30NNLO_Wtaunu_MAXHTPTV140_280_CFilterBVeto.merge.DAOD_HIGG4D1.e5340_s2726_r7772_r7676_p3017	339.68	0.9702	0.28465
mc15_13TeV.364192.Sherpa_221_NNPDF30NNLO_Wtaunu_MAXHTPTV140_280_BFilter.merge.DAOD_HIGG4D1.e5340_s2726_r7772_r7676_p3017	339.13	0.9702	0.10247
mc15_13TeV.364193.Sherpa_221_NNPDF30NNLO_Wtaunu_MAXHTPTV280_500_CVetoBVeto.merge.DAOD_HIGG4D1.e5340_s2726_r7772_r7676_p3017	72.085	0.9702	0.54821
mc15_13TeV.364194.Sherpa_221_NNPDF30NNLO_Wtaunu_MAXHTPTV280_500_CFilterBVeto.merge.DAOD_HIGG4D1.e5340_s2726_r7772_r7676_p3017	71.995	0.9702	0.31883
mc15_13TeV.364195.Sherpa_221_NNPDF30NNLO_Wtaunu_MAXHTPTV280_500_BFilter.merge.DAOD_HIGG4D1.e5340_s2726_r7772_r7676_p3017	71.95	0.9702	0.13592
mc15_13TeV.364196.Sherpa_221_NNPDF30NNLO_Wtaunu_MAXHTPTV500_1000.merge.DAOD_HIGG4D1.e5340_s2726_r7772_r7676_p3017	15.051	0.9702	1.0
mc15_13TeV.364197.Sherpa_221_NNPDF30NNLO_Wtaunu_MAXHTPTV1000_E_CMS.merge.DAOD_HIGG4D1.e5340_s2726_r7772_r7676_p3017	1.234	0.9702	1.0
mc15_13TeV.344440.Sherpa_NNPDF30NNLO_Wtaunu2jets_Min_N_TChannel.merge.DAOD_HIGG4D1.e5231_s2726_r7772_r7676_p2949	6.7537	1.0	1.0

A.5 $W \to ee$

Dataset Name	XSec [pb]	K-Factor	Filter Eff.
mc15_13TeV.364170.Sherpa_221_NNPDF30NNLO_Wenu_MAXHTPTV0_70_CVetoBVeto.merge.DAOD_HIGG4D1.e5340_s2726_r7772_r7676_p3017	19152.0	0.9702	0.82467
mc15_13TeV.364171.Sherpa_221_NNPDF30NNLO_Wenu_MAXHTPTV0_70_CFilterBVeto.merge.DAOD_HIGG4D1.e5340_s2726_r7772_r7676_p3017	19146.0	0.9702	0.13087
mc15_13TeV.364172.Sherpa_221_NNPDF30NNLO_Wenu_MAXHTPTV0_70_BFilter.merge.DAOD_HIGG4D1.e5340_s2726_r7772_r7676_p3017	19138.0	0.9702	0.044838
mc15_13TeV.364173.Sherpa_221_NNPDF30NNLO_Wenu_MAXHTPTV70_140_CVetoBVeto.merge.DAOD_HIGG4D1.e5340_s2726_r7772_r7676_p3017	944.67	0.9702	0.67486
mc15_13TeV.364174.Sherpa_221_NNPDF30NNLO_Wenu_MAXHTPTV70_140_CFilterBVeto.merge.DAOD_HIGG4D1.e5340_s2726_r7772_r7676_p3017	945.56	0.9702	0.24378
mc15_13TeV.364175.Sherpa_221_NNPDF30NNLO_Wenu_MAXHTPTV70_140_BFilter.merge.DAOD_HIGG4D1.e5340_s2726_r7772_r7676_p3017	945.74	0.9702	0.10341
mc15_13TeV.364176.Sherpa_221_NNPDF30NNLO_Wenu_MAXHTPTV140_280_CVetoBVeto.merge.DAOD_HIGG4D1.e5340_s2726_r7772_r7676_p3017	339.69	0.9702	0.5988
mc15_13TeV.364177.Sherpa_221_NNPDF30NNLO_Wenu_MAXHTPTV140_280_CFilterBVeto.merge.DAOD_HIGG4D1.e5340_s2726_r7772_r7676_p3017	339.92	0.9702	0.29187
mc15_13TeV.364178.Sherpa_221_NNPDF30NNLO_Wenu_MAXHTPTV140_280_BFilter.merge.DAOD_HIGG4D1.e5340_s2726_r7772_r7676_p3017	339.67	0.9702	0.10898
mc15_13TeV.364179.Sherpa_221_NNPDF30NNLO_Wenu_MAXHTPTV280_500_CVetoBVeto.merge.DAOD_HIGG4D1.e5340_s2726_r7772_r7676_p3017	72.069	0.9702	0.54825
mc15_13TeV.364180.Sherpa_221_NNPDF30NNLO_Wenu_MAXHTPTV280_500_CFilterBVeto.merge.DAOD_HIGG4D1.e5340_s2726_r7772_r7676_p3017	72.112	0.9702	0.31974
mc15_13TeV.364181.Sherpa_221_NNPDF30NNLO_Wenu_MAXHTPTV280_500_BFilter.merge.DAOD_HIGG4D1.e5340_s2726_r7772_r7676_p3017	72.1	0.9702	0.13706
mc15_13TeV.364182.Sherpa_221_NNPDF30NNLO_Wenu_MAXHTPTV500_1000.merge.DAOD_HIGG4D1.e5340_s2726_r7772_r7676_p3017	15.047	0.9702	1.0
mc15_13TeV.364183.Sherpa_221_NNPDF30NNLO_Wenu_MAXHTPTV1000_E_CMS.merge.DAOD_HIGG4D1.e5340_s2726_r7772_r7676_p3017	1.2342	0.9702	1.0
mc15_13TeV.344439.Sherpa_NNPDF30NNLO_Wenu2jets_Min_N_TChannel.merge.DAOD_HIGG4D1.e5237_s2726_r7772_r7676_p2949	6.7548	1.0	1.0

A.6 $W \to \mu\mu$

Dataset Name	XSec [pb]	K-Factor	Filter Eff.
mc15_13TeV.364156.Sherpa_221_NNPDF30NNLO_Wmunu_MAXHTPTV0_70_CVetoBVeto.merge.DAOD_HIGG4D1.e5340_s2726_r7772_r7676_p3017	19151.0	0.9702	0.8244
mc15_13TeV.364157.Sherpa_221_NNPDF30NNLO_Wmunu_MAXHTPTV0_70_CFilterBVeto.merge.DAOD_HIGG4D1.e5340_s2726_r7772_r7676_p3017	19142.0	0.9702	0.13088
mc15_13TeV.364158.Sherpa_221_NNPDF30NNLO_Wmunu_MAXHTPTV0_70_BFilter.merge.DAOD_HIGG4D1.e5340_s2726_r7772_r7676_p3017	19141.0	0.9702	0.044587
mc15_13TeV.364159.Sherpa_221_NNPDF30NNLO_Wmunu_MAXHTPTV70_140_CVetoBVeto.merge.DAOD_HIGG4D1.e5340_s2726_r7772_r7676_p3017	945.52	0.9702	0.672
mc15_13TeV.364160.Sherpa_221_NNPDF30NNLO_Wmunu_MAXHTPTV70_140_CFilterBVeto.merge.DAOD_HIGG4D1.e5340_s2726_r7772_r7676_p3017	945.52	0.9702	0.24592
mc15_13TeV.364161.Sherpa_221_NNPDF30NNLO_Wmunu_MAXHTPTV70_140_BFilter.merge.DAOD_HIGG4D1.e5340_s2726_r7772_r7676_p3017	944.66	0.9702	0.083022
mc15_13TeV.364162.Sherpa_221_NNPDF30NNLO_Wmunu_MAXHTPTV140_280_CVetoBVeto.merge.DAOD_HIGG4D1.e5340_s2726_r7772_r7676_p3017	339.77	0.9702	0.6028
mc15_13TeV.364163.Sherpa_221_NNPDF30NNLO_Wmunu_MAXHTPTV140_280_CFilterBVeto.merge.DAOD_HIGG4D1.e5340_s2726_r7772_r7676_p3017	339.8	0.9702	0.29188
mc15_13TeV.364164.Sherpa_221_NNPDF30NNLO_Wmunu_MAXHTPTV140_280_BFilter.merge.DAOD_HIGG4D1.e5340_s2726_r7772_r7676_p3017	339.66	0.9702	0.110298
mc15_13TeV.364165.Sherpa_221_NNPDF30NNLO_Wmunu_MAXHTPTV280_500_CVetoBVeto.merge.DAOD_HIGG4D1.e5340_s2726_r7772_r7676_p3017	72.072	0.9702	0.54755
mc15_13TeV.364166.Sherpa_221_NNPDF30NNLO_Wmunu_MAXHTPTV280_500_CFilterBVeto.merge.DAOD_HIGG4D1.e5340_s2726_r7772_r7676_p3017	72.093	0.9702	0.32013
mc15_13TeV.364167.Sherpa_221_NNPDF30NNLO_Wmunu_MAXHTPTV280_500_BFilter.merge.DAOD_HIGG4D1.e5340_s2726_r7772_r7676_p3017	72.057	0.9702	0.12405
mc15_13TeV.364168.Sherpa_221_NNPDF30NNLO_Wmunu_MAXHTPTV500_1000.merge.DAOD_HIGG4D1.e5340_s2726_r7772_r7676_p3017	15.007	0.9702	1.0
mc15_13TeV.364169.Sherpa_221_NNPDF30NNLO_Wmunu_MAXHTPTV1000_E_CMS.merge.DAOD_HIGG4D1.e5340_s2726_r7772_r7676_p3017	1.2349	0.9702	1.0
mc15_13TeV.344438.Sherpa_NNPDF30NNLO_Wmunu2jets_Min_N_TChannel.merge.DAOD_HIGG4D1.e5231_s2726_r7772_r7676_p2949	6.7448	1.0	1.0

A.7 $t\bar{t}$ and single top

Dataset Name	XSec [pb]	K-Factor	Filter Eff.
mc15_13TeV.410000.PowhegPythiaEvtGen_P2012_ttbar_hdamp172p5_nonallhad.merge.DAOD_HIGG4D1.e3698_s2608_s2183_r7725_r7676_p2949	696.11	1.195	0.5442
mc15_13TeV.410007.PowhegPythiaEvtGen_P2012_ttbar_hdamp172p5_allhad.merge.DAOD_HIGG4D1.e4135_s2608_s2183_r7725_r7676_p2949	696.21	1.195	0.457
mc15_13TeV.410011.PowhegPythiaEvtGen_P2012_singletop_tchan_lept_top.merge.DAOD_HIGG4D1.e3824_s2608_s2183_r7725_r7676_p2949	43.739	1.0094	1.0
mc15_13TeV.410012.PowhegPythiaEvtGen_P2012_singletop_tchan_lept_antitop.merge.DAOD_HIGG4D1.e3824_s2608_s2183_r7725_r7676_p2949	25.778	1.0193	1.0
mc15_13TeV.410013.PowhegPythiaEvtGen_P2012_Wt_inclusive_top.merge.DAOD_HIGG4D1.e3753_s2608_s2183_r7725_r7676_p2949	34.009	1.054	1.0
mc15_13TeV.410014.PowhegPythiaEvtGen_P2012_Wt_inclusive_antitop.merge.DAOD_HIGG4D1.e3753_s2608_s2183_r7725_r7676_p2949	33.989	1.054	1.0
mc15_13TeV.410025.PowhegPythiaEvtGen_P2012_SingleTopSchan_noAllHad_top.merge.DAOD_HIGG4D1.e3998_s2608_s2183_r7725_r7676_p2949	2.0514	1.0048	1.0
mc15_13TeV.410026.PowhegPythiaEvtGen_P2012_SingleTopSchan_noAllHad_antitop.merge.DAOD_HIGG4D1.e3998_s2608_s2183_r7725_r7676_p2949	1.2615	1.0215	1.0

A.8 Diboson

Dataset Name	XSec [pb]	K-Factor	Filter Eff.
mc15_13TeV.363490.Sherpa_221_NNPDF30NNLO_llll.merge.DAOD_HIGG4D1.e5332_s2726_r7772_r7676_p3228	1.2561	1.0	1.0
mc15_13TeV.363356.Sherpa_221_NNPDF30NNLO_ZqqZll.merge.DAOD_HIGG4D1.e5525_s2726_r7772_r7676_p3228	15.561	1.0	0.14089
mc15_13TeV.363355.Sherpa_221_NNPDF30NNLO_ZqqZvv.merge.DAOD_HIGG4D1.e5525_s2726_r7772_r7676_p3228	15.567	1.0	0.27978
mc15_13TeV.361068.Sherpa_CT10_llvv.merge.DAOD_HIGG4D1.e3836_s2608_s2183_r7725_r7676_p2949	13.998	0.91	1.0
mc15_13TeV.363494.Sherpa_221_NNPDF30NNLO_vvvv.merge.DAOD_HIGG4D1.e5332_s2726_r7772_r7676_p3228	0.60368	1.0	1.0
mc15_13TeV.361091.Sherpa_CT10_WplvWmqq_SHv21_improved.merge.DAOD_HIGG4D1.e4607_s2726_r7772_r7676_p2949	24.893	0.91	1.0
mc15_13TeV.363359.Sherpa_221_NNPDF30NNLO_WpqqWmlv.merge.DAOD_HIGG4D1.e5583_s2726_r7772_r7676_p3228	24.71	1.0	1.0
mc15_13TeV.363358.Sherpa_221_NNPDF30NNLO_WqqZll.merge.DAOD_HIGG4D1.e5525_s2726_r7772_r7676_p3228	3.433	1.0	1.0
mc15_13TeV.363357.Sherpa_221_NNPDF30NNLO_WqqZvv.merge.DAOD_HIGG4D1.e5525_s2726_r7772_r7676_p3228	6.7874	1.0	1.0
mc15_13TeV.363489.Sherpa_221_NNPDF30NNLO_WlvZqq.merge.DAOD_HIGG4D1.e5525_s2726_r7772_r7676_p3228	11.42	1.0	1.0
mc15_13TeV.363491.Sherpa_221_NNPDF30NNLO_lllv.merge.DAOD_HIGG4D1.e5332_s2726_r7772_r7676_p3228	4.5877	1.0	1.0
mc15_13TeV.363493.Sherpa_221_NNPDF30NNLO_lvvv.merge.DAOD_HIGG4D1.e5332_s2726_r7772_r7676_p3228	3.2286	1.0	1.0

A.9 $H_{125} \rightarrow \tau\tau$

The cross-section for these samples is not taken from [72] as there are mistakes in the calculations for the $H \rightarrow \tau\tau$ samples. Instead the cross-section was taken from the ATLAS analysis for the $H_{125} \rightarrow \tau\tau$ process [68].

Dataset Name	XSec [pb]	K-Factor	Filter Eff.
mc15_13TeV.343365.aMcAtNloPythia8EvtGen_A14_NNPDF23_NNPDF30ME_ttH125_dilep.merge.DAOD_HIGG4D1.e4706_s2726_r7772_r7676_p2949	0.05343	1.0	1.0
mc15_13TeV.343366.aMcAtNloPythia8EvtGen_A14_NNPDF23_NNPDF30ME_ttH125_semilep.merge.DAOD_HIGG4D1.e4706_s2726_r7772_r7676_p2949	0.22276	1.0	0.43817
mc15_13TeV.343367.aMcAtNloPythia8EvtGen_A14_NNPDF23_NNPDF30ME_ttH125_allhad.merge.DAOD_HIGG4D1.e4706_s2726_r7772_r7676_p2949	0.230832	1.0	0.45649
mc15_13TeV.345073.PowhegPy8EG_NNPDF30_AZNLOCTEQ6L1_VBFH125_tautaul13l7.merge.DAOD_HIGG4D1.e5822_s2726_r7772_r7676_p3228	0.23721	1.0	0.057926
mc15_13TeV.345074.PowhegPy8EG_NNPDF30_AZNLOCTEQ6L1_VBFH125_tautaulm15hp20.merge.DAOD_HIGG4D1.e5822_s2726_r7772_r7676_p3228	0.23721	1.0	0.040337
mc15_13TeV.345075.PowhegPy8EG_NNPDF30_AZNLOCTEQ6L1_VBFH125_tautaulp15hm20.merge.DAOD_HIGG4D1.e5822_s2726_r7772_r7676_p3228	0.23721	1.0	0.040323
mc15_13TeV.345076.PowhegPy8EG_NNPDF30_AZNLOCTEQ6L1_VBFH125_tautauh30h20.merge.DAOD_HIGG4D1.e5822_s2726_r7772_r7676_p3228	0.23721	1.0	0.19829
mc15_13TeV.345120.PowhegPy8EG_NNLOPS_nnlo_30_ggH125_tautaul13l7.merge.DAOD_HIGG4D1.e5814_s2726_r7772_r7676_p3228	3.0469	1.0	0.053756
mc15_13TeV.345121.PowhegPy8EG_NNLOPS_nnlo_30_ggH125_tautaulm15hp20.merge.DAOD_HIGG4D1.e5814_s2726_r7772_r7676_p3228	3.0469	1.0	0.037749
mc15_13TeV.345122.PowhegPy8EG_NNLOPS_nnlo_30_ggH125_tautaulp15hm20.merge.DAOD_HIGG4D1.e5814_s2726_r7772_r7676_p3228	3.0469	1.0	0.037826
mc15_13TeV.345123.PowhegPy8EG_NNLOPS_nnlo_30_ggH125_tautauh30h20.merge.DAOD_HIGG4D1.e5814_s2726_r7772_r7676_p3228	3.0469	1.0	0.1889
mc15_13TeV.345211.PowhegPy8EG_NNPDF30_AZNLO_WmH125J_Winc_MINLO_tautau.merge.DAOD_HIGG4D1.e5808_s2726_r7772_r7676_p3228	0.033147	1.0	1.0
mc15_13TeV.345212.PowhegPy8EG_NNPDF30_AZNLO_WpH125J_Winc_MINLO_tautau.merge.DAOD_HIGG4D1.e5808_s2726_r7772_r7676_p3228	0.052685	1.0	1.0
mc15_13TeV.345217.PowhegPy8EG_NNPDF30_AZNLO_ZH125J_Zinc_MINLO_tautau.merge.DAOD_HIGG4D1.e5808_s2726_r7772_r7676_p3228	0.055438	1.0	1.0

A.10 QCD

Dataset Name	XSec [pb]	K-Factor	Filter Eff.
mc15_13TeV.361020.Pythia8EvtGen_A14NNPDF23LO_jetjet_JZ0W.merge.DAOD_HIGG4D1.e3569_s2576_s2132_r7773_r7676_p3017	78420000000.0	1.0	0.9755
mc15_13TeV.361021.Pythia8EvtGen_A14NNPDF23LO_jetjet_JZ1W.merge.DAOD_HIGG4D1.e3569_s2576_s2132_r7773_r7676_p3017	78420000000.0	1.0	0.00067143
mc15_13TeV.361022.Pythia8EvtGen_A14NNPDF23LO_jetjet_JZ2W.merge.DAOD_HIGG4D1.e3668_s2576_s2132_r7773_r7676_p3017	2433200000.0	1.0	0.00033423
mc15_13TeV.361023.Pythia8EvtGen_A14NNPDF23LO_jetjet_JZ3W.merge.DAOD_HIGG4D1.e3668_s2576_s2132_r7773_r7676_p3017	26454000.0	1.0	0.00032016
mc15_13TeV.361024.Pythia8EvtGen_A14NNPDF23LO_jetjet_JZ4W.merge.DAOD_HIGG4D1.e3668_s2576_s2132_r7773_r7676_p3017	254630.0	1.0	0.00053138
mc15_13TeV.361025.Pythia8EvtGen_A14NNPDF23LO_jetjet_JZ5W.merge.DAOD_HIGG4D1.e3668_s2576_s2132_r7773_r7676_p3017	4553.5	1.0	0.00092409
mc15_13TeV.361026.Pythia8EvtGen_A14NNPDF23LO_jetjet_JZ6W.merge.DAOD_HIGG4D1.e3569_s2608_s2183_r7773_r7676_p3017	257.53	1.0	0.00094242
mc15_13TeV.361027.Pythia8EvtGen_A14NNPDF23LO_jetjet_JZ7W.merge.DAOD_HIGG4D1.e3668_s2608_s2183_r7773_r7676_p3017	16.215	1.0	0.0003928
mc15_13TeV.361028.Pythia8EvtGen_A14NNPDF23LO_jetjet_JZ8W.merge.DAOD_HIGG4D1.e3569_s2576_s2132_r7773_r7676_p3017	0.62503	1.0	0.010176
mc15_13TeV.361029.Pythia8EvtGen_A14NNPDF23LO_jetjet_JZ9W.merge.DAOD_HIGG4D1.e3569_s2576_s2132_r7773_r7676_p3017	0.019639	1.0	0.012076
mc15_13TeV.361030.Pythia8EvtGen_A14NNPDF23LO_jetjet_JZ10W.merge.DAOD_HIGG4D1.e3569_s2576_s2132_r7773_r7676_p3017	$1.962 \cdot 10^{-3}$	1.0	0.0059087
mc15_13TeV.361031.Pythia8EvtGen_A14NNPDF23LO_jetjet_JZ11W.merge.DAOD_HIGG4D1.e3569_s2608_s2183_r7773_r7676_p3017	$4.23 \cdot 10^{-5}$	1.0	0.0026761
mc15_13TeV.361032.Pythia8EvtGen_A14NNPDF23LO_jetjet_JZ12W.merge.DAOD_HIGG4D1.e3668_s2608_s2183_r7773_r7676_p3017	$1.0 \cdot 10^{-6}$	1.0	0.00042592

A.11 $A \rightarrow \tau\tau$

This section contains the signal MC samples. The cross-section is not given because it is dependent on the coupling to up-type quarks as it was shown in section 4.2.2. The K-Factors and filter efficiencies were also shown in this section.

| Dataset Name |
|---|
| mc15_13TeV.346025.Pythia8EvtGen_A14NNPDF23LO_ggA60_tautau_leplep.merge.AOD.e6774_a766_a821_r7676 |
| mc15_13TeV.346026.Pythia8EvtGen_A14NNPDF23LO_ggA70_tautau_leplep.merge.AOD.e6774_a766_a821_r7676 |
| mc15_13TeV.346027.Pythia8EvtGen_A14NNPDF23LO_ggA80_tautau_leplep.merge.AOD.e6774_a766_a821_r7676 |
| mc15_13TeV.346028.Pythia8EvtGen_A14NNPDF23LO_ggA90_tautau_leplep.merge.AOD.e6774_a766_a821_r7676 |

B Additional plots

B.1 Mass distributions
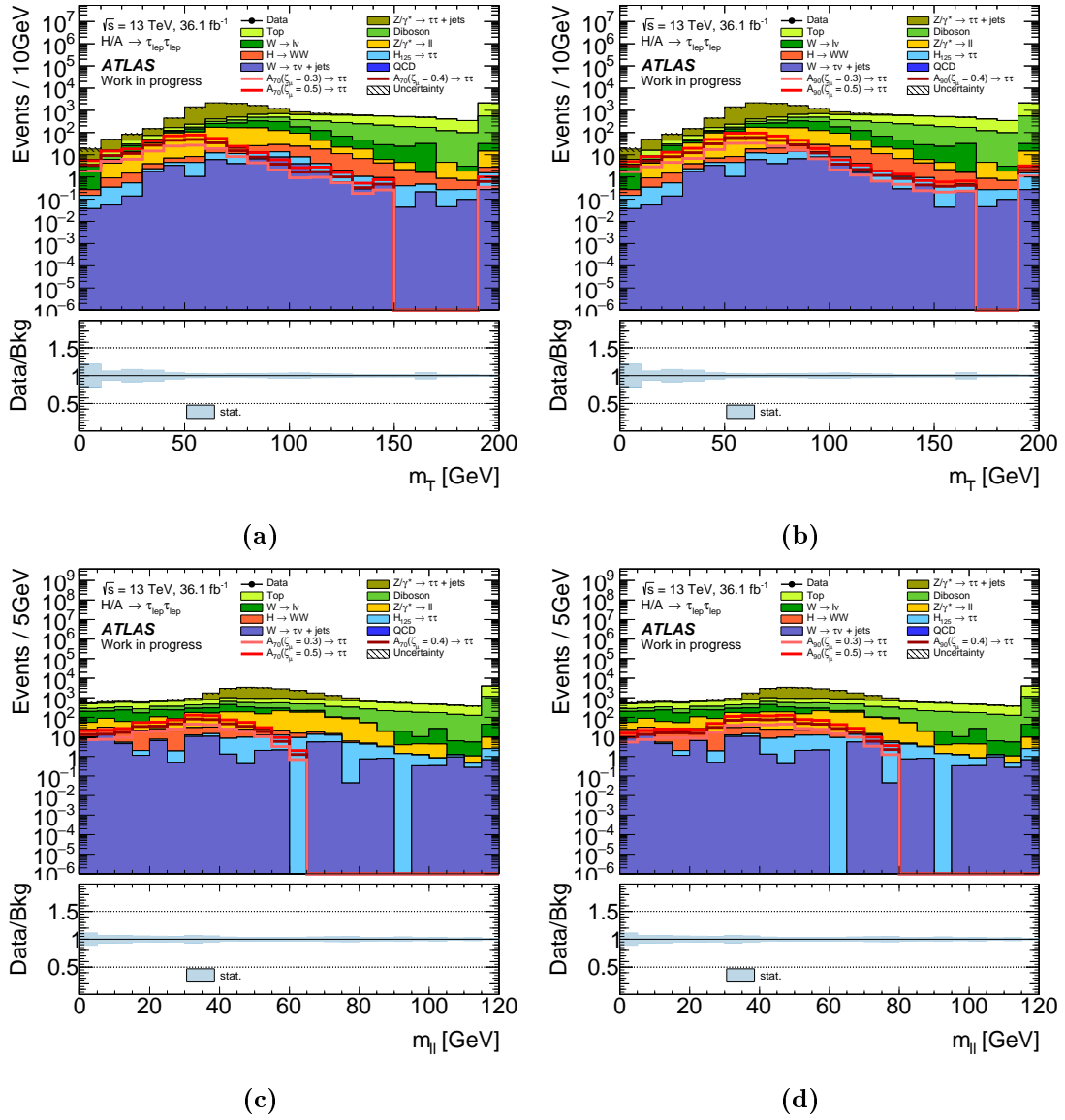
Figure B.1: Mass distributions of the total transverse mass and the dilepton mass for an A boson with a mass of 70 GeV (left) and 90 GeV (right)
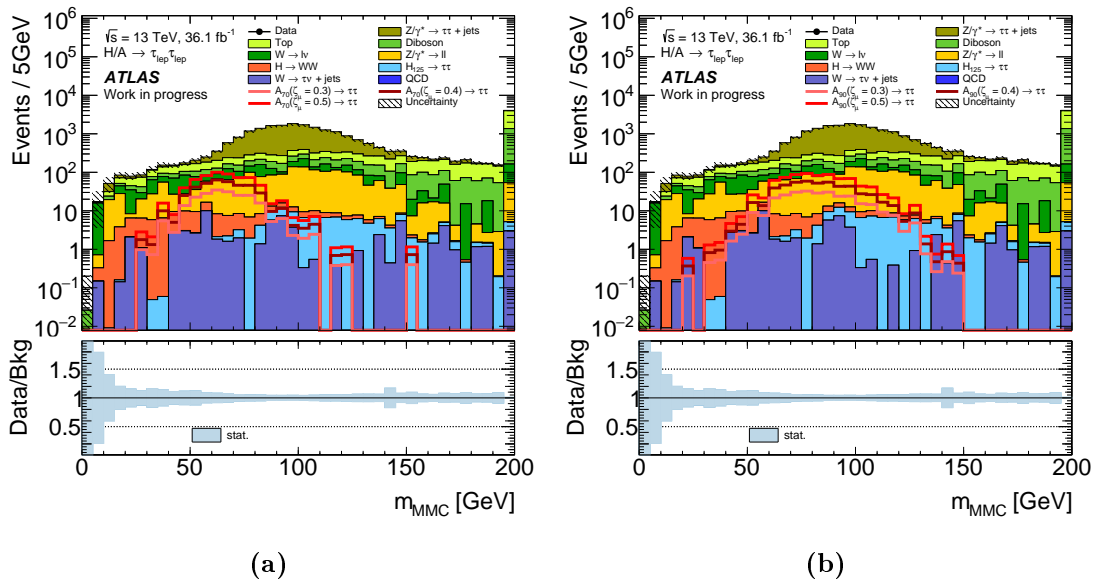
(a)   (b)

Figure B.2: Mass calculated through the missing mass calculator for an A boson with a mass of 70 GeV (left) and 90 GeV (right)
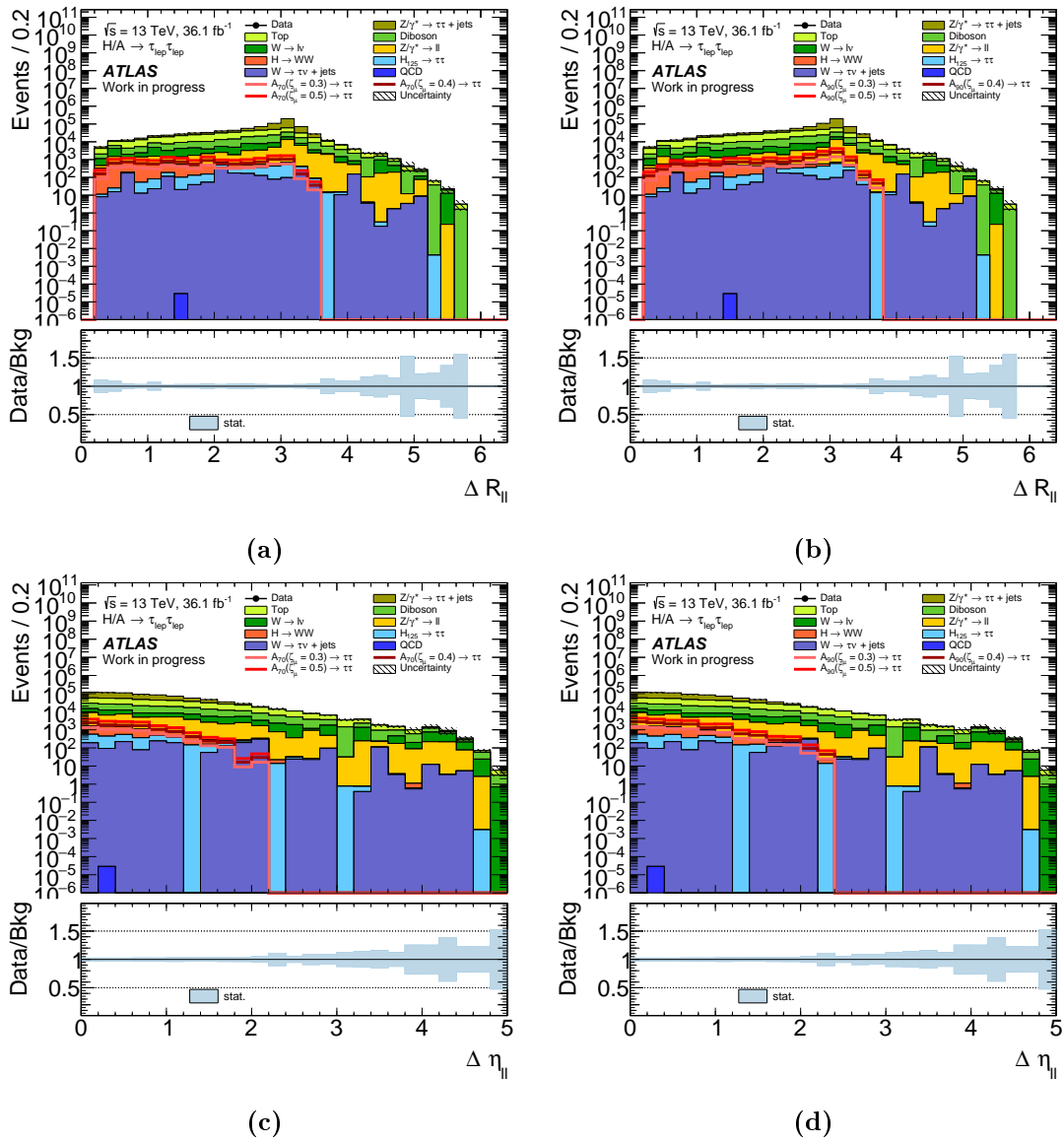
B.2 Angular Distributions

(a)

(b)

(c)

(d)

Figure B.3: Distributions of ΔR and $\Delta \eta$ between the two leptons for an A boson with a mass of 70 GeV (left) and 90 GeV (right)

B.3 $Z \rightarrow \tau\tau$ Control Region

(a)

(b)

(c)

(d)
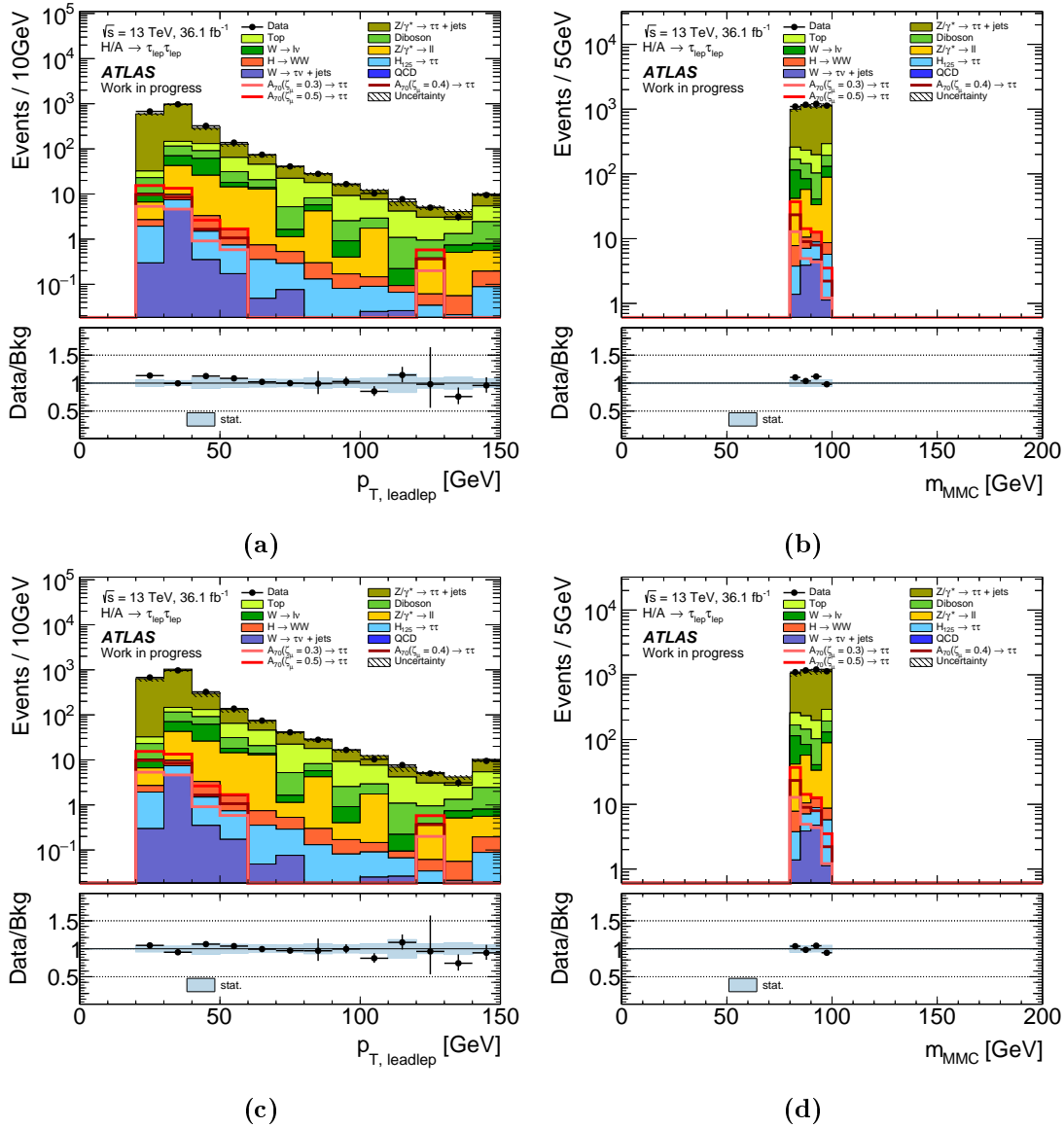
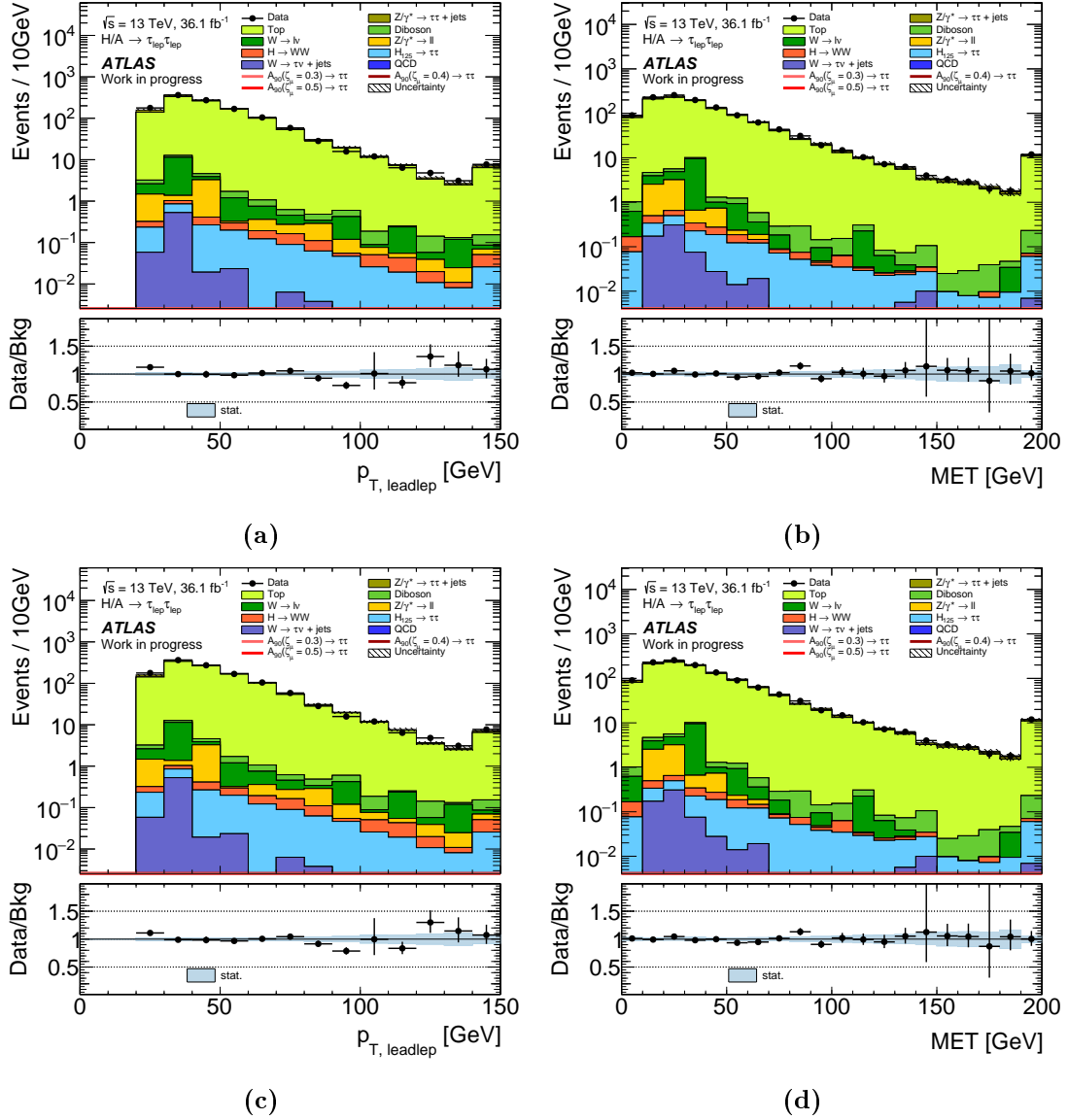**Figure B.4:** $Z \rightarrow \tau\tau$ control region plots for the analysis of a Higgs Boson with a mass of $70\,\mathrm{GeV}$ without (top) and with (bottom) the scale factor of 1.073. (a),(c) p_T of the leading lepton (b),(d) mass from the missing mass calculator
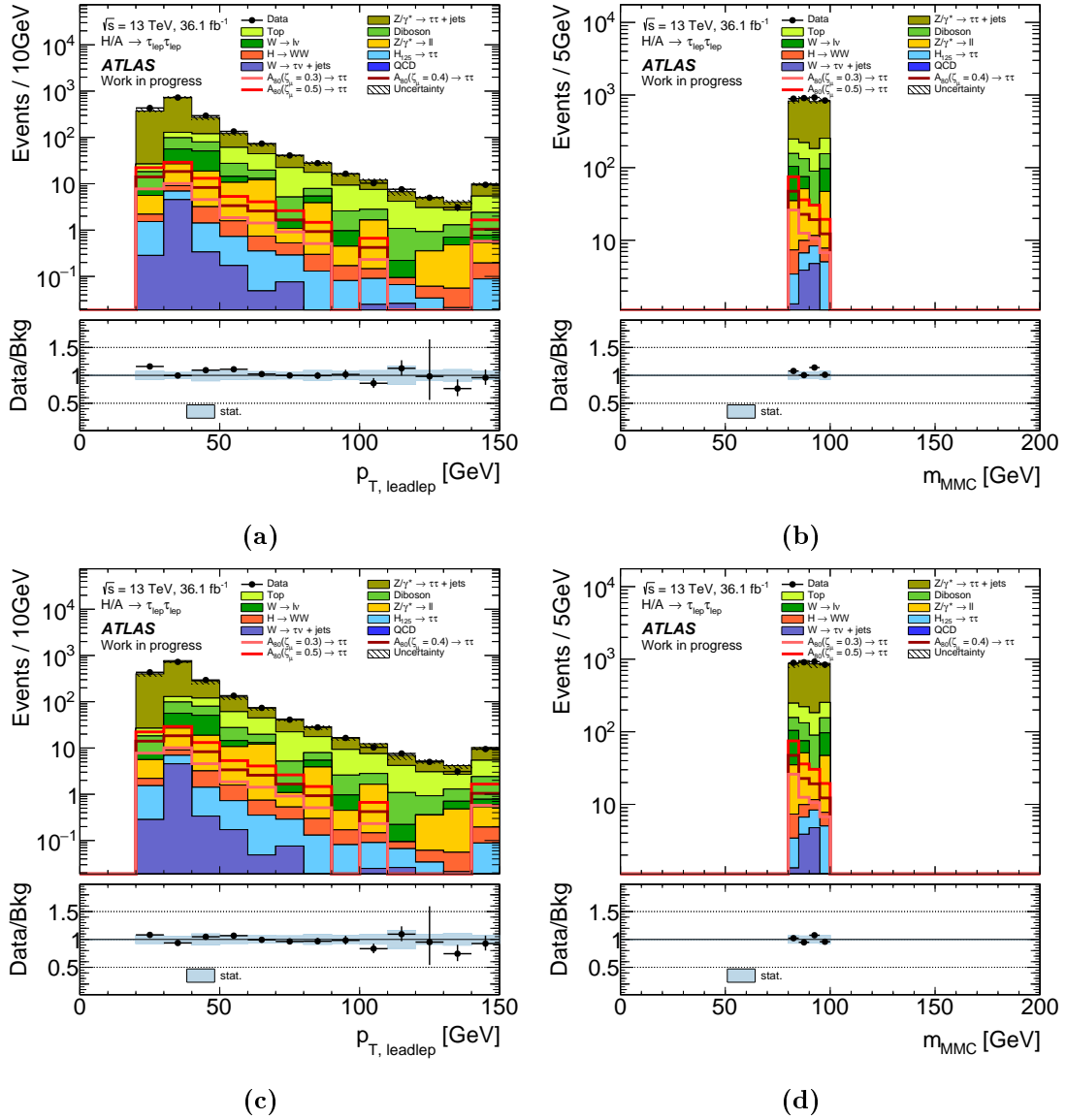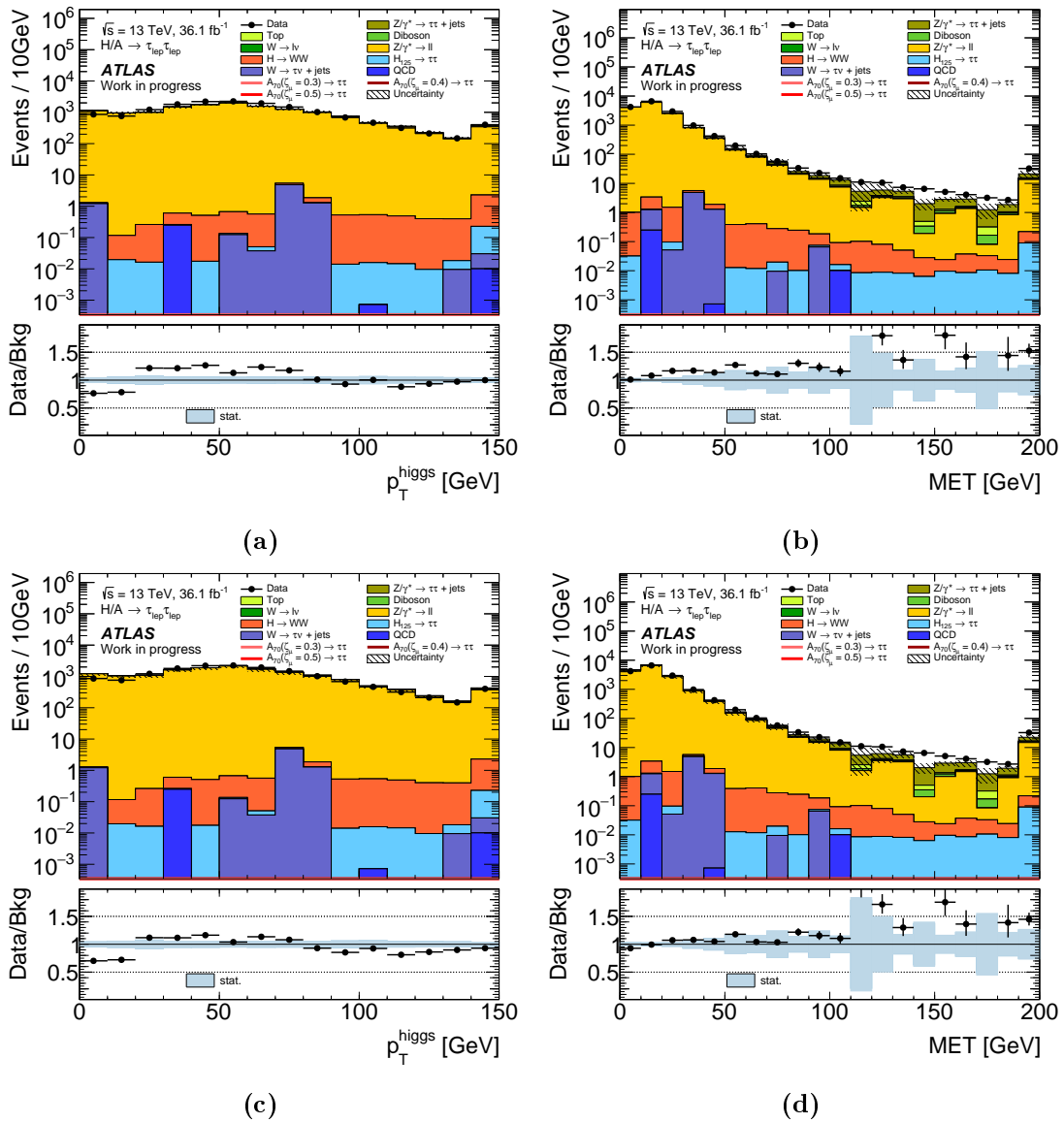
Figure B.5: $Z \to \tau\tau$ control region plots for the analysis of a Higgs Boson with a mass of $80\,\mathrm{GeV}$ without (top) and with (bottom) the scale factor of 1.078. (a),(c) p_T of the leading lepton (b),(d) mass from the missing mass calculator
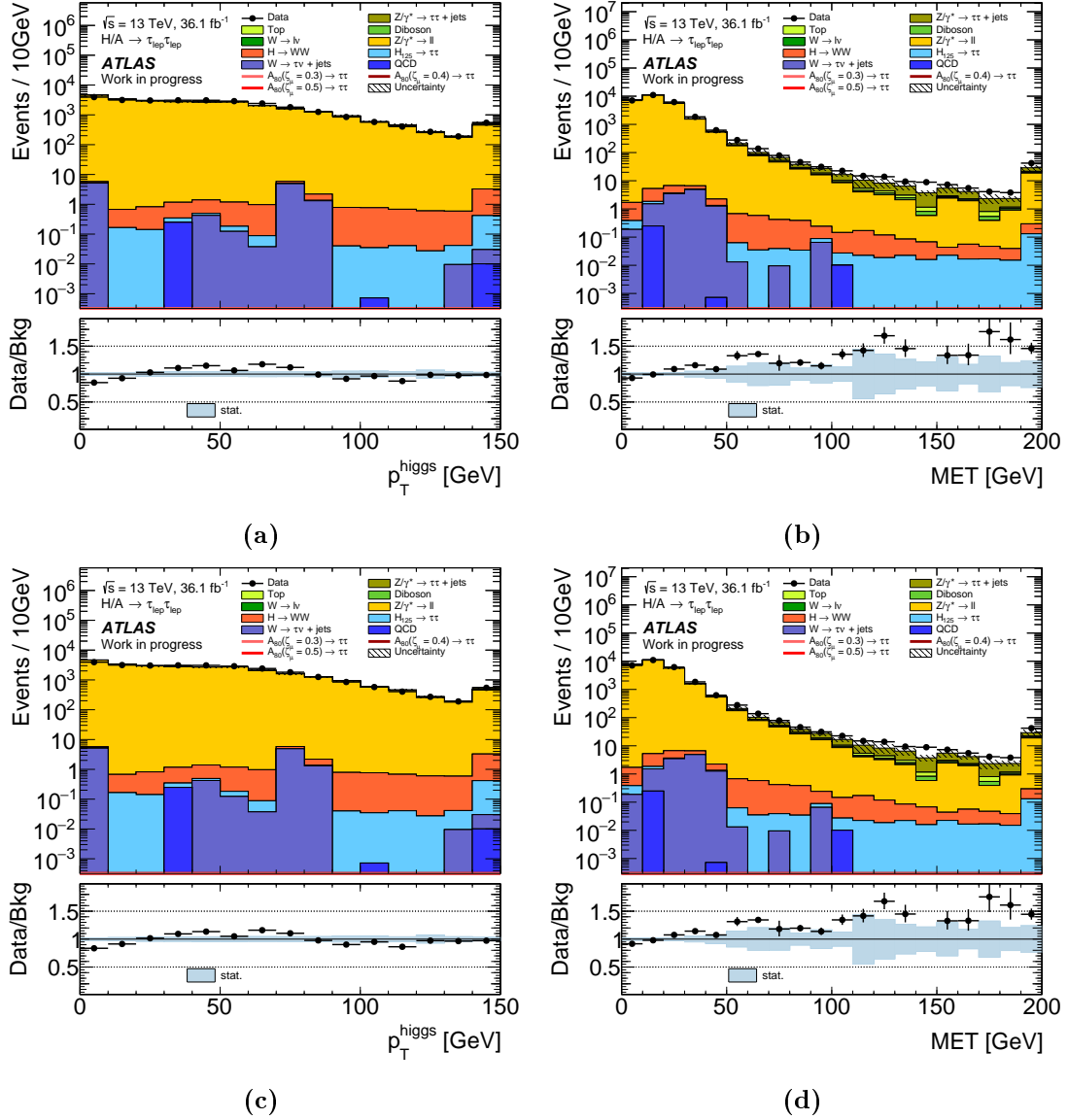
(a)

(b)

(c)

(d)
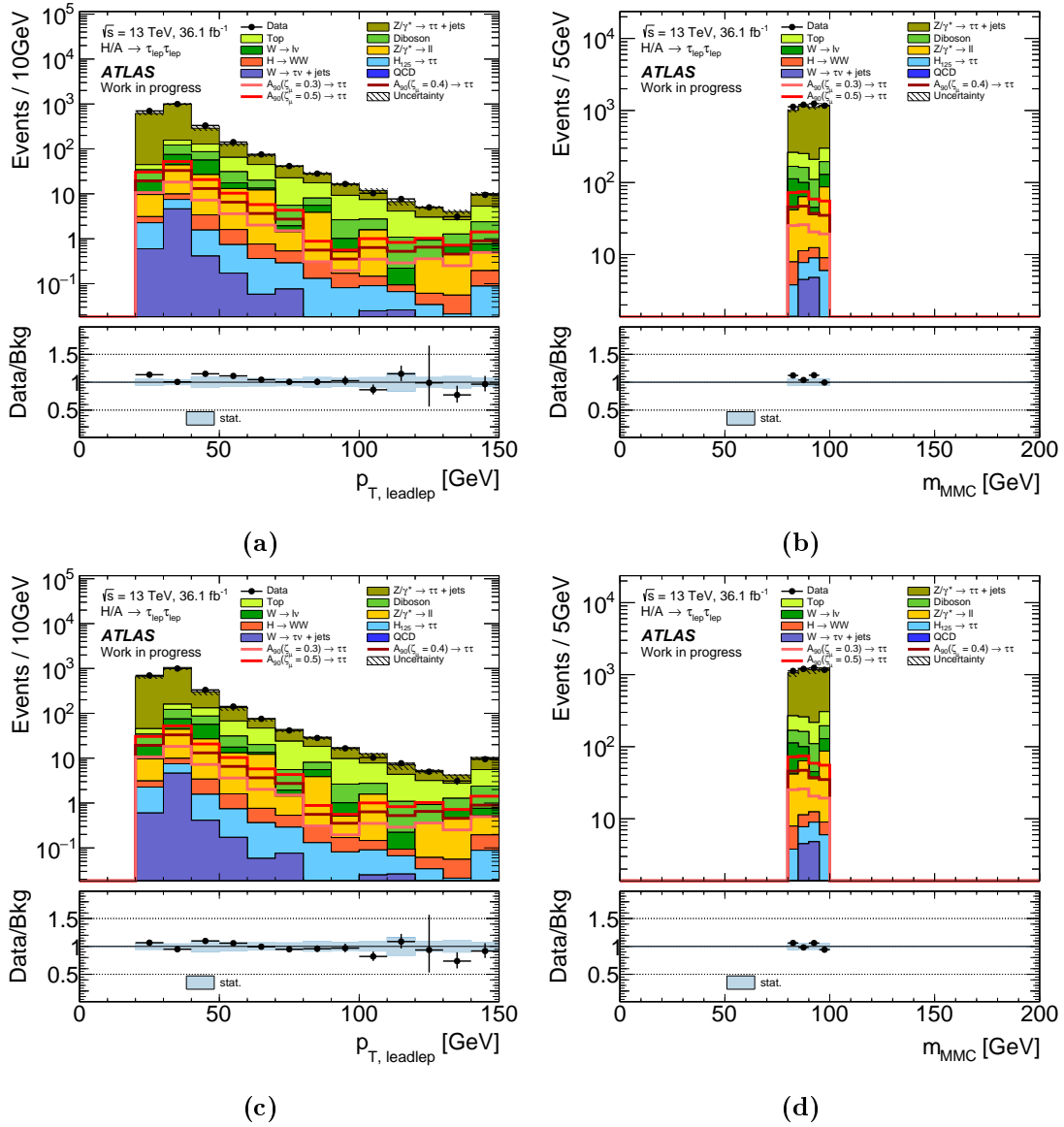
Figure B.6: $Z \to \tau\tau$ control region plots for the analysis of a Higgs Boson with a mass of 90 GeV without (top) and with (bottom) the scale factor of 1.068. (a),(c) p_T of the leading lepton (b),(d) mass from the missing mass calculator

B.4 Top Control Region

(a)

(b)

(c)

(d)
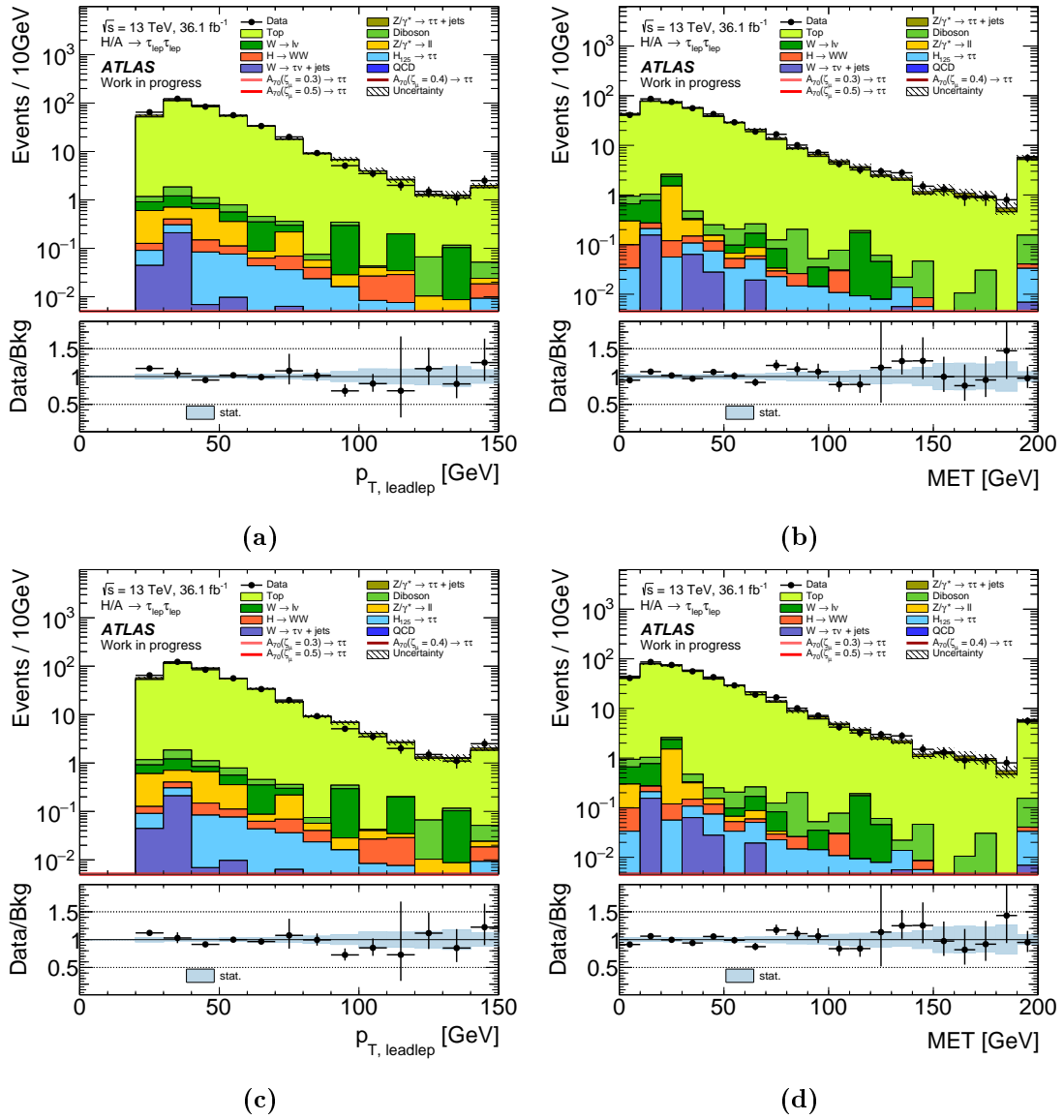
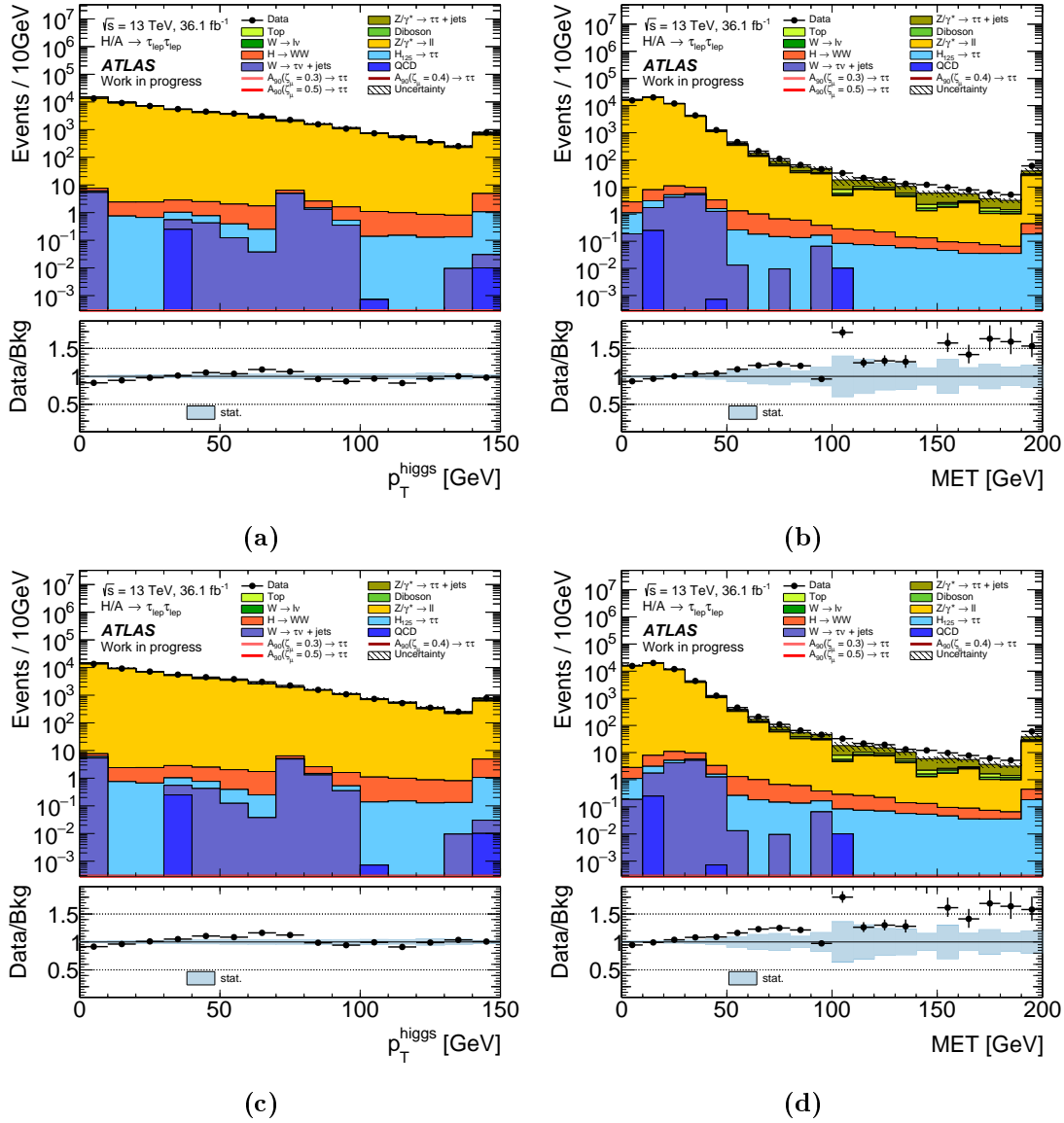**Figure B.7:** Top control region plots for the analysis of a Higgs Boson with a mass of 70 GeV without (top) and with (bottom) the scale factor of 1.025. (a),(c) p_T of the leading lepton (b),(d) missing transverse energy

(a)   **(b)**

(c)   **(d)**
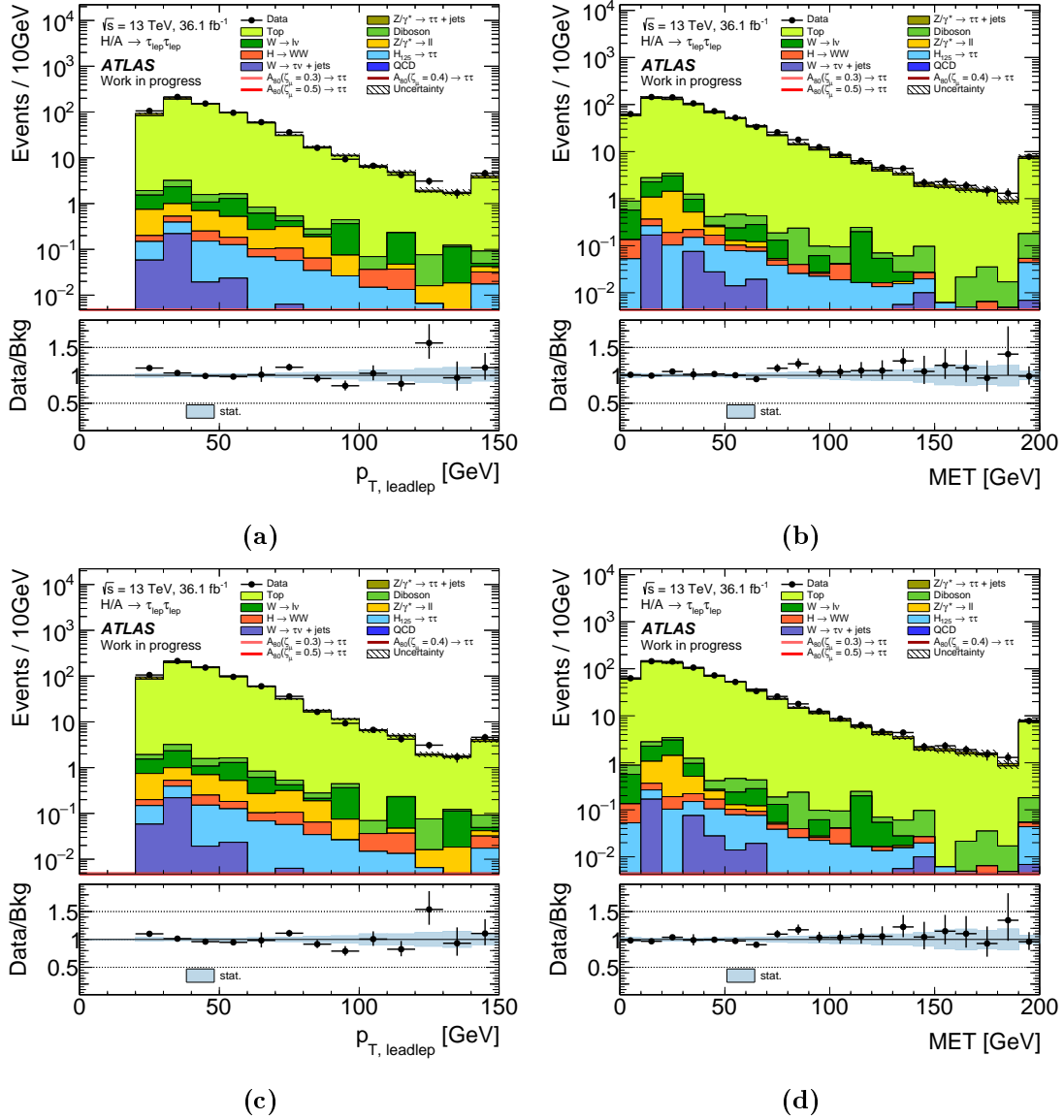
Figure B.8: Top control region plots for the analysis of a Higgs Boson with a mass of 80 GeV without (top) and with (bottom) the scale factor of 1.032. (a),(c) p_T of the leading lepton (b),(d) missing transverse energy

Figure B.9: Top control region plots for the analysis of a Higgs Boson with a mass of 90 GeV without (top) and with (bottom) the scale factor of 1.088.(a),(c) p_T of the leading lepton (b),(d) missing transverse energy

B.5 $Z \rightarrow ll$ Control Region

(a)

(b)

(c)

(d)

Figure B.10: $Z \rightarrow ll$ control region plots for the analysis of a Higgs Boson with a mass of 70 GeV without (top) and with (bottom) the scale factor of 1.089. (a),(c) p_T of the mother particle (b),(d) missing transverse energy

Figure B.11: $Z \to ll$ control region plots for the analysis of a Higgs Boson with a mass of 80 GeV without (top) and with (bottom) the scale factor of 1.014. (a),(c) p_T of the mother particle (b),(d) missing transverse energy

(a)

(b)

(c)

(d)

Figure B.12: $Z \to ll$ control region plots for the analysis of a Higgs Boson with a mass of 90 GeV without (top) and with (bottom) the scale factor of 0.966. (a),(c) p_T of the mother particle (b),(d) missing transverse energy

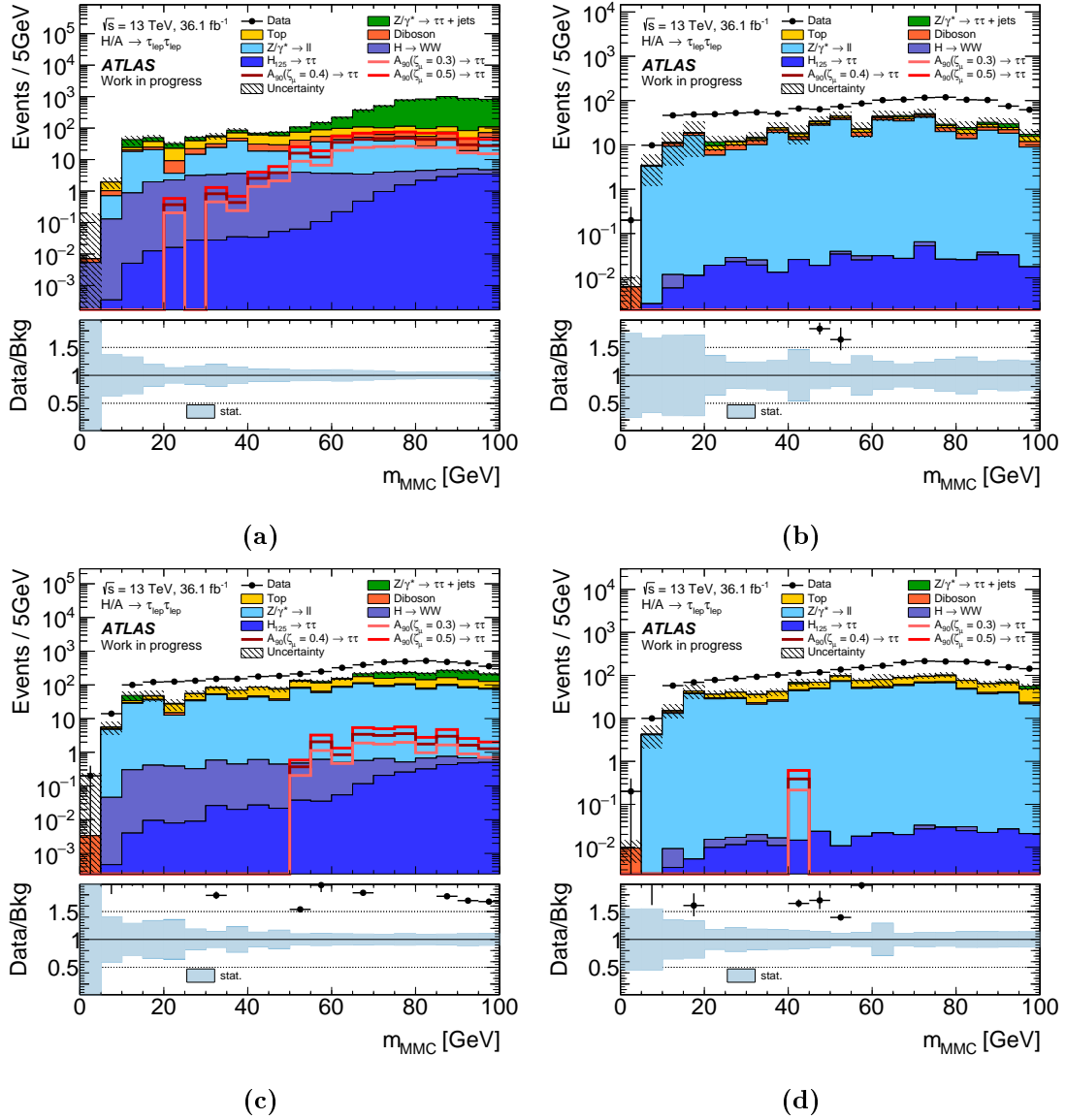## B.6 Fake Control Regions

(a)

(b)

(c)

(d)
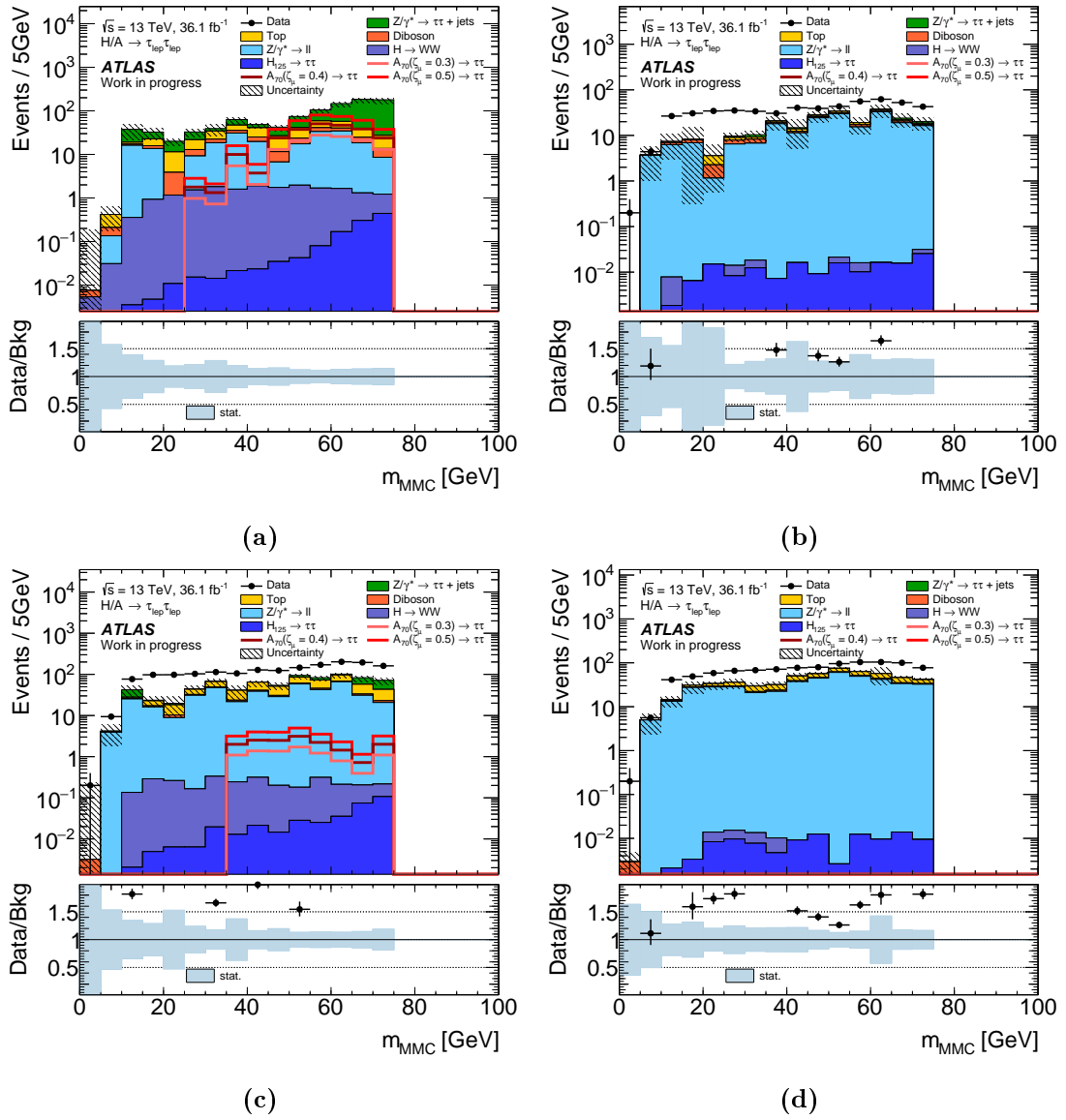
Figure B.13: Mass from the missing mass calculator in the four different regions for a Higgs boson with a mass of 70 GeV (a) signal region A (b) same-sign region B (c) fake region C (d) fake same-sign region D
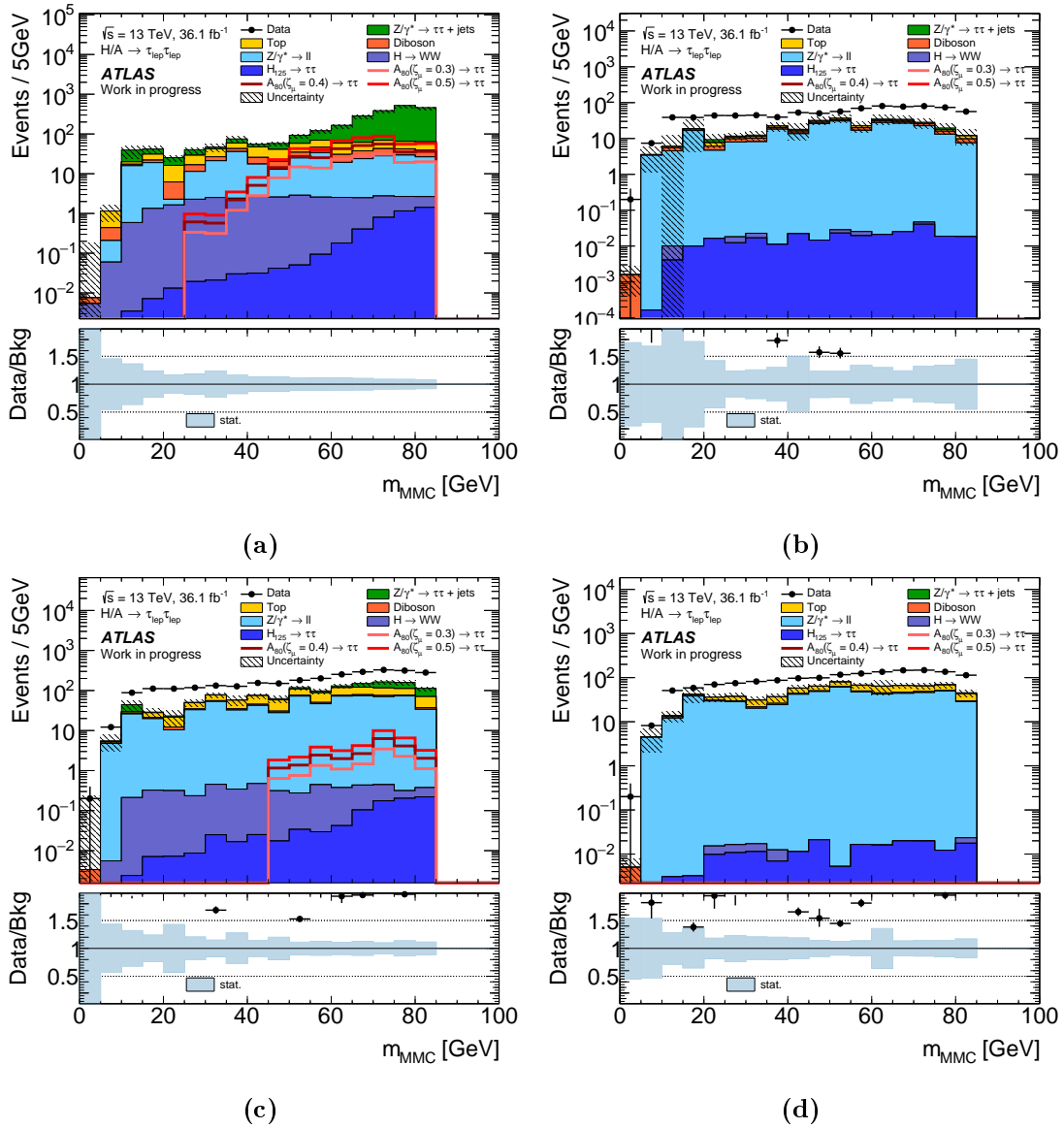
Figure B.14: Mass from the missing mass calculator in the four different regions for a Higgs boson with a mass of 80 GeV (a) signal region A (b) same-sign region B (c) fake region C (d) fake same-sign region D

Figure B.15: Mass from the missing mass calculator in the four different regions for a Higgs boson with a mass of 90 GeV (a) signal region A (b) same-sign region B (c) fake region C (d) fake same-sign region D

(a)   **(b)**
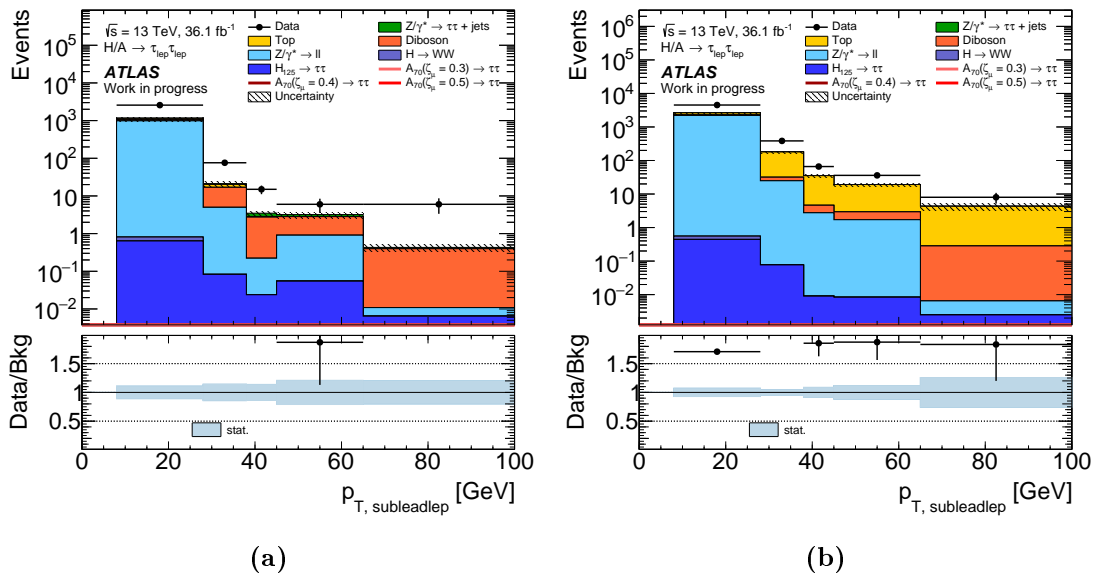
Figure B.16: p_T of the subleading lepton for 70 GeV Higgs Boson in the (a) same-sign control region (b) fake same-sign control region

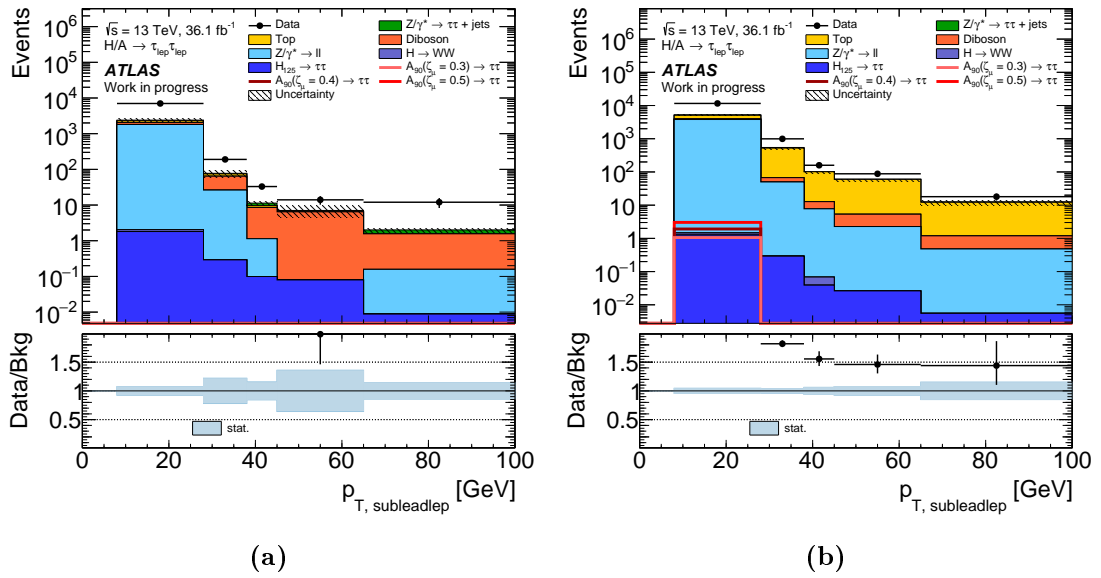**(a)**   **(b)**
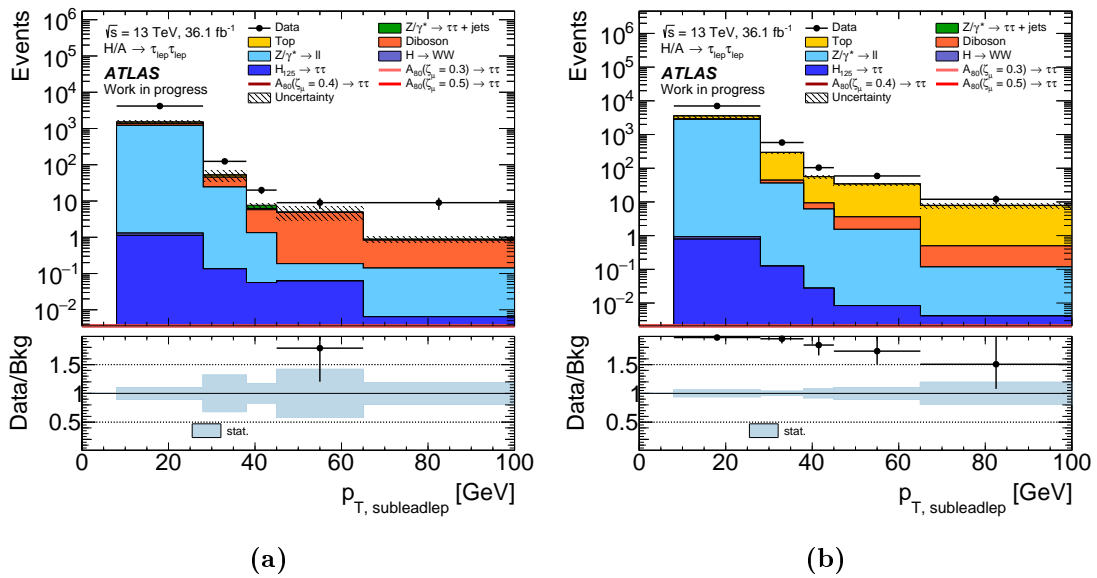
Figure B.17: p_T of the subleading lepton for a 80 GeV Higgs Boson in the (a) same-sign control region (b) fake same-sign control region

Figure B.18: p_T of the subleading lepton for a 90 GeV Higgs Boson in the (a) same-sign control region (b) fake same-sign control region
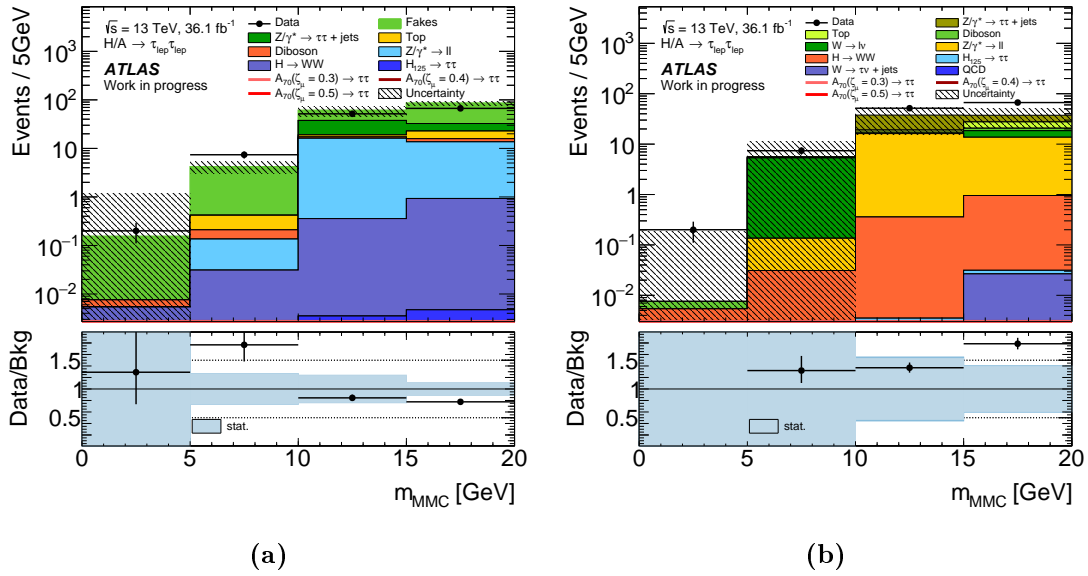
B.7 Testing the fake estimation

(a)   (b)

Figure B.19: Mass distribution from the missing mass calculator in the region $0\,\text{GeV} < m_{MMC} < 20\,\text{GeV}$ for a $70\,\text{GeV}$ Higgs boson (a) with fake estimation (b) without fake estimation
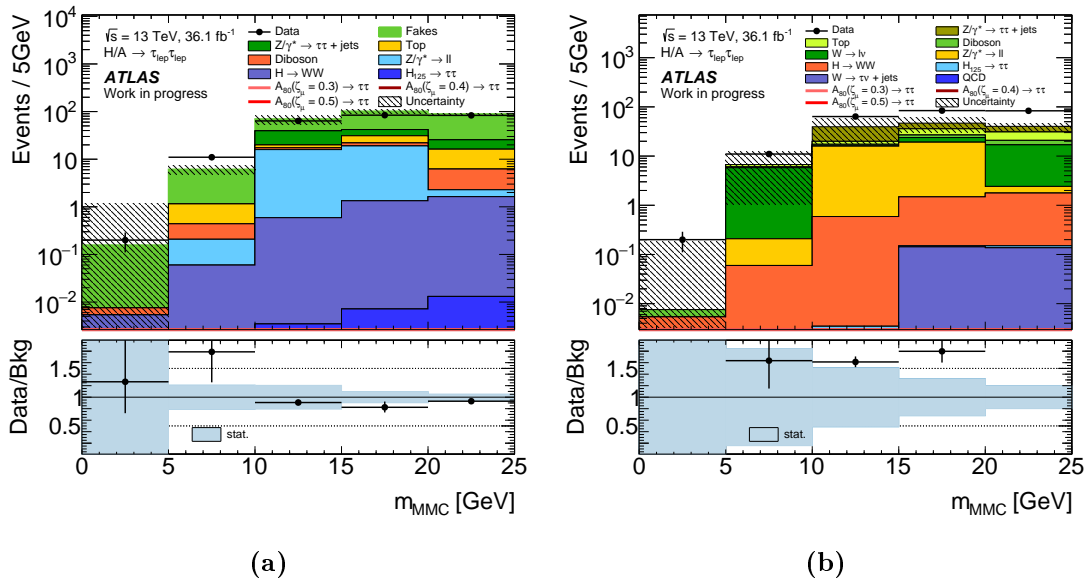

(a)   (b)

Figure B.20: Mass distribution from the missing mass calculator in the region $0\,\text{GeV} < m_{MMC} < 25\,\text{GeV}$ for a $80\,\text{GeV}$ Higgs boson (a) with fake estimation (b) without fake estimation
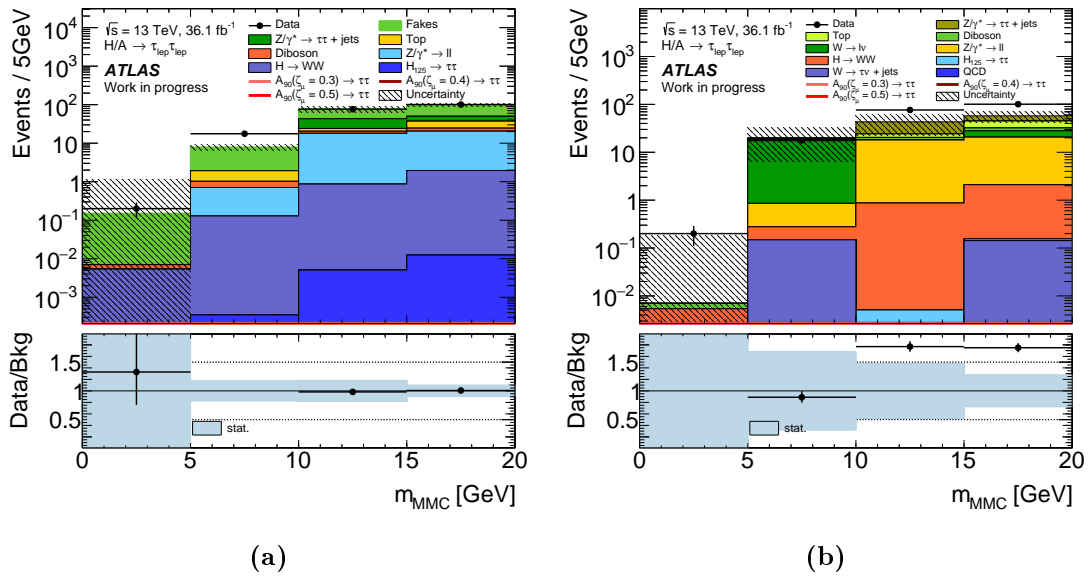
Figure B.21: Mass distribution from the missing mass calculator in the region $0\,\mathrm{GeV} < m_{MMC} < 20\,\mathrm{GeV}$ for a $90\,\mathrm{GeV}$ Higgs boson (a) with fake estimation (b) without fake estimation

B.8 Parabolic Functions for scaling factors
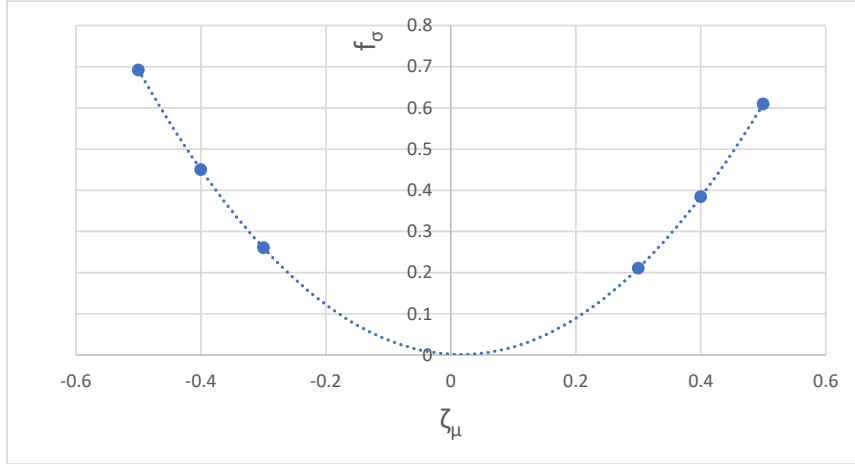
B.8.1 $m_A = 70\,\text{GeV}$

Figure B.22: Parabolic function for the scale factor of the cross-section in dependence of ζ_μ

$$f_\sigma(\zeta_\mu) = 2.596 \cdot \zeta_\mu^2 - 0.083 \cdot \zeta_\mu + 0.002 \tag{B.1}$$

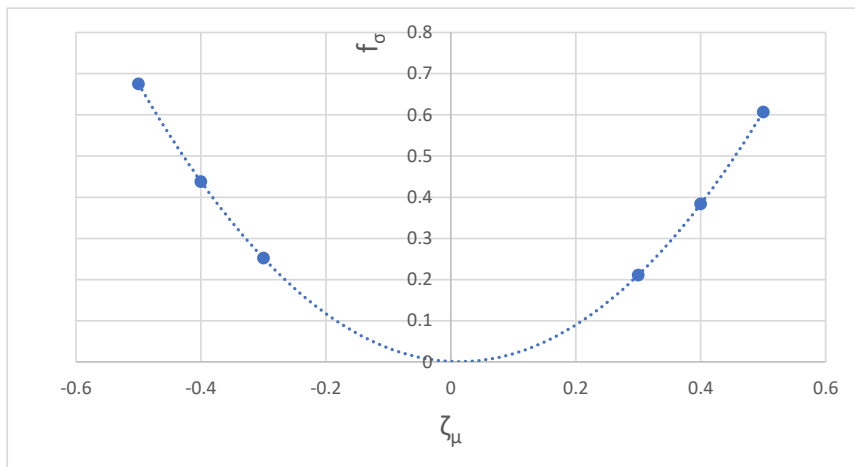### B.8.2 $m_A = 80\,\text{GeV}$

Figure B.23: Parabolic function for the scale factor of the cross-section in dependence of ζ_μ

$$f_\sigma(\zeta_\mu) = 2.560 \cdot \zeta_\mu^2 - 0.068 \cdot \zeta_\mu + 0.001 \tag{B.2}$$
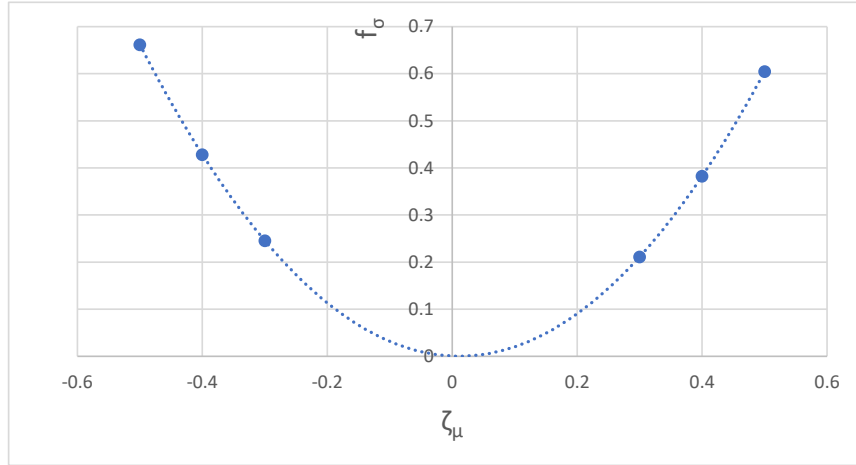
B.8.3 $m_A = 90\,GeV$

Figure B.24: Parabolic function for the scale factor of the cross-section in dependence of ζ_μ

$$f_\sigma(\zeta_\mu) = 2.530 \cdot \zeta_\mu^2 - 0.057 \cdot \zeta_\mu + 0.001 \tag{B.3}$$

Bibliography

[1] J. J. Thomson M.A. F.R.S. "XL. Cathode Rays". *The London, Edinburgh, and Dublin Philosophical Magazine and Journal of Science*, 44(269):293–316, 1897. URL: `https://doi.org/10.1080/14786449708621070`, `doi:10.1080/14786449708621070`.

[2] A. Einstein. "Die Grundlage der allgemeinen Relativitätstheorie [AdP 49, 769 (1916)]". *Annalen der Physik*, 14(1):517–571, 1916. URL: `https://onlinelibrary.wiley.com/doi/abs/10.1002/andp.200590044`, `doi:10.1002/andp.200590044`.

[3] Julian Schwinger. "Quantum Electrodynamics. I. A Covariant Formulation". *Phys. Rev.*, 74:1439–1461, Nov 1948. URL: `https://link.aps.org/doi/10.1103/PhysRev.74.1439`, `doi:10.1103/PhysRev.74.1439`.

[4] R. P. Feynman. "Mathematical Formulation of the Quantum Theory of Electromagnetic Interaction". *Phys. Rev.*, 80:440–457, Nov 1950. URL: `https://link.aps.org/doi/10.1103/PhysRev.80.440`, `doi:10.1103/PhysRev.80.440`.

[5] Sheldon L. Glashow. "Partial-symmetries of weak interactions". *Nuclear Physics*, 22(4):579 – 588, 1961. URL: `http://www.sciencedirect.com/science/article/pii/0029558261904692`, `doi:https://doi.org/10.1016/0029-5582(61)90469-2`.

[6] Steven Weinberg. "A Model of Leptons". *Phys. Rev. Lett.*, 19:1264–1266, Nov 1967. URL: `https://link.aps.org/doi/10.1103/PhysRevLett.19.1264`, `doi:10.1103/PhysRevLett.19.1264`.

[7] Abdus Salam. "Renormalizability of Gauge Theories". *Phys. Rev.*, 127:331–334, Jul 1962. URL: `https://link.aps.org/doi/10.1103/PhysRev.127.331`, `doi:10.1103/PhysRev.127.331`.

[8] **UA1** Collaboration, G. Arnison et al. "Experimental observation of lepton pairs of invariant mass around 95 GeV/c^2 at the CERN SPS collider". *Physics Letters B*, 126(5):398 – 410, 1983. URL: `http://www.sciencedirect.com/science/article/pii/0370269383901880`, `doi:https://doi.org/10.1016/0370-2693(83)90188-0`.

[9] **UA2** Collaboration, M. Banner et al. "Observation of single isolated electrons of high transverse momentum in events with missing transverse energy at the CERN pp collider". *Physics Letters B*, 122(5):476 – 485, 1983. URL: `http://www.sciencedirect.com/science/article/pii/0370269383916052`, `doi:https://doi.org/10.1016/0370-2693(83)91605-2`.

[10] Peter W. Higgs. "Broken Symmetries and the Masses of Gauge Bosons". *Phys. Rev. Lett.*, 13:508–509, Oct 1964. URL: `https://link.aps.org/doi/10.1103/PhysRevLett.13.508`, `doi:10.1103/PhysRevLett.13.508`.

[11] Peter W. Higgs. "Spontaneous Symmetry Breakdown without Massless Bosons". *Phys. Rev.*, 145:1156–1163, May 1966. URL: `https://link.aps.org/doi/10.1103/PhysRev.145.1156`, `doi:10.1103/PhysRev.145.1156`.

[12] F. Englert and R. Brout. "Broken Symmetry and the Mass of Gauge Vector Mesons". *Phys. Rev. Lett.*, 13:321–323, Aug 1964. URL: `https://link.aps.org/doi/10.1103/PhysRevLett.13.321`, `doi:10.1103/PhysRevLett.13.321`.

[13] **ATLAS** Collaboration, Georges Aad et al. "Observation of a new particle in the search for the Standard Model Higgs boson with the ATLAS detector at the LHC". *Phys. Lett.*, B716:1–29, 2012. `arXiv:1207.7214, doi:10.1016/j.physletb.2012.08.020`.

[14] **CMS** Collaboration, Serguei Chatrchyan et al. "Observation of a new boson at a mass of 125 GeV with the CMS experiment at the LHC". *Phys. Lett.*, B716:30–61, 2012. `arXiv:1207.7235, doi:10.1016/j.physletb.2012.08.021`.

[15] Steven Weinberg. "Non-Abelian Gauge Theories of the Strong Interactions". *Phys. Rev. Lett.*, 31:494–497, Aug 1973. URL: `https://link.aps.org/doi/10.1103/PhysRevLett.31.494`, `doi:10.1103/PhysRevLett.31.494`.

[16] David J. Gross and Frank Wilczek. "Ultraviolet Behavior of Non-Abelian Gauge Theories". *Phys. Rev. Lett.*, 30:1343–1346, Jun 1973. URL: `https://link.aps.org/doi/10.1103/PhysRevLett.30.1343`, `doi:10.1103/PhysRevLett.30.1343`.

[17] H. David Politzer. "Reliable Perturbative Results for Strong Interactions?". *Phys. Rev. Lett.*, 30:1346–1349, Jun 1973. URL: `https://link.aps.org/doi/10.1103/PhysRevLett.30.1346`, `doi:10.1103/PhysRevLett.30.1346`.

[18] H. Fritzsch, M. Gell-Mann, and H. Leutwyler. "Advantages of the color octet gluon picture". *Physics Letters B*, 47(4):365 – 368, 1973. URL: `http://www.sciencedirect.com/science/article/pii/0370269373906254, doi:https://doi.org/10.1016/0370-2693(73)90625-4`.

[19] William N. Cottingham and Derek A. Greenwood. *An introduction to the standard model of particle physics*. Cambridge Univ. Press, Cambridge, 1. publ. edition, 1998. URL: `http://slubdd.de/katalog?TN_libero_mab21458909`.

[20] Steven Schramm. "Searching for Dark Matter with the ATLAS Detector", 2017. URL: `http://slubdd.de/katalog?TN_libero_mab216541452`.

[21] Matic Lubej. "Standard Model", 2015. URL: `https://www.physik.uzh.ch/groups/serra/StandardModel.html`.

[22] Evgeny Akhmedov. "Majorana neutrinos and other Majorana particles: Theory and experiment". In *The Physics of Ettore Majorana*. Cambridge University Press, 2014. URL: `https://inspirehep.net/record/1333680/files/arXiv:1412.3320.pdf, arXiv:1412.3320`.

[23] Paul Langacker. "Introduction to the Standard Model and Electroweak Physics". In *Proceedings of Theoretical Advanced Study Institute in Elementary Particle Physics on The dawn of*

the LHC era (TASI 2008): Boulder, USA, June 2-27, 2008, pages 3–48, 2010. URL: `https://inspirehep.net/record/810197/files/arXiv:0901.0241.pdf`, `arXiv:0901.0241`, `doi:10.1142/9789812838360_0001`.

[24] John Ellis. "Higgs Physics". In *Proceedings, 2013 European School of High-Energy Physics (ES-HEP 2013): Paradfurdo, Hungary, June 5-18, 2013*, pages 117–168, 2015. URL: `https://inspirehep.net/record/1272850/files/arXiv:1312.5672.pdf`, `arXiv:1312.5672`, `doi:10.5170/CERN-2015-004.117`.

[25] Kien Nguyen. "The Higgs Mechanism", 2009. URL: `https://www.theorie.physik.uni-muenchen.de/lsfrey/teaching/archiv/sose_09/rng/higgs_mechanism.pdf`.

[26] K.K. Gan. "Parity and Charge conjugation", 2010. URL: `https://www.physics.ohio-state.edu/~gan/teaching/winter10/Chapter6.pdf`.

[27] C. S. Wu, E. Ambler, R. W. Hayward, D. D. Hoppes, and R. P. Hudson. "Experimental Test of Parity Conservation in Beta Decay". *Physical Review*, 105:1413–1415, February 1957. `doi:10.1103/PhysRev.105.1413`.

[28] M. Jeitler. "Symmetries and Conservation Laws". URL: `http://www.hephy.at/fileadmin/user_upload/Lehre/Unterlagen/fabjan/TP11_3Symmetries.pdf"`.

[29] PDG. "Status of the Higgs Boson physics", 2017. URL: `http://pdg.lbl.gov/2018/reviews/rpp2018-rev-higgs-boson.pdf`.

[30] Katharina Schleicher. "Higgs Boson: Spin and CP", September 2014. URL: `https://terascale.physik.uni-freiburg.de/lehre/ss_14/StudentMaterial/SchleicherProc`.

[31] Fred Jegerlehner. "Muon g - 2 theory: The hadronic part". *EPJ Web Conf.*, 166:00022, 2018. `arXiv:1705.00263`, `doi:10.1051/epjconf/201816600022`.

[32] Adriano Cherchiglia, Dominik Stöckinger, and Hyejung Stöckinger-Kim. "Muon g-2 in the 2HDM: maximum results and detailed phenomenology". *Phys. Rev.*, D98:035001, 2018. `arXiv:1711.11567`, `doi:10.1103/PhysRevD.98.035001`.

[33] Antonio Pich and Paula Tuzon. "Yukawa Alignment in the Two-Higgs-Doublet Model". *Phys. Rev.*, D80:091702, 2009. `arXiv:0908.1554`, `doi:10.1103/PhysRevD.80.091702`.

[34] Mikolaj Misiak and Matthias Steinhauser. "Weak radiative decays of the B meson and bounds on $M_{H^\pm}$ in the Two-Higgs-Doublet Model". *Eur. Phys. J.*, C77(3):201, 2017. `arXiv:1702.04571`, `doi:10.1140/epjc/s10052-017-4776-y`.

[35] **CMS** Collaboration. "Search for additional neutral Higgs bosons decaying to a pair of tau leptons in pp collisions at $\sqrt{s} = 7$ and 8 TeV". Technical Report CMS-PAS-HIG-14-029, CERN, Geneva, 2015. URL: `https://cds.cern.ch/record/2041463`.

[36] S. S. Wilks. "The Large-Sample Distribution of the Likelihood Ratio for Testing Composite Hypotheses". *Ann. Math. Statist.*, 9(1):60–62, 03 1938. URL: `https://doi.org/10.1214/aoms/1177732360`, `doi:10.1214/aoms/1177732360`.

[37] Abraham Wald. "Tests of Statistical Hypotheses Concerning Several Parameters When the Number of Observations is Large". *Transactions of the American Mathematical Society*, 54(3):426–482, 1943. URL: http://www.jstor.org/stable/1990256.

[38] Glen Cowan, Kyle Cranmer, Eilam Gross, and Ofer Vitells. "Asymptotic formulae for likelihood-based tests of new physics". *Eur. Phys. J.*, C71:1554, 2011. [Erratum: Eur. Phys. J.C73,2501(2013)]. arXiv:1007.1727, doi:10.1140/epjc/s10052-011-1554-0,10.1140/epjc/s10052-013-2501-z.

[39] Nicole A. Lazar Ronald L. Wasserstein. "The ASA's Statement on p-Values: Context, Process, and Purpose". *The American Statistician*, 70:2:129–133, 2016. URL: https://amstat.tandfonline.com/doi/full/10.1080/00031305.2016.1154108?scroll=top&needAccess=true#.W5kDwmNCTIU.

[40] Eilam Gross Glen Cowan. "Discovery significance with statistical uncertainty in the background estimate", 2008. URL: https://www.pp.rhul.ac.uk/~cowan/stat/notes/SigCalcNote.pdf.

[41] Max Märker. "Boosted Decision Trees in the analysis of $A/H \to \tau^+\tau^-$ with ATLAS", 2017. URL: https://iktp.tu-dresden.de/IKTP/pub/17/Maerker_Max_Masterarbeit.pdf.

[42] A. L. Read. "Presentation of search results: the CL_s technique". *Journal of Physics G: Nuclear and Particle Physics*, 28(10), 2002. URL: http://iopscience.iop.org/article/10.1088/0954-3899/28/10/313/meta.

[43] Glen Cowan. "Some Statistical Tools for Particle Physics", 2016. URL: http://www.pp.rhul.ac.uk/~cowan/stat/cowan_munich16.pdf.

[44] **CERN** Collaboration. "The Large Hadron Collider", 2018. URL: https://home.cern/topics/large-hadron-collider.

[45] **CERN** Collaboration. "LHC the guide". Brochure, 2017. URL: http://cds.cern.ch/record/2255762/files/CERN-Brochure-2017-002-Eng.pdf.

[46] **CERN** Collaboration. "LHC luminosity charts", 2017. URL: https://lpcc.web.cern.ch/lhc-luminosity-charts.

[47] **ATLAS** Collaboration, Dan Tovey. "Highlights from the ATLAS Experiment", 2017. URL: https://indico.cern.ch/event/466934/contributions/2473175/attachments/1490328/2316309/Tovey-ATLAS-EPS-2017-Final.pdf.

[48] Lyndon Evans and Philip Bryant. "LHC Machine". *Journal of Instrumentation*, 3(08):S08001, 2008. URL: http://stacks.iop.org/1748-0221/3/i=08/a=S08001.

[49] **ATLAS** Collaboration, G. Aad et al. "The ATLAS Experiment at the CERN Large Hadron Collider". *Journal of Instrumentation*, 3(08):S08003, 2008. URL: http://stacks.iop.org/1748-0221/3/i=08/a=S08003.

[50] A Vogel. "ATLAS Transition Radiation Tracker (TRT): Straw Tube Gaseous Detectors at High Rates". Technical Report ATL-INDET-PROC-2013-005, CERN, Geneva, Apr 2013. URL: http://cds.cern.ch/record/1537991.

[51] **Desy**. "Calorimeters - Energy measurement", 2012. URL: `http://www.desy.de/~garutti/LECTURES/ParticleDetectorSS12/L10_Calorimetry.pdf`.

[52] M.Battaglieri. "Hadronic Calorimeters", 2015. URL: `https://www.ge.infn.it/~batta/Lect3-hadrcal.pdf`.

[53] Dirk Duschinger. "Search for New Physics in Fully Hadronic Di-tau Final States with the ATLAS Detector", 2013. URL: `https://iktp.tu-dresden.de/IKTP/pub/13/diploma_thesis_dirk_duschinger.pdf`.

[54] Yu Nakahama. "The ATLAS Trigger System: Ready for Run-2". *Journal of Physics: Conference Series*, 664, 2015. URL: `http://iopscience.iop.org/article/10.1088/1742-6596/664/8/082037`.

[55] Martin Pohl Simonetta Gentile. "Physics of Tau Leptons", 1995. URL: `https://cds.cern.ch/record/290480/files/ppe-95-147.pdf`.

[56] Michael H. Seymour and Marilyn Marx. "Monte Carlo Event Generators". In *Proceedings, 69th Scottish Universities Summer School in Physics : LHC Phenomenology (SUSSP69): St.Andrews, Scotland, August 19-September 1, 2012*, pages 287–319, 2013. `arXiv:1304.6677`, `doi:10.1007/978-3-319-05362-2_8`.

[57] **ATLAS** Collaboration, Georges Aad et al. "Electron reconstruction and identification efficiency measurements with the ATLAS detector using the 2011 LHC proton-proton collision data". *Eur. Phys. J.*, C74(7):2941, 2014. `arXiv:1404.2240`, `doi:10.1140/epjc/s10052-014-2941-0`.

[58] Marco Bonvini. "Higgs codes", May 2018. URL: `https://www.ge.infn.it/~bonvini/higgs/`.

[59] **PDG**. "τ", 2014. URL: `http://pdg.lbl.gov/2013/listings/rpp2013-list-tau.pdf`.

[60] A. Elagin, P. Murat, A. Pranko, and A. Safonov. "A New Mass Reconstruction Technique for Resonances Decaying to di-tau". *Nucl. Instrum. Meth.*, A654:481–489, 2011. `arXiv:1012.4686`, `doi:10.1016/j.nima.2011.07.009`.

[61] Peter Fackeldey. "Measurement of the CP-Mixing in Higgs to Tau Tau decays". Master's thesis, RWTH Aachen University, July 2016. URL: `http://www.institut3b.physik.rwth-aachen.de/global/show_document.asp?id=aaaaaaaaaauwfgz`.

[62] **PDG**. "Top Quark", 2018. URL: `http://pdg.lbl.gov/2018/listings/rpp2018-list-t-quark.pdf`.

[63] Gaetano Barone. "MCPAnalysisGuidelinesMC15", 2018. URL: `https://twiki.cern.ch/twiki/bin/viewauth/AtlasProtected/MCPAnalysisGuidelinesMC15`.

[64] Sarah Heim. "Past Run2 Electron Efficiencies Recommendations", 2018. URL: `https://twiki.cern.ch/twiki/bin/view/AtlasProtected/EfficiencyMeasurements2015MC15b`.

[65] **ATLAS** Collaboration. "Electron efficiency measurements with the ATLAS detector using the 2015 LHC proton-proton collision data". Technical Report ATLAS-CONF-2016-024, CERN, Geneva, Jun 2016. URL: `http://cds.cern.ch/record/2157687`.

[66] **Atlas** Collaboration, G. Aad et al. "Muon reconstruction performance of the ATLAS detector in proton–proton collision data at *sqrts*=13 TeV". *The European Physical Journal C*, 76(5):292, May 2016. URL: `https://doi.org/10.1140/epjc/s10052-016-4120-y`, `doi:10.1140/epjc/s10052-016-4120-y`.

[67] Andrea Coccaro. "Flavour tagging recommendations in release 20.7", 2017. URL: `https://twiki.cern.ch/twiki/bin/view/AtlasProtected/BTagCalib2015`.

[68] **ATLAS** Collaboration. "Cross-section measurements of the Higgs boson decaying to a pair of tau leptons in proton–proton collisions at $\sqrt{s} = 13$ TeV with the ATLAS detector". Technical Report ATLAS-CONF-2018-021, CERN, Geneva, Jun 2018. URL: `https://cds.cern.ch/record/2621794`.

[69] **CMS** Collaboration, Serguei Chatrchyan et al. "Observation of a new boson at a mass of 125 GeV with the CMS experiment at the LHC". *Phys. Lett.*, B716:30–61, 2012. `arXiv:1207.7235`, `doi:10.1016/j.physletb.2012.08.021`.

[70] Charalampos Anastasiou, Claude Duhr, Falko Dulat, Elisabetta Furlan, Thomas Gehrmann, Franz Herzog, Achilleas Lazopoulos, and Bernhard Mistlberger. "High precision determination of the gluon fusion Higgs boson cross-section at the LHC". *JHEP*, 05:058, 2016. `arXiv:1602.00695`, `doi:10.1007/JHEP05(2016)058`.

[71] G. Apollinari, O. Brüning, T. Nakamoto, and Lucio Rossi. "High Luminosity Large Hadron Collider HL-LHC". *CERN Yellow Report*, (5):1–19, 2015. `arXiv:1705.08830`, `doi:10.5170/CERN-2015-005.1`.

[72] **ATLAS** Collaboration. "CentralMC15ProductionList", October 2017. URL: `https://twiki.cern.ch/twiki/bin/view/AtlasProtected/CentralMC15ProductionList`.

Erklärung

Ich versichere, dass ich die vorliegende Arbeit selbstständig verfasst und keine anderen als die angegebenen Quellen und Hilfsmittel benutzt habe. Ich reiche diese Arbeit erstmals als Prüfungsleistung ein. Mir ist bekannt, dass ein Betrugsversuch mit der Note "nicht bestanden" (5,0) geahndet wird und im Wiederholungsfall zum Ausschluss von der Einbringung weiterer Prüfungsleistungen führen kann.

_____   _____
Ort,Datum   Paul Moder

Danksagung